LASER ANEMOMETER MEASUREMENTS IN DRAG-REDUCING CHANNEL FLOWS

By

MICHAEL MACK REISCHMAN

Bachelor of Science in Mechanical Engineering
New Mexico State University
Las Cruces, New Mexico
1967

Master of Science in Mechanical Engineering
New Mexico State University
Las Cruces, New Mexico
1969

Submitted to the Faculty of the Graduate College
of the Oklahoma State University
in partial fulfillment of the requirements
for the Degree of
DOCTOR OF PHILOSOPHY
December, 1973

LASER ANEMOMETER MEASUREMENTS IN

DRAG-REDUCING CHANNEL FLOWS

Thesis Approved:

W. H. Liederman, Jr.
Thesis Adviser

Dennis K McLaughlin

R F Lowery

Bennett Basore

N N Durham
Dean of the Graduate College

ACKNOWLEDGMENTS

I would like, above all, to thank my advisor, Dr. William G. Tiederman, Jr. for his personal interest and excellent guidance throughout this study. Thanks also go to Dr. Dennis K. McLaughlin for the many discussions contributing insight about laser anemometry. I am also grateful to Nancy Elliott for the numerous drafts and to Eldon Hardy for the excellent art work.

The Mechanical and Aerospace Engineering Department of Oklahoma State University supported the research discussed here and partially provided my livelihood - both of which are greatly appreciated.

However, the lioness' share of the thanks must go to my wife "Babe" for the prolonged forbearance.

TABLE OF CONTENTS

LIST OF TABLES

LIST OF FIGURES

NOMENCLATURE

English

A	law of the wall constant, slope = 1/k
A^+	constant in eddy diffusivity expression
B	law of the wall constant, intercept
B'	constant in ΔB predictor of van Driest
C	buffer region velocity profile constant, slope
D	buffer region velocity profile constant, intercept
DR	drag reduction, %
D_H	hydraulic diameter, ft
D'	constant in ΔB predictor of Rudd, $D' = [1+k_3\theta u_\tau/\upsilon]^{\frac{1}{2}}$
d	diameter, inches
E	eddy diffusivity, $E = \varepsilon/\upsilon$
f_D	Doppler frequency, Hz
f_L	calculated low frequency bound, Hz
f_H	calculated high frequency bound, Hz
K_1, K_2	constants in the ΔB predictor of Tomita
k	von Karman constant, k = 0.41
k_1	modified mixing length constant in ΔB predictor of van Driest
k_3	constant in the ΔB predictor of Rudd
L^+	buffer region constant in ΔB predictor of van Driest
N	number of individual velocity realizations
$\overline{P}$	non-dimensional pressure gradient, $\overline{P} = \frac{\tau_w}{\rho \overline{U}^2_{AVG}}$
P	pressure, psi
$p(u)$	probability density function

Re	Reynold number, $Re = \overline{U}_{AVG} D_H/[\upsilon]_{SOL}$
R	Reynold number based on channel half width, $R = \frac{\overline{U}_{AVG}W}{2\upsilon}$
T	period, sec
$\overline{T}_D$	mean Doppler period, sec
$\overline{T}_B$	average time between bursts, sec
t_1	polymer relaxation time, sec
t	time, sec
U	instantaneous streamwise velocity, $U = \overline{U} + u$
$\overline{U}$	streamwise mean velocity, ft/sec
$\overline{U}'$	non-dimensional streamwise velocity, $\overline{U}' = \overline{U}/\overline{U}_{AVG}$
$\overline{U}_{AVG}$	bulk average velocity, ft/sec
$\overline{U}_{MAX}$	channel centerline velocity, ft/sec
u_τ	shear velocity, $u_\tau = [\tau_W/\rho]^{\frac{1}{2}}$, ft/sec
u_τ^*	critical or onset wall shear velocity, ft/sec
u'	streamwise turbulent intensity, $u' = \sqrt{\overline{u^2}}$
u	streamwise velocity fluctuation, ft/sec
U^+	non-dimensional velocity, $U^+ = \overline{U}/u_\tau$
U_I	individual realization of the streamwise component of the velocity vector
V_I	individual realization of the velocity vector
v'	turbulent intensity normal to the wall $v' = \sqrt{\overline{v^2}}$
W	channel width, inches
x	streamwise coordinate direction, inches
y	coordinate direction normal to wall, inches
y'	non-dimensional distance, $y' = 2y/W$
y^+	non-dimensional distance normal to wall, $y^+ = yu_\tau/\upsilon$

y_1	dummy variable
z	spanwise coordinate direction, inches

Greek

ΔX	beam intersection dimension in streamwise direction, inches
ΔY	beam intersection dimension normal to the wall, inches
ΔZ	beam intersection in the spanwise direction, inches
ΔB	additive constant in law of the wall
ω_i	weighting function
γ_i	geometric function relating the projected area of the probe volume to V_i
λ	streak spacing, inches
λ^+	non-dimensional streak spacing, $\lambda^+ = \lambda u_\tau / \upsilon$
Λ	wavelength of light, Å
θ	beam intersection angle, degrees
υ	kinematic viscosity, ft^2/sec
τ_w	wall shearing stress, psi
ρ	fluid density, lb/ft^3
ξ (u)	energy density function
ε	turbulent diffusivity, ft^2/sec
α	proportionality constant in ΔB predictors

Subscripts

SOL	solvent equivalent
DPS	dilute polymer solution
AVG	average
MAX	maximum

w	wall
l	buffer region

Abbreviations

mw	milliwatts
gpm	gallons per minute
mg	milligrams
l	liter
wppm	parts per million by weight

CHAPTER I

INTRODUCTION

The general characteristics of drag-reduction can best be understood in terms of the precise definition offered by Lumley (1). He defines drag-reduction as the "reduction of skin friction in turbulent flow below that of the solvent alone". The "reduction in skin friction" refers to a lowering of the wall shearing stress when small amounts, less than 250 wppm (parts per million by weight), of a high molecular weight polymer are added to a Newtonian solvent. The drag-reduction (friction-reduction) is greater than that obtained due to the change in Reynolds number caused by the minor changes in the solvent viscosity or density. As the definition points out, the addition of polymer additives results in drag-reduction only when the flow is turbulent. Recent survey articles, such as those by Hoyt (2) and Lumley (1), provide excellent commentary on additional aspects of the drag-reduction phenomenon and its application.

Drag-reduction has been studied by various techniques. Pressure drop-flow rate experiments have shown only the magnitude and scope of the phenomenon. For example, a maximum drag-reduction asymptote of approximately 80% exists and drag-reducing additives include soap solutions, algae, plant derivatives and high molecular weight polymers. Flow visualization experiments have given some insight into the drag-reduction mechanism and have provided the basis for qualitative inter-

pretations about various aspects of a drag-reducing flow. Numerous velocity measurements have been made in an attempt to quantify the effect of polymer additives. Due to the ambiguities in the measurement technique and confusing features of the flow facilities, these past works are contradictory and difficult to interpret.

Purpose

The major purpose was to accurately measure the mean and fluctuating velocities of a drag-reducing flow in a fully-developed, two-dimensional turbulent channel flow. The intention was to make velocity measurements which are sufficient to, 1) describe the mean turbulent transport of momentum, 2) test theoretical models of past and future investigators and 3) make inferences about the drag-reduction mechanism.

Inherent in the above purpose is the fundamental desire to measure the effects of the polymer additives on only the turbulent processes. Consequently, the simplest experimental apparatus which possesses all the essential features of a turbulent shear flow, namely, production, convection and dissipation, was chosen. This apparatus yields a fully-developed, two-dimensional channel flow. An apparatus of this type is suitable to give results leading to a better understanding of the drag-reduction mechanism and to provide the test case for modeling techniques.

The desired accuracy of the velocity measurements required the use of a laser Doppler anemometer. A laser anemometer measuring individual realizations was used because it was the only present day laser anemometer technique which would yield accurate measurements in the high fluctuation, near-wall region. The technique also has the advantages of straightforward and unambiguous data analysis.

Review of Previous Investigations

Twenty of the previous investigations which have measured velocities in drag-reducing flows are listed in Table 1. The number of these investigations and the continuing attempts to conduct the definitive experiment indicates the interest in the problem and the lack of faith that the scientific community has in the bulk of these measurements. The reasons that none of these experiments have been conclusive has varied. In most cases the problem has been the measurement device, but in others the difficulty has been the flow apparatus.

The experimental techniques can be divided into four groups: bubble tracing, laser Doppler anemometers, hot-element probes and pitot probes. The largest group is the pitot probe investigations. Pitot probes are subject to error and Metzner and Astarita (23) attribute these errors to the influence of additional viscoelastic normal stress terms. Consequently, the time-average of fluctuating stresses are not simply related to the time-averaged velocity fluctuations. For example, Smith, et al. (24) have demonstrated that measurements in identical flow situations made by various size pitot probes yield different results. Corrections for pitot probe techniques are complex and in most cases are omitted. A notable exception is Tomita (19), who has applied viscoelastic corrections to his pitot probe measurements.

Hot-film and hot-wire sensors depend upon the heat transfer characteristics of the medium. Friehe and Schwartz (25) have shown that hot-element sensors are difficult to calibrate since the polymer additives alter the heat transfer characteristics of the solvent. Moreover, the calibrations drift unpredictably as contaminates collect on the

TABLE I

SUMMARY OF PAST INVESTIGATIONS

Investigator	Experimental Facility	Measurement Type
Chung & Graebel (3)	.47" pipe, gravity drain, approximately 400 diameter downstream	Laser Doppler Anemometer (LDA)
Elata, et al. (4)	2" pipe, probe diameter = .12"	Pitot Probe
Ernst (5)	.75", 1.50" pipes, 400, 125 diameters downstream, blowdown operation, .007" pitot probe	Pitot Probe
Giles (6)	1.25" pipe, .021" probe diameter, 133 diameters downstream, pumped	Pitot Probe
Goldstein, et al. (7)	.55" glass tube, 65 diameter downstream, gravity feed	LDA
Goren, Norbury (8)	2" pipe, gravity drain	Pitot Probe
Killen & Almo (9)	Rotating concentric cylinders	Pitot Probe
Kumor & Sylvester (10)	8" square duct with splitter plate, pumped	LDA
Logan (11)	½" square duct, 65 diameters downstream, gravity feed, gravity drain	LDA
Nicodemo, et al. (12)	.79", 1.21" pipes, probe diameter of .3", towing tank	Pitot Probe

TABLE I (Continued)

Patterson & Florez (13)	1" pipe, 200 diameter downstream, pumped	Hot Film Anemometer and Pitot Probe
Rollin & Seyer (14)	1", 2.75" pipes; 187, 117 diameters downstream, pumped flow	Bubble Tracing
Rudd (15)	½" square duct, 120 widths downstream, pumped	LDA
Seyer & Metzner (16)	1" pipe	Bubble Tracing
Shankar (17)	1.25" pipe, sample size of 8-10, pumped flow	LDA (Individual Realization)
Spangler (18)	.761" pipe	Pitot Probe
Tomita (19)	1" pipe, 180 diameters downstream, probe diameter = .040	Pitot Probe
Wetzel & Tsai (20)	Gravity flow water, 6" tunnel $\bar{U}$=4-8 ft/sec	Pitot Probe
Virk, et al. (21)	1.26" pipe, blowdown, .010" and .066" probe diameter	Pitot Probe & Hot Film
Wells, et al. (22)	.76" pipe, 400 diameter downstream, probe diameter = 0.20"	Pitot Probe

sensors. This drifting problem is particularly severe in dilute polymer solutions where the sensitivity of the probe to velocity changes is lower than it is in water alone.

Bubble tracing is an extremely tedious process, and consequently sample sizes are generally small. For accurate results large samples are required, particularly in the near-wall region (see Donohue, et al. [26]). For this reason bubble tracing results have been hampered by large uncertainties.

The fourth group of workers have used the laser Doppler anemometer, which is a non-interfering instrument that does not depend on the rheological or intensive properties of the working fluid. Properly applied it is generally believed that it will yield excellent results in a dilute polymer flow. The laser anemometer was first used in drag-reducing flows by four investigators almost simultaneously: Chung and Graebel (3), Goldstein, et al. (7), Rudd (15) and Shankar (17). The measurements of Shankar (17) have insufficient sample sizes for accurate results. Meanwhile, Goldstein, et al. (7) made measurements only on the tube centerline. Chung and Graebel (3) were operating in a small pipe where the spatial resolution of their laser anemometer was very poor because the longest dimension of their probe volume was oriented normal to the wall.

There is a group which appears to have made acceptable laser velocity measurements in drag-reducing flows. This group consists of Rudd (15), Logan (11) and Kumor and Sylvester (10). Rudd's measurements were by far the most comprehensive, and his results were the first to quantify the so-called viscous "sublayer thickening" and to show increased streamwise intensities and decreased spanwise intensities.

Logan (11) verified Rudd's findings in the streamwise direction and made measurements of the turbulent intensities normal to the wall, as well as Reynolds stress distribution for a drag-reducing flow. The most recent work is that of Kumor and Sylvester (10), which was designed to characterize the mean and fluctuating velocity components of a dilute polymer solution undergoing progressive degradation. Their measurements extend to a y^+ of three and are the most detailed in that aspect. These last researchers, Rudd, Logan, Kumor and Sylvester, present the best available data but all were conducted in a square apparatus.

Rudd (15) and Logan (11) both utilized a one-half inch square duct for their measurements. Whitelaw (27) has recently shown that non-symmetric secondary flows are significant in square-duct flows. In fact, Logan recognized part of the problem of operating in a small square and measured the secondary flow. He then calculated that u_τ values based upon pressure drop were 30% to 40% low compared to two-dimensional values of u_τ. This ambiguity is evident in the abnormally high results for the normalized solvent turbulent intensities, u'/u_τ, shown by both Rudd and Logan. However, there is still the problem that the flow field is three-dimensional. Kumor and Sylvester used an eight-inch square duct with a submerged off-center flat plate. Boundary layer measurements were made by traversing the laser anemometer normal to the plate. Secondary flows and the pressure gradient in this type configuration are not known. Kumor and Sylvester have offered no water data results that allows verification of the suitability of this facility. In all cases the experimental apparatus yielded secondary flows or unknown pressure gradients which confuse the issue about the effect of the polymer additive on the turbulence.

In addition to inconsistencies in the flow facility, the type of laser anemometry used is of concern. All three, Logan, Kumor and Sylvester and Rudd used continuous-wave systems. Continuous-wave laser anemometers are susceptible to the Doppler ambiguity and signal "drop out", both of which are fundamental limitations. A spectrum analyzer was used in all three cases and the effect of signal drop-out on a spectrum analyzer is not fully understood.

Polymer solution degradation is the last item of concern. It has not been established that a 40% drag-reducing degraded solution will yield the same velocity profile as a fresh solution at 40% drag-reduction. Kumor and Sylvester closely documented their drag-reduction, but there is no assurance that their velocity profiles are valuable in a comparative sense. Rudd's pumped system, no doubt, had some polymer degradation, but it was not outlined nor its importance mentioned.

In summary, previous results from all four groups have failed to yield accurate velocity measurements which can be used to 1) test theoretical models, 2) provide calculation schemes for engineering predictions, and 3) determine how polymer additives effect the turbulent mechanisms.

Scope of the Present Study

The concept was to build a two-dimensional turbulent flow channel which, due to a slight bowing of the side walls, permitted laser anemometer measurements of both mean and fluctuating components of velocity to be made with good spatial resolution. A one inch channel width was chosen such that shear velocities on the order of 0.20 ft/sec could be attained at flow rates of 200 gallons per minute. Velocity measurements

were made as systematic variations in the polymer types and flow rates were being made. The polymer types were varied in an effort to examine the effect of molecular weights, and flow rates were varied for each polymer to examine the effect of the change in drag-reduction. The variations employed in these two parameters are outlined in Table II.

TABLE II

POLYMER CHARACTERISTICS

Polymer	Molecular Weight*	Manufacturer	% Drag-Reduction Employed
Magnifloc 837-A (polyacrylamide)	15×10^6	American Cyanimid	23.8, 35.4, 39.9
Separan AP273 (polyacrylamide)	7.5×10^6	Dow	31.3, 34.5, 40.4
Polyox WSR-301 (polyethylene oxide)	4×10^6	Union Carbide	37.8

*advertised

All tests were conducted at a polymer concentration of 100 wppm. The shear rate dependence of viscosity of each drag-reducing solution was obtained over a wide range of shear rates (15 sec^{-1} to 1000 sec^{-1}). Drag-reduction characteristics were obtained for each dilute polymer solution by conducting pressure drop-flow rate tests. However, drag-reduction in the channel was determined by calculating the shear velocity from the slope of the velocity profile near the wall and comparing

it with the wall shear velocity for an equivalent solvent flow rate.

Velocity measurements were made with a laser anemometer measuring individual realizations (LAMIR) at from seven to nine locations in the two-dimensional channel. The velocity data is naturally free from the ambiguities of continuous-wave laser anemometer systems, and was corrected for the errors due to both statistical biasing of the realizations and the velocity gradient. The sample size of the individual realizations were, with the exception of two locations, large enough to insure (at the 95% confidence level) that the measurements were within 5%. The bulk of the measurements were within 2.5% to 3%. The experimental apparatus, peripheral components and data handling equipment are described in Chapter II.

Chapter III contains the results and comparisons derived from the experimental measurements. The experimental data was utilized in establishing a mean velocity prediction technique for seven drag-reducing flows wherein three different polymers were used. The turbulent transport properties were predicted using the mean velocity profile information for the same flows. The turbulent intensity data provided a basis by which comparisons could be made and possible structure information could be implied. The fluctuation data was also used in the calculation of energy density functions, which permits data presentation in the energy domain.

The discussion of the results and how they may be interpreted in light of previous investigations is the subject of Chapter IV. The results are summarized and some conclusions are drawn in Chapter V.

CHAPTER II

EXPERIMENTAL TECHNIQUES

This chapter presents the details of the turbulent channel flow facility, its peripheral components and the individual realization laser anemometer used for velocity measurements. The data collection, reduction and correction techniques are discussed, as well as the experimental procedures used for characterization of the dilute polymer solutions.

Water Channel and Flow System

The flow facility is basically a two-dimensional channel sufficiently long such that velocity profile measurements could be made at a location where the flow is fully-developed. The unique feature of the channel is that the side walls are bowed inward very slightly. This allows the spatial resolution of the laser anemometer to be maximised in the near-wall region.

The flow channel was constructed (see Figure 1) with clear plastic, seamless walls. The uniform bowing was accomplished by means of a steel rod which, when forced inward at its support points, caused the channel walls to bow inward along their entire length. A machined nylon gauge block was used to set a predetermined channel centerline width of 1.020 inches after bowing. The channel shape and dimensions were checked on a milling machine to ensure uniformity and symmetry in the bowing over the entire length. Each wall was bowed 0.047 inches.

The channel is 12 inches tall, has a cross-sectional area of 0.089 ft^2 and a hydraulic diameter of 0.164 feet. The channel dimensions were checked at various flowrates and found to be constant within ±0.001 inches from the above values.

The entire turbulent flow channel is constructed of $\frac{1}{4}$ inch plexiglas, and can be seen in Figures 2 and 3. Water enters the upstream settling chamber (see Figure 2), which is 15 inches long, 15 inches high and $11\frac{1}{2}$ inches wide, through a three-inch PVC pipe. The first baffle plate primarily redistributes the three-inch inlet flow from a jet-like configuration to one more uniform over the cross section of the upstream chamber. Three remaining baffle plates (two 64 mesh stainless steel screens and one uniformly drilled baffle plate using $\frac{1}{4}$ inch holes) serve to cut down the disturbance size and hence insure a uniform low disturbance flow near the channel entrance.

The entrance to the channel from the settling chamber is a Borda type entrance, which is located approximately three inches inside the upstream settling chamber (see Figure 2). The channel is 70 inches long, and the center of the test section is located 55 inches downstream of the entrance. The flow leaves the channel through a twelve inch x twelve inch overflow, constant head tank. The 600 gallon catch tank may be used to catch and recycle the working fluid, to route the fluid to the drain, or to serve as a reservoir tank for the pumped operation. Figure 4 shows the turbulent flow channel and its circulation system. The overall flow system can be operated in any one of three modes: continuously pumped, 600 gallon blowdown or 3700 gallon blowdown. The pumped flow mode is capable of a 200 gpm continuous flow by isolating the circulation system from the drain and by using the catch tank as

an inlet reservoir for the pump. The flow channel is isolated from any vibrations associated with the pump or its hardware. The pumped circulation system was utilized for laser anemometer setup and the solvent (water) data runs described later.

The blowdown flow modes are utilized when the working fluid is a dilute polymer solution, thereby minimizing polymer degradation and flow disturbances. By monitering the pressure and amount of air flowing into either tank a constant flow rate through the flow channel is maintained. Flow rates up to 400 gpm may be achieved in the blowdown modes. All piping, valves and fittings common to the three flow modes are either stainless steel, PVC, or plexiglas. Run times varied from 16 minutes to a maximum of approximately 40 minutes. All blowdown runs were routed to the drain after the solution had passed through the test section. All make-up water was filtered with a 0.5 micron woven filter and the entire flow loop was thoroughly flushed after each polymer run. Multiple flushes were also performed before each data run in order to remove impurities and check out the various systems.

90° Side-Scatter Laser Anemometer

The basic principle of the laser Doppler anemometer is to measure the Doppler shift of laser radiation scattered by small particles which are moving with the fluid. The frequency of the Doppler shift is directly proportional to the particle velocity.

The laser Doppler anemometer used here was of the individual realization type, which measures the period for 10 cycles of a Doppler burst scattered from a single particle. The essential points about a laser anemometer measuring individual realizations (LAMIR) are that the signal

is not continuous and that velocity realizations occur only when a scattering center is in the probe volume. The appearance of a scatter center in probe volume is a random event with a probability of occurrence proportional to the volume of fluid swept through the probe volume. The LAMIR output is in a form that can be processed with well-known statistical techniques. That is, if a number of independent realizations are recorded, the mean and standard deviation of the individual realizations yield estimates of the mean and root mean square velocities.

In contrast, if there are a large number of scattering centers in the probe volume, the output of the laser anemometer is essentially continuous. The continuous-wave anemometers frequently employ a frequency tracker which converts Doppler frequency to an analog signal proportional to the instantaneous velocity. Trackers are, however, limited by their electronics, and the measurement of turbulence levels above 15% - 20% have questionable accuracy. In addition, continuous-wave systems are fundamentally limited due to the Doppler ambiguity and signal drop-out.

A schematic of the basic optical setup, which is a dual-scatter or fringe anemometer system, is shown in Figure 5. The system shown uses a Spectra-Physics Model 130 5mw helium-neon (6328 Å) laser and a RCA model 7326 photomultiplier.

Figure 6 shows that the optical portion of the LAMIR is mounted on a traversing mechanism which in turn is mounted on a sturdy base. The base is mechanically isolated from the flow channel. The beam splitter, mirrors and transmitting lens yield two focused, intersecting, temporally and spatially coherent, plane polarized beams. The intersecting

beams form a beam crossing within which the light waves constructively and destructively interfere, forming a fringe pattern. The beam crossing is located such that it can be traversed across the vertical center of the flow channel. Figure 7 shows how the bowed flow channel walls and laser optics are used to give the best possible spatial resolution, that is, the maximum dimension of the beam crossing is parallel to the wall, and the smallest dimension is normal to the wall.

As shown in Figure 7, the photomultiplier receives light from the collecting lens that was scattered in a conical pattern at 90° to the plane of the incident beams. The intensity of light scattered at this angle is not optimal - but three distinct advantages are present. First, the mechanism used to traverse the laser optics is mechanically simple and can be isolated from the flow channel. Second, there is very little optically generated noise present since the majority of the sources of stray light are not in the field of view of the photomultiplier. Finally, the 90° orientation provides an opportunity to optically reduce the beam intersection's long dimension by simply adding an aperture in front of the photomultiplier.

In water the configuration shown here yields a beam intersection angle of 5.59° and the beams are focused to a resolution limit of 0.0048 inches at their $1/e^2$ intensity point. The Doppler frequency, f_D, is a function of the wavelength of incident light, the index of refraction of the medium and the beam intersection angle. Thus, for the configuration shown, f_D was 62.56 KHz for a velocity of one foot per second. The beam intersection dimensions are $\Delta Y = \Delta X = 0.0048$ inches and $\Delta Z = 0.105$ inches. Due to the collecting lens and aperture the only focused light reaching the photomultiplier comes from the

center 0.025 inches of the beam intersection. Thus, the probe volume may be considered a cylinder of 0.0048 inches diameter and 0.025 inches length. These distances are to be compared with the calculated smallest disturbance size. The Kolmogoroff microscale is an indication of the minimum eddy size possible for specific flow conditions. For the flow rates and velocities employed here, the microscale is calculated to be 0.100 inches, which is much larger than the LAMIR probe volume. There are about 40 usable fringes in the probe volume spaced at 0.000132 inches. This is an important consideration since it means that the Doppler frequency and the pedestal frequency (the low frequency proportional to the particles transit time through the probe volume) are separated by a factor of about 40.

The calculation of probe volume diameter based on the $1/e^2$ intensity point yielded a diameter of 0.0048 inches. This dimension is critical in locating the exact position of the center of the probe volume relative to the wall, thus a verification is necessary. The beam intersection edge was brought into contact with the wall using visual methods. The beam intersection was then traversed across the channel and brought into contact with the opposite wall. The distance traversed plus one beam intersection diameter was compared to a micrometer measurement of the same distance and found to agree within 0.001 inches. Thus, calculated and observed beam intersection diameters for all practical purposes are equal. Further verification of the calculated values stems from a comparison of the maximum number of fringes observed in Doppler bursts and the value computed using the known fringe spacing and the calculated $1/e^2$ diameter. The observations indicated a maximum of approximately 40 fringes, whereas the calculated value was 37. Agree-

ment is good, however a further restriction must be placed on the "effective" size of the probe volume normal to the wall. The minimum number of acceptable Doppler cycles coming from the probe volume is 13 since it is required that the period for 10 cycles be counted. Thus, as shown in Figure 8, only the central 0.00453 inches of the probe volume has 13 or more fringes. Consequently, the effective sensing diameter of the probe volume is 0.00453 inches.

Fortunately, the bowing of the channel wall provided reproducible methods for experimentally fixing the location of the channel wall. With the overhead lights out, the beam intersection and its reflections in the plexiglas wall could be brought into contact with one another. It was this location that placed the center of the probe volume one-half the width of the beam intersection from the wall. Two other methods were also used to verify the wall location. First, when seen from the photomultiplier side, microscopic scratches in the channel walls scattered light when the beams were in contact with the walls; the scattered light ceased when the laser beams were entirely in the flow. Secondly, the diffraction pattern of the laser beams on the ceiling could be noted. These three observations were used each time and found to agree. It is estimated that the wall of the channel could be located within ±0.0005 inches. The channel width can be obtained by simply traversing the LAMIR optics across the flow channel and noting the distance travelled by the LAMIR on the traverse screw thread. The traverse mechanism has a sixteen threads per inch drive and its indicator can be read within ±0.0002 inches.

LAMIR Data Processing

Data Acquisition

The purpose of the data acquisition electronics is to condition and record the electrical signals that result from the bursts of light scattered by particles in the flow. The photomultiplier converts the scattered light into an electrical current. The signal output from the photomultiplier has two components. There is a Doppler portion, which has a constant period and a Gaussian envelope. There is also a longer period component, called the pedestal, which is proportional to the scattering particles transit time across the probe volume. This composite wave form is shown, after 20 dB of amplification, in Figure 9. (For demonstrative purposes the number of Doppler cycles is much less than the 40 which are, in reality, typically present.) The purpose of the band pass filter is to remove the pedestal component from the composite signal, in addition to removing random noise outside the frequency range of interest. The band pass filter is a Multimetrics model AF-120, which, when operated in the band pass mode, has a filtering slope of 24 dB/octave. The ratio of Doppler to pedestal frequencies can be as great as 40 and as low as 13, since 13 fringes are necessary to yield a useful signal. Thus the lower limit of the band pass filter can readily be set between the lowest expected Doppler frequency and the highest expected pedestal frequency. (See Figure 10). The general procedure used here was to calculate a lower frequency bound of the mean velocity measurement based upon the expected turbulent intensity. The band pass filter's lower setting was then set at 1/2 to 1/5 of that value. For example, for an expected mean velocity which gives f_D = 31

KHz and a 30% fluctuation level, the low frequency bound, f_L, was calculated to be 21 KHz (using a conservative estimate of 33% for fluctuation level). The filter 3 dB point was actually set at 6 KHz and the results later showed no frequencies below 15 KHz. The upper frequency bound was calculated similarly. For the example sited here the upper frequency bound, f_H, was calculated to be 41 KHz. The filter 3 dB point was set at 200 KHz and the highest recorded frequency was 65 KHz. The filter settings and the measured maximum and minimum frequencies were compared for each data point and no overlap was noted.

The absolute gap between Doppler and pedestal frequencies narrows as the probe volume approaches the wall. Band pass filtering becomes a fundamental limitation if the probe volume lies on the wall because frequencies near zero are present and the Doppler and pedestal spectrums are impossible to electronically separate. This fundamental limitation placed a restriction on the near-wall measurements and limited our measurements at no closer than 0.004 inches from the wall.

Amplification of the signal in the data acquisition system was accomplished by one C-COR Wideband Video Amplifier (model 4376 A) and two Hewlett-Packard instrumentation Amplifiers (model 405 A). All amplifiers were operated at a gain setting of 20 dB. The amplified and band-pass filtered signal (as shown in Figure 9) was next routed to a magnetic tape recorder, an Ampex model 1300. The Ampex is a double-bandwidth recorder and can record signals up to 300 KHz when operating in the direct recording mode and at a tape speed of 60 inches per second. The highest frequency recorded during the research was 219 KHz. The signal generator shown in Figure 9 was used to provide identification marks on the magnetic tape recording.

Data Reduction

The purpose of the data reduction scheme was to measure, verify and record the Doppler period of an individual realization from a particle passing through the probe volume. A verification of the individual realization was necessary because Doppler bursts will occasionally have single or multiple cycles missing or suppressed. The specific reasons for these missing cycles are not completely understood but can seriously affect the accuracy of the data. Also noise present within the frequency range of interest can cause the counter to start erroneously. These two sources of error must be taken into account and consequently - the data reduction system used here. The lower half of Figure 9 shows the block diagram for the data reduction process. The data tapes were played back at 7½ inches per second. This time expansion of 8 times gave the human operator time to make decisions concerning the validity of each velocity realization.

The amplifier in the data reduction block diagram, a Hewlett-Packard model 405 A, was not used in the majority of the data reduction runs, but is shown for completeness. The Multimetrics model AF-120 band pass filter was set at values which were 1/8 of those used during data recording. The band pass filter was used primarily during playback to reduce the effect of magnetic tape noise and broad band noise from the recording amplifiers.

The visual verification of a Doppler burst was achieved by checking each individual realization whose Doppler period was counted to insure that 10 consecutive Doppler cycles from a single realization were being counted. It was for this reason that the crucial elements of the data

reduction scheme were the Schmitt trigger and the storage oscilloscope. The Schmitt trigger transformed each cycle of a Doppler burst which had an amplitude above a preset level into a pulse. Thus, the Schmitt trigger output was a constant amplitude pulse train and the occurrence of an extraneous or missing pulse was immediately obvious. (See Figure 9.) Its output simultaneously triggered a Tektronix type 564 B Storage Oscilloscope and a General Radio model 1192 B digital counter which was operating in the "period times ten" mode. Then the operator visually verified a realization on the storage scope, the counter reading was recorded for later processing. The verification consisted of a visual inspection of the pulse train that triggers the counter to make certain that 10 consecutive pulses (Doppler cycles) were counted. Only pulse trains which represent valid individual realizations were recorded - the remainder were neglected.

A second operator transferred the Doppler periods thus collected to computer cards via an IBM 026 key punch. An IBM 360/65 was then used to calculate the means, root mean squares, and other properties of the recorded data.

Data Corrections

Statistical Biasing

The measurement of mean velocities with a LAMIR is not absolute. The desired quantity, mean velocity, is in fact the time-averaged mean velocity, that is,

$$\overline{U} = \frac{1}{T}\int_{o}^{T} U dt$$

The LAMIR does not measure the time-averaged mean, it measures a value larger than the true time-averaged mean. Recall that the occurrence of

a scattering source in the probe volume is a random event. If the scattering particles are distributed uniformly throughout the flow the number of particles in a fluid volume is proportional to the size of the volume. There is a larger volume of flow, and hence a larger number of scatter centers, flowing through the probe volume when the velocity is faster than the time-averaged mean than when the velocity is lower than the time-averaged mean. This can be seen in Figure 11, where the segment under any portion of the velocity trace is proportional to the volume flow through the probe volume. Figure 12 (from McLaughlin and Tiederman [28]) shows how a typical probability density distribution of the axial velocity component is biased. It is important to note that the spread of the distribution does not change significantly. In fact, McLaughlin and Tiederman (28) indicate that the uncorrected value of the root mean square of this velocity fluctuation is a good estimate of the true value.

The correct method for calculating the time-average velocity is to weight each velocity realization with a function which is proportional to the volume flow through the probe volume (28).

Thus the corrected mean velocity estimate is,

$$\overline{U} = \frac{\sum_{N} \omega_i U_i}{\sum_{N} \omega_i} \qquad (2.1)$$

where $$\omega_i = \frac{1}{|V_i| \gamma_i}$$

The simplest approach to the correction, however, is to use a one-dimensional weighting function instead of the true three-dimensional one.

Thus, assume:

$$\omega_i = \frac{1}{U_i} \tag{2.2}$$

By substituting Equation (2.2) into Equation (2.1) a substantial simplification may be obtained. Namely,

$$\overline{U} = \frac{N}{\sum_{N}^{N} 1/U_i} \tag{2.3}$$

Equation (2.3) may be rewritten as:

$$\overline{U} = \left[\frac{\Lambda}{2 \sin \theta/2}\right] \Big/ \overline{T}_D \tag{2.4}$$

where $\overline{T}_D$ is the average Doppler period.

The Doppler period is measured directly with the system outlined here, and, in fact, the computer routine input data is in Doppler period form. Thus, the biasing correction is accomplished by simply computing the velocity based on the mean Doppler period. This one-dimensional correction was applied to all data reduced here.

Velocity Gradient Biasing

The second correction to the data is needed to account for the presence of significant velocity gradients within the probe volume. The error involved here is due to basically the same principle as the biasing error. That is, the probe volume has finite extent and its outer locations on the average have a larger amount of volume flow. Hence, more particles are passing through that portion of the probe volume. The correction in this case is made to the effective location of the probe volume. The probe location is shifted from the center of the probe volume location to the centroid of the swept volume as shown

in Figure 13. The velocity gradient correction has been made to all data presented herein.

Thus, after both corrections have been made the results will appear as a corrected velocity $\overline{U}$ at an effective probe location, y.

Seed Injection

The laser anemometer measuring individual realizations measures the velocity of the particles entrained in the fluid motion. Therefore it is crucial that these particles be of optimum size such that the intensity of radiation at the Doppler frequency is maximal. It is also important that the seeding particles follow the turbulent motions. Thus the following particle size considerations were made.

Due to the inlet filtering the fluid was essentially free of particles larger than 0.5 microns. For the laser optical system used here, the results of Durst & Whitelaw (29) indicate that the size of the most efficient scattering center is approximately 2 microns. The flow was carefully seeded with a dilute concentration (1 mg/l) of 5-10 micron diameter particles classified from AC Fine Test Dust (ACFTD). ACFTD is primarily sand and is used widely in contamination testing. The distinction between the seeded and non-seeded flow could easily be noted by simply viewing the output of the photomultiplier as seed was being added. When no seed was present the Doppler bursts from particles were on the same level as the background noise. However, when the 5-10 micron ACFTD was added, the Doppler signal levels increased markedly, and in most cases the pedestal excursion was 80% to 100% "filled" with the Doppler frequency signal.

From the results of Hjelmfelt and Mockros (30), a 10 micron diameter sand particle should follow a 2500 Hz fluctuation with an amplitude ratio of 0.95. Most turbulent fluctuations in the low speed water flow described are below 250 Hz, and thus it is felt that the seed chosen is adequate for marking the fluid velocities.

The dilute polymer solutions were always mixed and allowed to sit for 6 to 8 hours before use. The 5-10 micron diameter ACFTD used for seeding purposes would not remain suspended in the fluid for this amount of time - thus a seed-injection system was used (see Figure 14). A concentrated seed slurry (about 250 mg/l) was mixed and injected into the flow loop piping at a rate which would give the desired seed concentration (1 mg/l). The injection flow rates were less that 0.3% of the channel flow rate - thus dilution of the dilute polymer solution was not a problem. The reservoir containing the seed slurry was kept well mixed by jetting the bypass flow of the injection pump into the bottom of the reservoir. The seed slurry was injected into the piping at a tee in the line through a 3/32 inch copper tube placed at right angles to the flow. To insure a uniformity of seed the injection was started prior to the data run.

When pumped operation was used, as in the solvent (water) data runs, seed was sprinkled onto the water surface in the 600 gallon catch tank. The concentration was kept dilute (<1 mg/l) and the continuous recycling of the working fluid kept the particles suspended.

Polymer Solution Characterization

Pressure Drop

A careful characterization of the drag-reducing solutions was performed after each data run. Such a characterization yields an independent verification that the solution did reduce the frictional losses in the channel. In addition, when compared from experiment to experiment, the drag-reduction characteristics give an excellent check on the consistancy of mixing techniques for the dilute polymer solutions.

A prime method of dilute polymer solution characterization is to relate the drag-reducing capability of the solution to the stress encountered in a particular flow. This can be done by conducting pressure drop and flow rate tests for the flow of the solution in a pipe. The pipe pressure drop apparatus used in this study is shown in Figure 15.

The 70 gallon reservoir was filled from the channel piping immediately after the data run. The filling was carefully controlled such that no vigorous agitation, pouring, or splashing of the dilute polymer solution occurred - thus alleviating the possibility of polymer solution degradation. The entire apparatus was constructed of stainless steel, glass and plexiglas. The system contains no pumps and only blowdown flow control was used. The two pipes used were nominally one inch (0.835 inches) and ½ inch (.425 inches) pipes with test section lengths of 113.5 inches and 57 inches respectively. The dashed lines in Figure 15 indicate the plumbing for flow in the one inch pipe, while solid lines denote flow in the ½ inch pipe. The flow meter is accurate to the nearest 1% (0.06 gpm) and the manometer fluid level could be read to within ±0.02 inches of deflection.

Viscosity

Generally people have assumed that the viscosity of dilute polymer solutions were constant, that is, independent of shear rate. This is a particularly poor assumption for the high molecular weight polyacrylamides. Viscosity is used in the determination of the wall-layer variables and in order to maintain a high accuracy measurement, the local value of the kinematic viscosity must be used.

The viscosity of dilute polymer solution used in these experiments was measured as a function of shear rate. Solution samples were taken from the downstream head tank immediately after the data run. Two Couette viscometers (a Brookfield Synchro-Electric Model LVF with the UL adapter and a Fann Model V-G) were used to obtain the shear rate dependence of viscosity. The Brookfield gave shear rates of 14.7, 36.7 and 73.4 sec^{-1}, while the Fann provided shear rates of 170, 340, 511 and 1022 sec^{-1}. In most cases multiple readings were taken at a specific rate of shear. These readings were then averaged. The small dial indication on the Fann viscometer made the readings taken on it susceptible to significant errors - on the order of ±10%.

CHAPTER III

EXPERIMENTAL DATA

This chapter presents the mean and fluctuating velocity data taken with the LAMIR for both solvent and dilute polymer solution flows. Also presented is the polymer solution characterization data.

Generally, the experiments can be classified into two categories: solvent and dilute polymer solution flows. The LAMIR data from the solvent flows was taken in order to demonstrate the standard character of the two-dimensional turbulent flow channel and to illustrate the accuracy of the anemometer used in this research. The velocity data for the dilute polymer solutions, in addition to the polymer solution characterization results is presented in order to provide the basis for a number of developments. Namely, 1) the examination of mean velocity prediction techniques; 2) the inference of the turbulent transport mechanism in dilute polymer flows and 3) a qualitative examination of the effect of the polymer upon a two-dimensional turbulent wall flow.

The general scope of the experiments conducted here is shown in Table III. There are a total of four experiments which used water as the working fluid, and seven wherein a dilute polymer solution was used. The general characteristics of the polymer solutions used are also outlined. The experimental uncertainties present in the data presented are discussed in detail in Appendix A.

TABLE III

SUMMARY OF EXPERIMENTAL SCOPE

Run Designation	Re	$\overline{U}_{AVG}$	U_τ (ft/sec)	$\overline{T}$(°c)	Polymer Characteristics		DR (%)	Date
					Name	Concentration (wppm)		
SOL-14	17,700	1.055	0.065	26	None	0	0.0	5 Jun 73
SOL-15	18,500	1.055	0.065	27.5	None	0	0.0	13 Jul 73
SOL-12	24,700	1.457	0.085	26	None	0	0.0	5 May 73
SOL-13	55,200	3.350	0.175	23-26	None	0	0.0	30 May 73
DPS- 5	20,196	1.239	0.0614	24	AP273	100	31.3	9 Jun 73
DPS- 6	26,373	1.618	0.0750	24	"	"	34.5	21 Jun 73
DPS- 7	44,516	2.676	0.1103	25	"	"	40.4	26 Jun 73
DPS-10	20,582	1.200	0.0625	26.5	837-A	"	23.8	9 Jul 73
DPS-11	37,490	2.185	0.0957	27	"	"	35.4	13 Jul 73
DPS-12	46,037	2.683	0.1105	26.5	"	"	39.9	17 Jul 73
DPS- 9	52,449	3.089	0.1277	26	WSR-301	"	37.8	6 Jul 73

Velocity Measurements in Water

Measurements were made in turbulent channel flow of water in order to establish the "standard" character of the channel. LAMIR measurements were made at four Reynolds numbers (Re); 17,700, 18,500, 24,700 and 55,200. Reynolds number is calculated using the bulk average velocity, $\overline{U}_{AVG}$, and the channel hydraulic diameter, D_H, which is 0.164 feet. The velocity measurements at Re = 18,500 were concentrated in the near-wall region with one data point taken at the centerline. The Re=24,700 data represented a traverse of the entire channel width, whereas the other traverses were made only between one wall and the centerline.

Figure 16 shows the measurements made at a Reynolds number of 24,700 in both the east and west side of the channel. In this figure the y coordinate is non-dimensionalized with the channel half-width, W/2, and the velocities are normalized using the channel centerline velocity, $\overline{U}_{MAX}$. The data confirms the symmetry of the flow and it is in good agreement with the channel data of Hussain and Reynolds (31), which was taken in air at a Reynolds number of 35,400. The velocity data has been corrected for the biasing and velocity gradients errors discussed earlier. The brackets indicate the 95% confidence interval on the mean velocity measurements, while the experimental error in y location is within the data point symbol.

In addition to examining the symmetric character of the channel, the two-dimensionality was also tested. Figure 17 shows the results of these tests. The channel centerline velocity, $\overline{U}_{MAX}$, is plotted as a function of distance below the channel centerline, z, for two Reynolds numbers, 16,600 and 24,400. Figures 16 and 17 indicate that the channel flow investigated here is a symmetric, two-dimensional,

fully-developed turbulent channel flow.

The mean velocity data for all solvent flows is shown in the non-dimensional wall layer coordinates in Figure 18. The Re = 24,700 data in this and subsequent figures were the average values of the data taken on the east and west sides. Except for the Re = 18,500 run the value of the wall shear velocity u_τ, was found by forcing the data at $y^+ > 30$ to fit the expression,

$$U^+ = A \log y^+ + B \qquad (3.1)$$

where A = 5.63, B = 5.0, $U^+ = \overline{U}/u_\tau$ and $y^+ = yu_\tau/\upsilon$. The shear velocity is defined by $u_\tau = [\tau_w/\rho]^{\frac{1}{2}}$. Previous investigations; Hussain and Reynolds (31), Clark (32), Eckelmann and Reichardt (33) and Laufer (34), suggest that the best values for the constants A and B for a two-dimensional channel at the Reynolds number range of interest are those shown. The data for Re = 18,500 was taken as a duplicate of the Re = 17,700 data, however, since no data was taken for $y^+ > 30$ the u_τ from the Re = 17,700 run was used to form the normalized variables. The data runs Re = 17,700 and Re = 18,500 were taken approximately six weeks apart and provide some indication of long term repeatability of the measurements.

Particular attention should be given to two points in Figure 18. The first is the data point at a $y^+ \simeq 3$ and a Reynolds number of 18,500. This point falls above the $U^+ = y^+$ curve even after corrections and confidence intervals have been applied. The reason for this is not totally understood. It is known, however, that the three-dimensional effect of the spanwise velocity fluctuations are most apparent in the near-wall region. The one-dimensional statistical biasing correction

applied to this data point may be insufficient.

The second point in question is the one at $y^+ \simeq 5$ for Re = 55,200. This data was taken using a probe volume whose edge was on the wall and whose center was 0.0023 inches from the wall. The experimental error in y location for this data point is 18% and the confidence interval shown in Figure 18 does include the $U^+ = y^+$ curve. In addition, since the probe is located on the wall, frequencies near zero are to be expected. The band pass filter used in data acquisition had to filter out some of the lower velocity fluctuations. This filtering does not seem to have affected the value of $\overline{U}$, but later figures will show that the turbulent intensity is lowered at this location.

In addition to determining the shear velocity, u_τ, from "forcing" the data to fit a universal profile, (Equation 3.1), it may be computed from the slope of the velocity profile in the near-wall region. Using a y^+ value of approximately six and the fluid properties as they were measured during the run, a "wall slope u_τ" was established. These values, in addition to the "log fit u_τ" values, are shown in Table IV.

TABLE IV

SHEAR VELOCITY COMPARISON-WALL SLOPE AND LOG FIT

Re	Wall Slope u_τ (ft/sec)	Log Fit u_τ (ft/sec)
17,700	0.065	0.069
18,500	0.066	0.069
24,700	0.081	0.085
55,200	0.178	0.175

Both estimates of u_τ are compared with the data of Hussain and Reynolds (31) in Figure 19. It is important to note the good agreement between the two u_τ estimation methods. The polymer data shown later will have a single method of u_τ determination, namely the "wall slope method". The method's validity is considered established by the above comparison.

All mean velocity data presented is corrected for both velocity gradient and biasing errors. Figure 20 shows the magnitude of these corrections. The data shown is the biased and corrected velocity measurement in the near-wall region for the three Reynolds numbers shown. Recall that the bias correction moves the data on the $\overline{U}$ axis while the velocity gradient correction moves it on the y-axis. The normalized results of these corrections are shown in Figure 21 for the near-wall region. These figures show that the velocity gradient correction is significant only when the mean velocity is near zero and/or the probe volume is very close to the wall. The biasing correction is more pronounced and is dependent on the root mean square of the fluctuation level. The biasing correction shown here varies from 16% for a fluctuation level of about 50% to insignificant levels when the fluctuation levels fall below 5%. Figure 21 demonstrates the necessity for corrections to be applied. The data in this region must fit the linear curve $U^+ = y^+$ and this is accomplished only after the statistical biasing and velocity gradient corrections have been made.

The root mean square (rms) estimates of the streamwise velocity fluctuations for the four solvent flows are presented in the next three figures. Figure 22 shows these rms values, u', normalized with the local mean velocity plotted as a function of y non-dimensionalized with channel half-width. Figure 23 shows the turbulent intensities as

a function of the wall layer coordinates. The intensities have been normalized with the u_τ obtained when the mean velocity data was "forced" to fit Equation 3.1. The relevant data of Hussain and Reynolds (31) and Eckelmann and Reichardt (33) are shown for comparison.

The two points discussed earlier should be noted again in Figures 22 and 23. The $y^+ \simeq 5$ data point for Re = 55,200 had some lower frequency fluctuations electronically filtered out and the overall turbulent intensity is, thus, reduced. The data at $y^+ \simeq 3$ for Re = 18,500 has a 95% confidence interval of 11% but remains slightly high. The probe volume size permits measurement of velocity fluctuations over a finite distance normal to the wall. This effect is most pronounced at low y^+ values and high intensity levels, and is most probably the effect seen here.

Velocity Measurements in Drag-Reducing Solutions

Velocity measurements were made in seven drag-reducing flows: three with Separan AP273 as the additive, three with Magnifloc 837-A, and one with Polyox WSR-301. The general parameters for the seven dilute polymer flows and the four solvent flows were presented in Table III. The Reynolds number (Re) is again based on hydraulic diameter and mass-average velocity, but for friction-reducing flows the solution viscosity is replaced by the solvent viscosity at the same temperature. The mass-average velocity, $\overline{U}_{AVG}$, was obtained by integrating the mean velocity profile and u_τ for the dilute polymer solutions was calculated from the velocity gradient in the viscous sublayer. As seen in Figure 18, the experimental solvent data fits the $U^+ = y^+$ curve in the range

$6 < y^+ < 8$. For this reason all calculations of u_τ from velocity gradient (wall slope u_τ) were based on data in this y^+ range.

The experimental program was planned and executed such that a variety of parameters could be employed when comparisons between drag-reducing and solvent flows were being made. For example, with reference to Table III, if one desires a comparison of flow characteristics at a common percentage of drag-reductions, DPS-6, DPS-11 and DPS-9 can be compared; or if Reynold number is the parameter of interest, SOL-12, DPS-6 and DPS-10 can be compared.

The mean velocity profiles for seven drag-reducing flows are presented in Figure 24. One of the most striking differences between various flows can be noted here; that is, the general shape of the profiles for Separan AP273 is quite different than those for Polyox WSR-301 or Magnifloc 837-A. Both 837-A and WSR-301 have a more classical appearance, that is, a lower velocity slope near the wall and a larger flow in the channel center regions (see Rudd [15]). This difference is best demonstrated in the ratio $\overline{U}_{AVG}/\overline{U}_{MAX}$, shown in Figure 25.

The mean velocity data is plotted in non-dimensional wall layer coordinates in Figures 26, 27 and 28. The solid curves representing the locus of solvent velocity measurements are shown for comparative purposes. In all cases, the calculation of y^+ uses a kinematic viscosity based upon the local shear rate. The log portion of the velocity profile appears identical to the solvent data except for a vertical shift. This portion of the mean profile can be described by,

$$U^+ = A \log y^+ + B + \Delta B \qquad (3.2)$$

where $A = 5.63$, $B = 5.0$ and ΔB is the additive constant. A buffer region exists between a y^+ of approximately 10 and the beginning of

the log region. The data suggests a third curve,

$$U^+ = C \log y^+ + D \qquad (3.3)$$

can be used to describe the limiting values on U^+ and y^+ in this region. This limiting function has been named by many as the "ultimate profile", and can be described as the line along which all data fits until it assumes the form of Equation 3.2. The intersection of Equations 3.2 and 3.3 depends upon the specific flow, being investigated. It is important to note that C and D vary from polymer type to polymer type and the slope, C, is less sensitive to change than the intercept D. Also, it is difficult to determine C and D until a sufficient ΔB shift has taken place, thus allowing enough data within the buffer region to clearly define Equation 3.3. The constants C and D which were determined from a "best fit" curve drawn through the data for the highest amount of drag reduction are summarized in Table V.

The velocity data in the near-wall region ($y<8$) can best be seen in Figure 29, which is linear plot of U^+ as a function y^+. The data for y^+ less than 8 fits the $U^+ = y^+$ curve well. The most important aspect of the data presented in Figure 29 is the departure of the mean velocity data from the $U^+ = y^+$ curve for values of $y^+ > 8$-10. This observation is in direct contrast to virtually all previous data, which is best typified by the work of Rudd (15), also shown in Figure 29. However, it should be recalled that all previous laser anemometer measurements have been made in square ducts. The lower dashed curve represents the locus of points representing the solvent velocity measurements and is included for comparative purposes.

TABLE V

SUMMARY OF LAW OF THE WALL CONSTANTS

Run Designation	A	B	ΔB	C	D
SOL-12,13,14,15	5.63	5.00	0	-	-
DPS- 5	"	"	7.19	17.70	-8.20
" - 6	"	"	8.09	"	"
" - 7	"	"	9.20	"	"
" -10	"	"	4.41	16.60	-7.30
" -11	"	"	7.03	"	"
" -12	"	"	8.28	"	"
" - 9	"	"	6.98	17.80	-8.30

The intensity of the turbulent velocity fluctuations in the drag-reducing flows examined here are shown in Figures 30 through 33. Figure 30 shows the root mean square (rms) estimates of the velocity's fluctuation normalized with the local mean velocity as a function of the distance normal to the wall non-dimensionalized with the channel half-width. The intensities for both polyacrylamides show an inflectional behavior at approximately $2y/W = 0.05$, in addition to displaying distinct differences from the solvent data in the outer regions of the flow. This is a real effect and not one that can be attributed to experimental or statistical uncertainty.

The final and most commonly employed method of presenting turbulent intensity information is shown in Figures 31 through 33. In these

figures, u' is normalized with u_τ and is plotted as a function of y^+. The data presented here is shown compared to typical solvent data and the square-duct data of Rudd (15). It can be seen that the data presented here differs significantly from that of Rudd. The distinct peak present in the solvent data has disappeared and the maximum values for u'/u_τ are distributed over a much wider range of y^+. There does not appear to be either an extended linear curve up to a distinct peak or a distinct peak in turbulent intensities - as shown by Rudd, Logan, and Kumor and Sylvester.

Comparisons

The histogram and the energy density function are not widely used methods of data presentation and comparison. However, the laser anemometer measuring individual realizations yields data of a form such that these presentations are formed with little effort.

Typical mean velocity data is presented in histogram form in Figure 34 for solvent and dilute polymer flows. This method of presentation allows a qualitative comparison to be made at a common non-dimensional distance from the wall. The velocity histograms shown extend over the important productive region of the wall layer and were formed using a large number of individual velocity realizations, N, as shown in Table VI. It is believed that these histograms are representative of those in all solvent and friction-reducing flows. The histogram comparisons were made on a Reynolds number basis. The distinct differences in the drag-reducing and solvent data at low values of y^+ and the merging of the histograms at higher y^+ should be noted.

TABLE VI

HISTOGRAM SAMPLE SIZES

RUN	y^+	N	POLYMER
SOL - 13	9.2	1001	-
"	17.9	1028	-
"	35.4	1014	-
DPS - 9	8.4	816	WSR-301
"	19.0	1019	"
"	29.4	951	"
DPS - 7	8.5	1001	AP273

The energy density function may be defined as,

$$\xi(u) \equiv u^2 p(u) \tag{3.4}$$

where p(u) is the probability density function. Uzkan and Reynolds (35) have pointed out that a plot of $\xi(u)$ as a function of u identifies the contributions of specific fluctuation magnitudes to the energy of the turbulence.

In order to obtain a detailed representation of the energy density function one must have a sample size of sufficient number such that the outermost parts of hte histogram and energy density function are well defined. It is estimated that sample sizes on the order of 5000 - 10,000 would be sufficient to give such detail. The manual data reduction used here precludes extensive documentation of energy density results - but some qualitative results are presented to show the value of this type of data presentation. The results shown in Figures 35, 36 and 37 are for the velocity measurements outlined in Table VI. It

is estimated that sample sizes on the order of those of Table VI are sufficient to give qualitative results. The regions which would suffer greatest would be those furthest from the origin.

Despite the small sample size one should note that differences in the dilute polymer and solvent data can be seen through the productive region of the flow ($5 < y^+ < 50$). (See Figures 35, 36 and 37.) The results for the solvent flow are in agreement with those of Uzkan and Reynolds (35). The comparison is made here on the basis of common Reynolds number. The Polyox WSR-301 curves are seen to continue rising through a y^+ of 35, whereas the solvent energy density functions have reached a maximum and are falling.

Eddy Diffusivity

A natural computational extension using mean velocity profile data is the determination of the eddy diffusivity. An expression for eddy diffusivity characterizes the momentum transport properties of the flow. These properties, or the amount of turbulent mixing, are useful in the analysis of turbulent heat transfer. The concept is to use the experimental velocity profile and the equations of motion to determine free constants in an assumed model for the eddy diffusivity of momentum. Then the temperature profile and the heat transfer coefficient can be predicted using the energy equation and equating the eddy diffusivities of heat and momentum.

The eddy diffusivity models provide an expression that replaces the non-linear Reynolds stress term in the equations of motion. Consequently, the eddy diffusivity of momentum is defined as,

$$E(y) = \frac{\varepsilon}{\upsilon} = \frac{-\overline{u'v'}}{\upsilon \dfrac{d\overline{U}}{dy}} \tag{3.5}$$

and the non-dimensional, time-average equation of motion for fully-developed, two-dimensional channel flow becomes

$$\overline{P} = \frac{1}{R} \frac{d}{dy'}\left[(1+E) \frac{d\overline{U}'}{dy'}\right] \tag{3.6}$$

The non-dimensionalization was performed using the mass-average velocity, $\overline{U}_{AVG}$, and the channel half-width, W/2. $\overline{P}$ is defined as $\overline{P} = \tau_w/\rho\overline{U}^2_{AVG}$ and the Reynolds number is $R = W\,\overline{U}_{AVG}/2[\upsilon]_{SOL}$. Equation (3.6) may be integrated once to yield,

$$\overline{U}'(y') = R\overline{P} \int_0^{y'} \frac{1-y_1}{1+E(y_1)}\, dy_1 \tag{3.7}$$

and the normalization requires that,

$$1 = \int \overline{U}'(y')dy' = R\overline{P} \int_0^{1} \int_0^{y'} \left[\frac{1-y_1}{1+E(y_1)}\, dy_1\right] dy' \tag{3.8}$$

Equation (3.7) demonstrates that the velocity profile may be calculated from a simple integration if the eddy diffusivity distribution is known. Most eddy diffusivity models contain some free constants which are determined by requiring $\overline{U}'(y')$ from Equation (3.7) to agree with the experimental data.

The model used here was first recommended by Cess (36) for turbulent pipe flow. The Cess model has the advantages of being a continuous function which yields non-zero velocity fluctuation levels at the center of the channel (or pipe) flow. When the Cess expression has

been adapted for channel flow it appears as (see Tiederman & Reynolds [37]),

$$E = \frac{1}{2}\left[1+\frac{k^2R^2\overline{P}}{9}\left[2y'-y'^2\right]^2\left[3-4y'-2y'^2\right]^2\left[1+\exp\left(\frac{-y'R\sqrt{\overline{P}}}{A^+}\right)\right]^2\right]^{\frac{1}{2}} - 1/2 \qquad (3.9)$$

The free constants are A^+ and k.

In order to compute E(y') and $\overline{U}'(y')$ for solvent flows one must know the Reynolds number (R) of the flow. The values of A^+ and k are picked (see Hussain and Reynolds [31]) and the starting value of $\overline{P}$ must be calculated. The initial value of $\overline{P}$ is approximated from an expression for turbulent pipe flow (see Kays [38]), which when modified, appears as

$$\overline{P} = 0.0177\ [R]^{-0.2} \qquad (3.10)$$

The values R, A^+, k and $\overline{P}$ are the input parameters to an iterative computer scheme. Within the iterative program, E(y') and $\overline{U}'(y')$ are computed from Equations (3.9) and (3.7) respectively. Equation (3.8) is then used to compute an updated $\overline{P}$ which is used to restart the calculation of E(y') and $\overline{U}'(y')$. The updating (iteration) of $\overline{P}$ continues until the normalization condition yields a $\overline{P}$ which has a sufficiently small error when compared to the previous $\overline{P}$ iteration. The mean velocity profile generated in this manner may now be compared with the experimental data. If the agreement is poor the values of A^+ and/or k are adjusted and the entire procedure must be repeated. Here the numerical integrations were performed using a Simpson's 1/3 rule with 400 integrational increments. 400 intervals proved satisfactory since an increase to 1000 intervals gave no significant changes.

This scheme was implemented for the solvent flows in order to test

the model and to verify the computer routine. Various values of A^+ and k were used to determine a family of $E(y')$ and $\overline{U}'(y')$, which were compared to the experimental velocity profiles. The values of $A^+ = 29$ and $k = 0.45$ were found to yield a $\overline{U}'(y')$ which best fit the experimental data. These results are identical to those found by Hussain and Reynolds (31) for a similar channel flow.

Figure 38 shows the comparison between the solvent data and the calculated mean velocity profiles using the Cess model and $A^+ = 29$, $k = 0.45$. The agreement is good at all Reynolds numbers. Figure 39 then displays the non-dimensional eddy diffusivity given by the Cess model. These results are in agreement with those of Tiederman and Reynolds (37) and Hussain and Reynolds (31).

The <u>form</u> of the model employed here for the determination of the turbulent transport properties for drag-reducing flows is the same as that for solvent flows, that is; the Cess model. However, the iteration scheme is changed because a single value of $\overline{P}$ from the experiment must be used for each flow.

The inputs are again R, $\overline{P}$, k and A^+, but some very important differences exist in their assignment. The viscosity of the dilute polymer solution is used in calculating the Reynolds number, R. The value of k is set at 0.45 and not allowed to vary because 1/k is proportional to the slope of the log portion of the universal law of the wall. Recall that in a drag-reducing flow it has been established that the <u>slope</u> of the log portion is the same as the solvent slope. $\overline{P}$ cannot be evaluated from Equation (3.10) for dilute polymer flows, but the definition of $\overline{P}$ yields a working equation directly. Namely,

$$\overline{P} = \frac{\tau_w}{\rho \overline{U}_{AVG}^2} = \left[\frac{u_\tau}{\overline{U}_{AVG}}\right]^2 \qquad (3.11)$$

Thus, for drag-reducing flows $\overline{P}$ is calculated using pressure-drop and flow rate data and it remains constant for the entire analysis. A^+ is the only input parameter which is determined by iteration.

The computational scheme begins with R and $\overline{P}$ fixed by the experimental conditions, k = 0.45, and an initial value of A^+.

The distributions of $E(y')$ and $\overline{U}'(y')$ are computed using Equations (3.9) and (3.7). The value of $\overline{P}$ obtained by using Equation (3.8) is compared to the experimental value from Equation (3.11). If the error is large, the value of A^+ is changed and the entire process is repeated. The cycle continues until the value of $\overline{P}$, which satisfies the normalization condition (Equation [3.8]), is the same as the experimental value. The velocity profile generated in this manner is then compared to the experimental data. However, note that there are no free parameters unless the condition k = 0.45 is relaxed. This is important because if the calculated profiles agree with the experimental data the computational scheme becomes a prediction technique for drag-reduction velocity profiles.

Mean velocity profiles were predicted for all seven drag-reducing flows discussed in this research. The actual experimental parameters were used in the determination of Reynolds number and $\overline{P}$. The results of these predictions are compared to the experimental data in Figures 40, 41 and 42. The agreement is excellent. The values of A^+ which resulted from the calculations are shown in Table VII. It should be noted that the values of A^+ for each run are comparable to the y^+

values at the intersection of the log and buffer regions for that corresponding run (see Figures 26, 27 and 28).

TABLE VII

CONSTANT FOR DRAG-REDUCED EDDY DIFFUSIVITY

Run	A^+
DPS- 5	72.8
DPS- 6	76.0
DPS- 7	92.2
DPS-10	54.6
DPS-11	71.4
DPS-12	80.0
DPS- 9	71.3

The eddy diffusivity model outlined here and applied to the dilute polymer flows is plotted in Figures 43 and 44. The eddy diffusivity of the Polyox WSR-301 has the greatest magnitude, while the diffusivity for Magnifloc 837-A is suppressed somewhat and the Separan AP273 diffusivity is the lowest of all drag-reducing polymer results. In addition, it should be noted that the eddy diffusivity data for the AP273 reaches a maximum at the channel center, which is different than the behavior for either the solvent or the other dilute polymer flows.

The diffusivity distributions at comparable Reynolds numbers for solvent and drag-reducing flows are compared in Figure 45.

Polymer Solution Characterization

Drag Reduction

A careful characterization of the drag-reducing solution was performed after each data run. Pressure drop and flow rates tests were conducted and the drag-reducing capabilities of the solution were obtained. These measurements are an excellent indication of the degradation (if any) of the dilute polymer solution. In addition, they can be used as an indication of the repeatibility of polymer solution mixing techniques. The drag-reduction data is more fully documented and presented in Appendix B.

Viscosity

In most of the previous dilute polymer experiments the viscosity of the solution was assumed to be independent of the shear rate. The physical appearance of the 100 wppm solutions of Separan AP273 suggested that a more extensive examination of the viscosity of the dilute polymer solutions was needed. As mentioned previously, the viscosity of the dilute polymer solutions was measured over a shear rate range of 15 sec^{-1} to 1000 sec^{-1} by using two Couette viscometers, a Brookfield Synchro-Electric Model LVF and a Fann model V-G. The maximum possible shear rate for each viscometer yields the most accurate data, thus more emphasis is placed on the readings at 1022, 73.4 and 36.7 sec^{-1}.

The viscometric data is shown in Figure 46. For the 31.3% drag-reducing solution for AP273 (the first data run), only a single viscometer reading was taken. More careful documentation of later AP273

polymer solutions indicated that a "family" of curves described the shear rate dependence of the viscosity for 100 wppm solutions. A curve belonging to this family was constructed for the single data point mentioned above. Thus the viscometric curve for the 31.3% drag-reducing solution of AP273 is an approximation.

It is interesting to note the degree of non-Newtonian properties for these fluids. The polyacylamides are most pseudoplastic while the polyethlene oxide is more Newtonian in its behavior. All solutions approach Newtonian behavior at lower shear rates ($<100 sec^{-1}$), but most flows have shear rates above this value.

CHAPTER IV

DISCUSSION

The interpretation and discussion of the results can be divided into two general sections, namely, the mean velocity results and the turbulent velocity fluctuation results. The mean velocity results in the drag-reducing flows and their relationship to previous results will be discussed in two general ways. First, the velocity profile will be divided into the three characteristic regions and each region will be discussed. The regions are the viscous sublayer, the buffer region and the log portion. Secondly, the predictive technique for the calculation of the velocity profile and the turbulent transport mechanisms in the drag-reducing flows will be discussed.

The turbulent intensity information will be compared to previous results and will be used to demonstrate the importance of the buffer region in drag-reducing flows. In addition, some qualitative judgements will be made about the structure of a drag-reducing flow from the energy density representation of the velocity fluctuation results.

Mean Velocity

The purpose of this section is to examine and interpret the mean velocity measurements for the dilute polymer flows. References to previous investigations will be made when necessary and possible, but it must be recalled that such comparisons are between the data from a

two-dimensional turbulent channel flow and that of an experiment conducted in a square duct.

The results of this study generally show the existence of the three regions in a drag-reducing turbulent boundary layer. The three-region concept constitutes an apparently rather widely accepted (not necessarily proven) picture of drag-reducing flows. A general description of these three regions follows:

1. Viscous Sublayer: The near-wall portion of the boundary layer, where viscous forces predominate and the velocity profile is linear. The non-dimensional velocity profile in this region is described by the linear relationship $U^+ = y^+$ (see Figure 47).

2. Log Region: The outer portion of the turbulent wall layer. The log region for drag-reducing flows has been shown to fit the expression $U^+ = A \ln y^+ + B + \Delta B$ (see Figure 47). ΔB is an additive constant and represents a vertical shift in the log portion of the velocity profile. The constants A and B, ($A = 1/k$) are equivalent to those for a solvent flow. The mean velocity in this portion of the flow appears to be equivalent to a Newtonian flow. This region is apparently outside the major dynamic influence of the polymer additives.

3. Buffer Region (Elastic Sublayer): The region joining the viscous sublayer and an elevated log region. A typical curve, $U^+ = C \ln y^+ + D$, (see Figure 47), describes the buffer region. At high amounts of drag-reduction the velocity curve within the buffer region describes what some researchers refer to as the "ultimate profile" (see Virk (21), Tomita (19)). The buffer region is the zone in which the effect of the polymer additives is seen most dramatically. The shape of the profile within the buffer region and its junction with the viscous sublayer are areas of wide data scatter.

The measurements made here allow a detailed examination of each of these regions.

The extent of the linear curve, $U^+ = y^+$, in the near-wall region is the first area of discussion. A controversy exists concerning so-called "sublayer thickening" which is represented by the velocity

profile remaining linear to a y^+ = 15 to 20 instead of the solvent value of 8 to 9. Four investigations, including this one, have made velocity measurements at $y^+ \leq 10$. For convenience, Table VIII indicates the extent of the linear curve and the lowest y^+ location at which velocity measurements were made in each of these investigations.

TABLE VIII

COMPARISON OF NEAR-WALL LASER ANEMOMETER MEASUREMENTS IN DRAG-REDUCING FLOWS

Author	Maximum y^+ for which $U^+=y^+$	Lowest y^+ Measurements
Logan (11)	10	10
Rudd (15)	19	8
Kumor & Sylvester (10)	16	3
Present Work	9	3

Past efforts show considerable scatter which may be a result of their experimental facilities. Recall that these investigators utilized square ducts. The present work demonstrates that the linear portion of a drag-reducing velocity profile has the same non-dimensional extent as that of a solvent profile, and that the velocity profiles leave the $U^+ = y^+$ curve at a different slope than the companion solvent data (see Figure 29). It must be concluded from this study that the linear

portion of the velocity profile extends to a y^+ of about 9, which determines the extend of the viscous sublayer. Thus, the non-dimensional mean velocity data for a drag-reducing and solvent flow in the near-wall region are equal and the polymer additives do not yield a thickened viscous sublayer.

The buffer region of the velocity profiles shown in Figures 26 through 28 have been described by the equation $U^+ = C \log y^+ + D$ where C and D are tabulated in Table V. The formulation of an equation which is designed to describe an "ultimate profile" using these values is not justified because the range of drag-reductions was insufficient. However, some qualitative characteristics can be noted. The slopes of the fitted profiles within the buffer region agree to within 7%, which implies that there exists a constant $C = 1/k'$, which describes the slope of a universal profile in the buffer regime. A more extensive series of experiments at high drag-reductions would provide a crucial input to the characterization of a so-called "ultimate profile".

The buffer region is obviously a region wherein the polymers have a strong influence on the mean velocity profile. In fact, Figures 26, 27 and 28 show that the log region and viscous sublayer of the dilute polymer flows are similar to those of water, but the buffer regions vary widely. The mean flow characteristics are altered in the buffer region.

The logarithmic region of the mean velocity profile for a drag-reducing flow is shifted by an amount ΔB due to the change in the buffer region profile (see Figure 47). The results presented herein made it possible to directly measure ΔB and consequently to test the available ΔB predictive schemes. The experimental values of ΔB were

shown in Table V. The various methods of ΔB prediction and their origin are shown in Table IX.

The basis for the predictive methods can be divided into three general categories. First, the length-scale models, wherein van Driest (39) and Meyer (40) use characteristic lengths such as sublayer thickness, buffer region thickness, pipe diameter, etc. The time-scale models form a second group of ΔB predictors. These models are typically the ratio of a polymer characteristic time (relaxation time, critical shear rate, etc.) and a characteristic flow time based on wall parameters. They form the basis for the works of Elata (4), Tomita (19), Seyer and Metzner (16), and Rudd (15). The predictor of Virk, et al. (21) is composed of general flow parameters, such as $\overline{U}_{AVG}$ and u_τ.

In the case of Elata, ΔB cannot be obtained from experimental data because the value of α is unknown. However, it has been hypothesized by Elata that α is a function of polymer species and concentration, and thus α would be a constant for each polymer species tested here. This feature can be examined with the experiments. Figure 46 demonstrates that the predicted α is a strong function of ΔB and not a constant.

For the remaining schemes, predicted value of ΔB can be found based upon the experimental conditions; this value may then be compared to the actual ΔB determined from the measured velocity profiles. These comparisons, in addition to the α results of Elata's model (4), are the subject of Table X. Table X is graphically presented in Figures 48 and 49. It can be seen from these two figures that the predicted and actual values are widely scattered and not in good agreement. They are, at times, consistant within a limited scope (e.g. a single polymer,

TABLE IX

ΔB PREDICTORS

Author	Predictor
Elata, et al. (4)	$\alpha \ln \frac{t_1 u_\tau^2}{\upsilon}$
Meyer (40)	$\frac{\overline{U}_{AVG}}{u_\tau} - 2.5 - 5.66 \log \frac{du_\tau}{2\upsilon_w}$
Tomita (19)	$K_1 \ln y_1^+ = K_2$
Virk, et al. (21)	$([\overline{U}_{AVG}]_{DPS} - [\overline{U}_{AVG}]_{SOL}) / u_\tau$
Rudd (15)	$12 D' - 2.44 \ln D' - 11.5$
van Driest (39)	$\frac{1}{k_1} - \frac{1}{k} \ln L^+ + B' - 5.0$
Seyer & Metzner (16)	$\Delta B (t_1) = y_1^+ - A \ln y_1^+$

TABLE X

COMPARISON OF ACTUAL TO PREDICTED VALUES OF ΔB

Run	Re	ΔB							α
		Actual	Tomita	Virk	Rudd	van Driest	Meyer	Seyer	Elata
DPS- 5	20,196	7.2	4.4	4.2	7.7	4.6	5.7	7.7	24.0
DPS- 6	26,373	8.1	5.0	4.9	10.5	5.2	6.3	8.9	17.1
DPS- 7	44,516	9.2	6.0	4.5	18.4	6.2	8.4	14.3	11.4
DPS-10	20,582	4.4	1.3	3.0	4.8	1.4	4.3	7.8	13.6
DPS-11	37,490	7.0	3.6	3.7	15.1	3.8	6.4	11.8	10.1
DPS-12	46,037	8.2	4.7	4.5	18.6	4.9	7.5	14.5	10.1
DPS- 9	52,449	7.0	3.4	5.8	8.4	5.6	6.9	7.9	20.2

a single flow rate, etc.). Of the seven methods of ΔB prediction reviewed, the one of Meyer is superior, even though it has discrepancies on the order of 25%. The applicability of any of these aforementioned predictors to a wide range of flows and polymer species is not practical.

Further attempts have been made to simply correlate (not predict) ΔB using the characteristic time based on wall parameters, and fundamental flow time-scales, such as polymer relaxation time, t_1, or the time between bursts, $\overline{T}_B$. (See Donohue, et al.(41)). These two characteristic times are fundamental measures of the identity of a specific flow. The ratios $\upsilon/u_\tau^2\ \overline{T}_B$, $\upsilon/u_\tau^2\ t_1$, $\upsilon/u_\tau^{*2}\ \overline{T}_B$ and $\upsilon/u_\tau^{*2}\ t_1$, were computed and plotted as a function of ΔB and drag reduction percentage. No correlation was present.

The predictors based upon length-scales used thus far, namely those of van Driest and Meyer, have not used the fundamental wall-region length in an attempt to collapse the ΔB data. This fundamental length is the low-speed streak spacing, λ, and the normalized spacing is $\lambda^+=\lambda u_\tau/\upsilon$. For the correlation attempts made here λ^+ was obtained from Donohue, et al. (41), λ was then calculated using experimental values of u_τ and υ. The parameters λ and λ^+ were plotted versus ΔB. A correlation was not present - thus a wall-layer length scale does not appear to be the basis for ΔB prediction. The radius of gyration of the polymer molecule is an attractive correlation parameter, but the complexity of the molecules makes experimental determination of the radius of gyration inaccurate.

In lieu of a time or length scale correlation there exists the possibility of ΔB correlation on flow parameters (e.g. $\overline{U}_{AVG}$, per cent drag-reduction, etc.). At the onset of this work it was thought that

ΔB data would collapse to a single curve when plotted as a function of percent drag-reduction. This is not the case. The data does collapse into a family of parallel curves (see Figure 50) if one assumes that the single data point for Polyox WSR-301 indicates a curve. Thus, drag-reduction only partially correlates the ΔB parameter.

The correlative attempts here have shown that ΔB may be predicted nicely when a single polymer type is considered. Previous workers have implied universal correlations based upon single polymer species investigations and implicit assumptions about how the polymer molecules affect the flow. It has been shown that these predictors are inadequate. A sound engineering approach would be development of a model which predicts the entire mean velocity profile even if the model yielded little insight into mechanism.

Using the calculation scheme outlined in Chapter III, the use of the Cess (36) model for turbulent diffusivity allows a prediction of the mean velocity profile for a drag-reducing flow to be made. These predictions are based upon knowledge of u_τ, U_{AVG} and υ.

The velocity profile calculations were made herein (see Figures 40, 41, for example) for seven drag-reducing flows with three polymer species and a range of drag-reductions from 24 to 40%. It <u>cannot</u> be implied that this type of prediction technique will withstand the tests of universality, but it does appear to have important engineering usage. The ΔB derived from the mean velocity profile predictions is compared to the experimental values in Table XI. The agreement is excellent. Table VII shows the values of A^+ which are obtained for each calculated mean velocity profile. These values indicate that A^+

TABLE XI

RESULTS OF ΔB PREDICTION USING CESS MODEL

Run	Experimental ΔB	Model ΔB	$A^+/\Delta B$
DPS- 5	7.2	7.3	10.2
DPS- 6	8.1	8.0	9.4
DPS- 7	9.2	9.4	10.0
DPS-10	4.4	4.8	12.5
DPS-11	7.0	7.2	10.2
DPS-12	8.2	8.4	9.8
DPS- 9	7.0	6.9	10.1

is, in general, an indication of the non-dimensional extent of the combined buffer region and viscous sublayer. The ratio of A^+ to the experimental value of ΔB is shown in Table XI. Excluding one value the ratio is constant to within 6%. The reasons for the ratio being constant are not understood, but they are undoubtedly related to the non-dimensional mean velocity slope in the buffer region.

It should be reiterated that a predictive scheme for the mean velocity profile has been shown to be valid for a variety of drag-reducing flows. The ΔB parameter may be found directly from the predicted mean velocity profile. In addition, the constant A^+ gives a reasonable estimate of the buffer region's thickness.

The original intent in using the expression of Cess (36) was to determine its validity in predicting the turbulent transport properties of drag-reducing flows. The distribution of eddy diffusivity is critical in the determination of the momentum, heat and mass transfer through a shear flow. The Cess expression is extremely practical in

that it is a continuous expression and yields the correct velocity gradient and a finite fluctuation level in the outer stream.

Useful interpretations can be made from the results of the diffusivity calculations. Figure 45 compares the calculated eddy diffusivities for water and dilute polymer flows with equivalent Reynolds number. The major point of interest here is the reduced turbulent mixing in the dilute polymer flows. The reduced mixing has been noted by others, in the form of reduced heat transfer coefficients (see Gupta et al. (42) and Latto and Shen (43)). This should be expected because for moderate Prandtl number fluids the eddy diffusivity of heat is equal to the eddy diffusivity of heat. This single input (eddy diffusivity) coupled with the energy equation and appropriate boundary conditions would be sufficient for calculating the decreased heat transfer rates.

Turbulent Intensities

The use of the LAMIR and experimental facility described earlier permitted unambiguous measurements of streamwise turbulent intensities to be made. The results shown here are believed to be indicative of the effect of polymer additives on the turbulent intensities in a general two-dimensional turbulent boundary layer. The results differ quite widely from those presented by Rudd (15), Kumor and Sylvester (10) and Logan (11), and due to the experimental differences in these works, only qualitative comparisons can be made.

Figures 31, 32 and 33 most dramatically present the differences in the intensity measurements. Rudd's data is shown and it is typical of Logan's and Kumor and Sylvester's measurements. The data from this

study shows the general effect of polymer addition (as shown by Figures 31, 32 and 33) is a loss of the distinct peak of the solvent case and a redistribution of the primary turbulent activity into a broad band. Note that the turbulent intensities in the near-wall region ($y^+ < 9$) are reduced. The motion pictures of Donohue and Tiederman (44) confirm this change in the near-wall region of a drag-reducing flow. The dye injected at the wall showed a suppression of activity in the turbulent structure - that is, the dye was distributed much more evenly and the distinct features (such as low speed streaks) became less identifiable and blended better into their surroundings.

The energy density function is another method of visualizing the viewpoint offered here. Recall that Figures 35, 36 and 37 are representative of the turbulent kinetic energy at various y^+ locations of both solvent and drag-reducing flows. The curves themselves indicate the amount of energy contributed to the total from a specific magnitude of velocity fluctuation. The redistribution of turbulent activity is again seen by noting that as one moves away from the wall the energy content gradually increases, peaks at about $y^+ = 40$, and gradually decreases as the outer flow regions are approached. Whereas energy content of the water flow peaks at $y^+ = 10$ to 30, in accordance with the results of Uzkan and Reynolds (35).

Kline, et al. (45) have shown that the buffer region is a narrow region ($8 < y^+ < 30$) of intense turbulent action in a non-drag-reducing flow. The largest values of turbulent kinetic energy production occur at $y^+ \approx 12$ as shown by Kim, et al. (46). The peak in the turbulent intensity plot u'/u_τ occurs at the same location. Thus the buffer region and turbulent production are intimately related. For a drag-

reducing flow the peak which represents maximum energy production has moved away from the wall and has become much broader, which implies a "buffer layer thickening". Recall that the viscous sublayer was not thickened. The log region of the profile has been shown to remain essentially the same in both the mean and fluctuating sense. It appears then that the alteration to the flow by polymer addition is in the productive region, or the buffer region.

It is now established that the polymer additives serve to reduce the production of turbulence (see Donohue, et al. (41)) and to broaden the buffer region which is the turbulence productive region of the flow. How the polymer additives make their presence felt so strongly in the buffer region is not known at this time. It is clear, however, that the region of concern should be the buffer region. The changes to turbulent production are being made in this region, and further probing should be concentrated there.

CHAPTER V

SUMMARY AND CONCLUSIONS

Summary

The laser anemometer measurements conducted here yielded accurate mean and fluctuating velocity profiles for seven drag-reducing flows. This data was sufficient for 1) developing a prediction scheme for the turbulent transport of momentum and consequently prediction of the mean velocity profile, 2) providing an experimental datum for testing phenomenological models of drag-reduction, and 3) providing a further understanding of the drag-reduction mechanism.

A large amount of data was taken with a laser Doppler anemometer in both solvent and dilute polymer flows. The data obtained in water verified the standard character, two-dimensionality and symmetry of the flow channel constructed for these measurements. Velocity measurements were made in drag-reducing flows in which parametric changes were systematically made in both the polymer properties (molecular weight) and flow conditions (drag-reduction). Extreme care was taken in the documentation of the experimental facility and in the data collection and reduction. In addition, corrections were applied to the data to account for both statistical and velocity gradient biasing.

The data for the drag-reducing flows can be compared to previous drag-reducing results and to the equivalent solvent flows. The summaries of the comparison made for each of the objectives follows.

Mean Velocity and Transport Property Calculations

For the range of drag-reductions encountered here, the mean velocity measurements confirm the concept of three zones within the turbulent wall layer. The use of a Cess (36) model and the knowledge of basic flow parameters permits the prediction of the mean velocity profile and consequently the turbulent transport properties. The calculation procedure can be outlined as follows.

The flow parameters needed are u_τ, υ, and U_{AVG}. The kinematic viscosity may be obtained using standard viscometric techniques. The quantity $\overline{U}_{AVG}$ can be obtained by simply knowing the flow rate. The shear velocity, u_τ, is obtained using pressure drop measurements and a momentum analysis. The actual calculation procedure is discussed in Chapter III. The numerical analysis results in a predicted mean velocity profile, $\overline{U}(y')$, and an eddy diffusivity distribution $E(y')$. The calculated $\overline{U}'(y')$ is in good agreement with the experimental data and the final value of A^+ in the Cess expression is an indication of the buffer region thickness. The eddy diffusivities for drag-reducing flows showed a lower magnitude and a maximum point shifted slightly away from the wall. The technique is of engineering usefulness and should be tested at higher amounts of drag-reduction and over a more exhaustive sample of polymer species.

ΔB Prediction

The ability of seven models to predict the ΔB parameter was tested and shown to fail. The plotted mean velocity profile generated using the predictive scheme developed in this thesis yields a ΔB that is

In excellent agreement with the experimental values. It must be noted that the prediction of ΔB when given the entire velocity profile from the above prediction is straightforward.

Mean Flow and Turbulent Intensities

Considerable velocity measurements were made in the near-wall region of the dilute polymer flows. The results indicate that the viscous sublayer ($y^+ < 10$) has mean velocity characteristics very similar to that of a solvent flow. In addition, for the drag-reductions encountered here (% DR < 40) no linear sublayer thickening is shown. Instead, the thickening effect takes place in the buffer region. Finally, the log region appears to have the same slope as the solvent flows but is displaced upward. Joining the individual parts, one obtains a mean velocity profile with a thickened buffer region which joins a sublayer to an elevated log region.

The turbulent intensities measured herein are in agreement with the past visual observations. Both indicate a loss of distinct features in the flow. For example, the distinct peak present in the solvent intensity profiles is not present. The drag-reduced intensity profile has a broad peak which is displaced outward from the wall. The intensity measurements also compliment the eddy diffusivity predictions, that is, the reduced eddy diffusivity implies reduced turbulent activity and the reduced intensities of the turbulent fluctuations confirm this finding. Furthermore, the limited results obtained from the energy density representation of the velocity support the finding that the flow lacks distinct features.

Conclusions

The major conclusions of this study can be stated as follows:

1. The model proposed by Cess (36) for the turbulent transport of momentum (eddy diffusivity) can be utilized in the prediction of turbulent diffusivities for dilute polymer flows. The model may also be utilized in the prediction of the mean velocity profile for a drag-reducing flow. The model is simple, straightforward and requires only information about the general flow parameters.

2. The eddy diffusivity for a drag-reducing flow is reduced from that of a comparable solvent flow. This implies reduced turbulent mixing and reduced heat transfer coefficients.

3. The methods previously proposed for prediction of the mean velocity profile shift lack universality. This deficiency is apparent in their inability to predict the ΔB shift for dilute polymer flows where the polymer species and drag-reduction were varied. The prediction technique outlined here does predict ΔB well, as well as the remainder of the mean velocity profile.

4. The near-wall velocity measurements have shown that, at least for drag-reduction of 40% or less, the viscous sublayer, indicated by a linear velocity profile, is of the same extent as a comparable solvent flow. There exists no evidence of a thickened sublayer.

5. The effect of the polymer additives is to redistribute the turbulent motion into a broader buffer region. The intensity of the turbulent velocity fluctuations are decreased when compared to a solvent flow of equivalent Re. There are indications that the region of maximum kinetic energy production is moved outward and is distributed more evenly than it is in a solvent flow. This phenomenon was present regardless of polymer species or amount of drag-reduction.

SELECTED BIBLIOGRAPHY

(1) Lumley, J.L. "Drag Reduction by Additives." Annual Review of Fluid Mechanics, Vol. 1 (1969), p. 367.

(2) Hoyt, J.W. "The Effects of Additives in Fluid Friction." Freeman Review, Trans. of the ASME, Series D, J. of Basic Engineering, Vol. 94 (1072), pp. 258-285.

(3) Chung, J.S., and W.P. Graebel, "Laser Anemometer Measurements of Turbulence in Non-Newtonian Pipe Flows." Physics of Fluids, Vol. 15, N. 4 (1972), pp. 546-554.

(4) Elata, C., J. Lehrer, and A. Kahanovitz, "Turbulent Shear Flow of Polymer Solutions." Isreal J. of Tech., Vol. 4, N. 1 (1966), pp. 87-95.

(5) Ernst, W.D. "Investigation of the Turbulent Shear Flow of Dilute Aqueous CMC Solutions." AIChE J., Vol. 12 (1966), p. 581.

(6) Giles, W.B. "Similarity Laws of Friction-Reduced Flows." J. Hydronautics, Vol. 2, N. 1 (1968), pp. 34-40.

(7) Goldstein, R.J., R.J. Adrian, and D.K. Kreid, "Turbulent and Transition Pipe Flow of Dilute Aqueous Polymer Solutions." I & EC Fund., Vol. 8, N. 3 (1969), pp. 498-502.

(8) Goren, Y., and J.F. Norbury, "Turbulent Flow of Dilute Aqueous Polymer Solutions." Trans. of the ASME, Series D, J. of Basic Engineering, Vol. 89 (1967), p. 814.

(9) Killen, J.M., and J. Almo, "Experimental Study of Effects of Dilute Solutions of Polymer Additives on Boundary Layer Characteristics." Viscous Drag Reduction, C.S. Wells, ed. New York: Plenum Press, 1969.

(10) Kumor, S.M., and N.D. Sylvester, "Effects of a Drag-Reducing Polymer on the Turbulent Boundary Layer." Drag Reduction, AIChE Symposium Series, Vol. 69, N. 130 (1973), pp. 1-13.

(11) Logan, S.E. "Laser Velocimeter Measurement of Reynolds Stress and Turbulence in Dilute Polymer Solutions." (Unpub. PhD. Thesis, California Institute of Technology, 1972).

(12) Nicodemo, L., D. Acierno, and G. Astarita, "Velocity Profiles in Turbulent Pipe Flow of Drag-Reducing Liquids." Chem. Engr. Science, Vol. 24 (1969), p. 1241.

(13) Patterson, G.K., and G.L. Florez, "Velocity Profiles During Drag Reduction." Viscous Drag Reduction, C.S. Wells, ed. New York: Plenum Press, 1969.

(14) Rollin, A., and F.A. Seyer, "Statistical Analysis of Instantaneous Velocities in Turbulent Flow of Dilute Viscoelastic Solutions." Presented at Symposium on Turbulence in Liquids, Univ. of Missouri at Rolla, 1973.

(15) Rudd, M.J. "Velocity Measurements Made with a Laser Dopplermeter on the Turbulent Pipe Flow of a Dilute Polymer Solution." J. Fluid Mech., Vol. 51, part 4 (1972) pp. 673-685.

(16) Seyer, F.A., and A.B. Metzner, "Turbulence Phenomena in Drag Reducing Solutions." AIChE J., Vol. 15, N. 3 (1969) pp. 427-434.

(17) Shankar, P.N. "Laser Doppler Velocity Profile Measurements in Laminar and Turbulent Pipe Flow." Report No. 69-C-396, General Electric Research and Development Center, Schenectady, N.Y., 1969.

(18) Spangler, J.G. "Studies of Viscous Drag Reduction with Polymers Including Turbulence Measurements and Roughness Effects." Viscous Drag Reduction, C.S. Wells, ed. New York: Plenum Press, 1969.

(19) Tomita, Y. "Pipe Flows of Dilute Aqueous Polymer Solutions." Bull. of JSME, Vol. 13, N. 61 (1970), pp. 926-942.

(20) Wetzel, J.M., and F.Y. Tsai, "Impact Tube Measurements in Dilute Polymer Solutions." AIChE J., Vol. 14 (1968), p. 663.

(21) Virk, P.S., E.W. Merrill, H.S. Mickley, K.A. Smith, and E.L. Mollo-Christensen, "The Toms Phenomenon: Turbulent Pipe Flow of Dilute Polymer Solutions." J. Fluid Mech., Vol. 30, part 2 (1967), pp. 305-328.

(22) Wells, C.S., J. Harkness, and W.A. Meyer, "Turbulence Measurements in Pipe Flow of a Drag-Reducing Non-Newtonian Flow." AIAA J., Vol. 6, N. 2 (1968), pp. 250-257.

(23) Metzner, A.B., and G. Astarita, "External Flow of Viscoelastic Materials: Fluid Property Restrictions on the Use of Velocity-Sensitive Probes." AIChE J., Vol. 13 (1967), p. 550.

(24) Smith, K.A., E.W. Merrill, H.S. Mickley and P.S. Virk, "Anamalous Pitot Tube and Hot Film Measurements in Dilute Polymer Solutions." Chem. Engr. Sc., Vol. 22 (1967) p. 619.

(25) Friehe, C.A., and W.H. Schwartz, "The Use of Pitot Static Tubes and Hot-Film Anemometers in Dilute Polymer Solutions." Viscous Drag Reduction, C.S. Wells, ed., New York: Plenum Press, 1969.

(26) Donohue, G.L., D.K. McLaughlin, and W.G. Tiederman, "Turbulence Measurements with a Laser Anemometer Measuring Individual Realizations." Physics of Fluids, Vol. 15 (1972) p. 1920.

(27) Whitelaw, J.H. "Measurements in Turbulent Water Flows by Laser Anemometry." Invited Lecture, presented at the Symposium on Turbulence in Liquids, Univ. of Missouri-Rolla, 1973.

(28) McLaughlin, D.K., and W.G. Tiederman, "Statistical Biasing in Individual Realization Laser Anemometry." Physics of Fluids, (to be published).

(29) Durst, F., and J.H. Whitelaw, "Theoretical Considerations of Significance to the Design of Optical Anemometers." ASME Paper No. 72-HT-7, 1972.

(30) Hjelmfelt, A.T., and L.F. Mockros, "Motion of Discrete Particles in a Turbulent Fluid." Appl. Sci. Res., Vol. 16 (1965), pp. 149-161.

(31) Hussain, A.K.M.F., and W.C. Reynolds, "The Mechanics of a Perturbation Wave in Turbulent Shear Flow." Report No. FM-6, Thermosciences Div., Department of Mech. Engineering, Stanford Univeristy, 1970.

(32) Clark, J.A. "A Study of Incompressible Turbulent Boundary Layers in Channel Flow." Trans. of the ASME, Series D., J. of Basic Engineering, Vol. 90 (1968), pp. 455-468.

(33) Eckelmann, H., and H. Reichardt, "An Experimental Investigation in a Turbulent Channel Flow with a Thick Viscous Sublayer." Proceedings, Symposium on Turbulence in Liquids, Univ. of Missouri-Rolla, 1971.

(34) Laufer, J. "Investigation of Turbulent Flow in a Two-Dimensional Channel." NACA Report 1053, 1949.

(35) Uzkan, T., and W.C. Reynolds, "A Turbulent Boundary Layer on a Wall Moving at the Free-Stream Velocity." Report No. MD-14, Thermosciences Div., Dept of Mechanical Engineering, Stanford Univeristy, 1965.

(36) Cess, R.D. "A Survey of the Literature in Heat Transfer in Turbulent Tube Flow." Westinghouse Research Report 8-0529-R24, 1958.

(37) Tiederman, W.G., and W.C. Reynolds, "Stability of Turbulent Poiseuille Flow with Application to the Malkus Theory of Turbulence." Report No. FM-2, Thermosciences Div., Dept of Mechanical Engineering, Stanford Univ., 1965.

(38) Kays, W.M. Convective Heat and Mass Transfer. 1st ed. New York: McGraw-Hill, 1966.

(39) Van Driest, E.R. "Turbulent Drag Reduction of Polymeric Solutions." J. Hydronautics, Vol. 4, N. 3 (1970), pp. 120-126.

(40) Meyer, W.A. "A Correlation of the Frictional Characteristics for Turbulent Flow of Dilute Viscoelastic Non-Newtonian Fluids in Pipes." AIChE J., Vol. 12, N. 3 (1966), pp. 522-525.

(41) Donohue, G.L., W.G. Tiederman, and M.M. Reischman, "Flow Visualization of the Near-Wall Region in a Drag-Reducing Channel Flow." J. Fluid Mech., Vol. 56, part 3 (1972), pp. 559-575.

(42) Gupta, M.K., A.B. Metzner, and J.P. Hartnett, "Turbulent Heat-Transfer Characteristics of Viscoelastic Fluids." Int. J. Heat Mass Transfer, Vol. 10 (1967), pp. 1211-1224.

(43) Latto, B., and C.H. Shen, "Effect of Dilute Polymer Solution Injection on External Boundary Layer Phenomena." Can. Jour. of Chem. Engr., Vol. 48 (1970), pp. 34-38.

(44) Donohue, G.L. and W.G. Tiederman, "The Effect of a Dilute, Drag-Reducing Macro-Molecular Solution in the Viscous Sublayer of a Turbulent Channel Flow." (a 16 mm motion picture), ASME/ESL Film Library, New York, 1971.

(45) Kline, S.J., W.C. Reynolds, F.A. Schraub, and P.W. Rundstadler, "The Structure of Turbulent Boundary Layers." J. Fluid Mech., Vol. 30 (1967), p. 741.

(46) Kim, H.T., S.J. Kline, and W.C. Reynolds, "An Experimental Study of Turbulence Production Near a Smooth Wall in a Boundary Layer with Zero Pressure Gradient." Report No. MD-20, Thermosciences Div., Dept. of Mech. Engineering, Stanford Univ., 1968.

(47) Barry, B.A. Engineering Measurements. 1st ed. New York, John Wiley & Sons, 1964.

(48) Whitsitt, N.F., L.J. Harrington, and H.R. Crawford, "Effect of Wall Shear Stress in Drag Reduction of Viscoelastic Solutions." Viscous Drag Reduction, C.S. Wells, ed., New York: Plenum Press, 1969.

APPENDIX A

UNCERTAINTY ESTIMATES AND DATA TABULATION

The desire to provide accurate velocity measurements in drag-reducing flows prompted a complete examination of the uncertainties. The sources of error which may be considered significant are the 1) probe volume location, y, 2) kinematic viscosity, υ, 3) mean velocity, $\overline{U}$, and 4) turbulent intensities, u'. The errors in the last two quantities are largely random and are calculated based on a 95% level of confidence for each sample set. The calculations were performed using "student t" and "chi-squared" distributions.

The confidence intervals of 95% in the value of $\overline{U}$ are larger than the errors induced by systematic experimental inaccuracies, which are estimated to be 1%. The 95% confidence intervals for all of the mean velocity and the turbulent intensity measurements are shown in Table XII.

It should be recalled that the estimated accuracy in locating the probe volume position is y ± 0.0005 inches. The error in kinematic viscosity measurement at high shear rates (the Fann viscometer) was approximately 10%. The estimated error in the viscosity measurement using the Brookfield viscometer is 3%. Thus, when moderate shear rates ($< 100\ sec^{-1}$) are present the accuracy of the kinematic viscosity changes from 10% to 3%.

The basic error sources and the amount of error present has now been identified and enumerated, and an uncertainty analysis follows.

TABLE XII

VELOCITY DATA TABULATION

Run Designation	y^+	U^+	N	$\overline{U}$ % Error	u' % Error	y % Error	y^+ % Error	U^+ % Error
SOL-14	5.9	6.6	232	4.2	9.3	4.8	7.6	6.5
	9.2	8.7	332	3.4	7.7	3.0	6.6	6.0
(Re=17,700)	18.0	11.5	380	2.1	7.3	1.5	6.0	5.4
	35.9	13.6	289	1.9	8.3	0.7	5.9	5.3
	67.2	15.1	222	1.5	9.4	0.4	5.8	5.2
	140.0	17.1	75	1.9	16.2	0.2	5.8	5.3
	286.0	18.2	50	1.6	16.7	0.0	5.8	5.2
SOL-15	2.7	3.7	173	7.5	10.7	10.6	12.1	9.0
	6.1	6.2	223	4.7	9.4	4.8	7.6	6.9
(Re=18,500)	9.6	8.4	179	4.8	10.4	3.0	6.6	6.9
	258.0	18.5	52	1.2	19.3	0.0	5.8	5.1
SOL-12	7.8	7.1	314	5.8	8.0	4.7	7.5	7.7
	13.6	10.2	300	4.0	8.1	2.7	6.4	6.4
(Re=24,700)	19.4	11.9	260	3.5	8.7	1.9	6.1	6.1
	37.1	13.9	169	3.2	10.8	0.9	5.9	5.9
	108.0	16.4	103	2.6	13.8	0.3	5.8	5.6
	223.0	18.5	72	1.8	16.5	0.2	5.8	5.3
	377.0	19.5	90	1.1	14.8	0.0	5.8	5.1
SOL-13	4.4	3.8	276	2.7	8.5	16.7	17.7	5.7
	6.6	6.8	458	2.6	6.6	10.9	12.4	5.6
(Re=55,200)	9.2	8.6	1001	1.8	4.5	7.8	9.7	5.6

TABLE XII (Continued)

SOL-13	17.9	11.7	1028	1.2	4.4	4.1	7.1	5.3
	35.4	14.2	1014	0.9	4.5	2.1	6.2	5.2
(Re=55,200)	179.0	17.3	224	1.3	9.4	0.4	5.8	5.2
	361.0	19.8	159	1.0	11.2	0.2	5.8	5.1
	778.0	20.9	179	0.6	10.5	0.0	5.8	5.1
DPS- 5	3.2	3.6	188	4.1	10.2	4.8	12.6	7.3
	6.1	6.2	219	3.1	8.5	2.5	11.9	6.8
(Re=20,200)	8.9	8.2	202	3.4	9.9	1.7	11.8	6.9
	13.1	10.2	215	3.0	9.6	1.1	6.8	6.7
	17.3	12.0	117	4.0	13.0	0.8	6.8	7.2
	33.8	17.8	156	2.9	10.3	0.4	6.7	6.7
	67.8	22.1	70	3.1	16.7	0.2	6.7	6.8
	134.0	24.5	69	1.7	16.7	0.0	6.7	6.2
DPS- 6	3.6	4.4	157	4.6	11.3	5.9	13.1	7.6
	6.7	6.7	181	3.4	10.5	3.0	12.0	6.9
(Re=26,400)	9.5	9.3	141	3.9	11.8	2.1	11.8	7.2
	17.8	13.5	193	3.0	10.1	1.0	11.7	6.7
	23.7	15.6	132	3.3	12.2	0.7	11.7	6.8
	36.6	19.1	73	3.6	16.4	0.5	6.7	7.0
	52.9	22.6	53	3.8	19.1	0.3	6.7	7.1
	102.0	24.6	47	2.8	20.2	0.2	6.7	6.6
	169.0	25.6	51	1.3	19.5	0.0	6.7	6.1

TABLE XII (Continued)

DPS- 7	4.6	5.3	302	2.5	8.1	5.9	13.1	6.5
	8.5	8.1	1001	1.1	1.4	3.0	12.0	6.1
(Re=44,500)	12.5	10.6	311	2.5	8.0	2.1	11.8	6.5
	19.8	14.9	236	2.3	9.1	1.2	11.7	6.4
	30.8	18.1	155	2.6	11.3	0.7	11.7	6.5
	44.7	21.6	106	2.8	13.6	0.5	6.7	6.6
	73.8	24.5	61	3.0	17.8	0.3	6.7	6.7
	136.0	26.8	64	2.2	17.5	0.2	6.7	6.4
	229.0	27.2	61	1.1	17.8	0.0	6.7	6.1
DPS- 9	8.4	8.4	816	1.2	1.6	5.9	13.1	6.1
	11.8	11.0	1019	1.2	1.4	4.0	12.3	6.1
(Re=52,400)	19.0	14.7	951	1.0	1.5	2.5	11.9	6.1
	29.4	18.3	223	2.2	9.4	1.5	11.8	6.4
	49.0	21.2	123	2.3	12.6	0.9	11.7	6.4
	75.4	23.0	109	1.8	13.4	0.6	6.7	6.3
	144.0	24.6	59	1.7	18.1	0.3	6.7	6.2
	268.0	25.5	67	1.1	17.1	0.2	6.7	6.1
	453.0	26.2	13	1.9	38.0	0.0	6.7	6.3
DPS-10	3.9	4.4	278	4.0	8.4	4.8	12.6	7.2
	7.5	7.4	294	3.0	8.2	2.5	11.9	6.7
(Re=20,600)	10.9	9.7	326	2.8	7.8	1.7	11.8	6.6
	14.3	11.3	285	2.8	8.3	1.2	11.7	6.6
	21.2	13.9	181	3.0	10.4	0.8	6.8	6.7
	36.0	17.0	131	2.4	12.2	0.5	6.7	6.5
	71.2	19.7	75	2.4	16.1	0.2	6.7	6.5
	106.0	21.4	75	1.6	16.1	0.2	6.7	6.2
	180.0	21.7	81	1.0	15.5	0.0	6.7	6.1

TABLE XII (Continued)

DPS-11	4.5	5.4	265	3.7	8.7	7.6	13.9	7.0
	8.3	8.3	256	2.8	8.8	3.7	12.2	6.7
(Re=37,500)	11.1	9.8	252	2.9	8.9	2.7	12.0	6.7
	17.0	12.5	246	2.8	9.0	1.8	11.8	6.7
	23.8	14.3	195	3.1	10.1	1.2	11.7	6.8
	45.8	19.7	104	3.2	13.7	0.6	11.7	6.8
	83.9	23.3	64	2.2	17.5	0.3	6.7	6.4
	171.0	24.9	57	1.5	18.5	0.2	6.7	6.2
	289.0	25.2	69	1.1	16.9	0.0	6.7	6.1
DPS-12	5.2	5.7	197	4.1	10.0	7.6	13.9	7.3
	8.3	8.3	195	3.1	10.1	4.4	12.5	6.8
(Re=46,00)	12.2	10.4	139	3.1	11.9	2.9	12.0	6.8
	18.2	13.1	138	3.3	11.9	1.9	18.8	6.8
	30.4	17.5	125	3.1	12.6	1.1	17.7	6.8
	50.5	21.4	89	2.9	14.3	0.6	17.7	6.7
	105.0	25.3	46	2.3	20.4	0.3	6.7	6.4
	196.0	26.6	50	1.1	19.6	0.2	6.7	6.1
	332.0	26.4	50	1.2	19.6	0.0	6.7	6.1

The calculation of u_τ, U^+, y^+, $\overline{U}_{AVG}$, $u'/\overline{U}$ and $u_\tau/\overline{U}_{AVG}$ is dependent upon experimental quantities and errors in these derived quantities was calculated using the methods outlined in Barry (47).

The errors in u_τ, $\overline{U}_{AVG}$, $u_\tau/\overline{U}_{AVG}$ are constant for each flow and they do not very significantly from flow to flow. The wall shear velocity is computed from

$$u_\tau = \left[\frac{\upsilon \, d\overline{U}}{dy}\right]^{\frac{1}{2}} \qquad \text{(A-1)}$$

Only near-wall data is used to determine u_τ and in this region the errors are large. In general, the errors prevalent in the computation are $\upsilon \pm 10\%$, $y \pm 5\%$ and $\overline{U} \pm 5\%$. The resulting error in u_τ is

$$u_\tau \pm 6\%$$

The mass-average velocity is determined by a velocity profile integration and is accurate to within

$$\overline{U}_{AVG} \pm 4\%$$

Thus, the error in $u_\tau/\overline{U}_{AVG}$ is

$$u_\tau/\overline{U}_{AVG} \pm 7\%$$

The non-dimensional coordinates U^+ and y^+ have errors that are a function of the local uncertainties. That is, for drag-reducing flows

$$y^+ = (u_\tau \pm 6\%)\,\frac{Y}{\upsilon} \qquad \text{(A-2)}$$

and

$$U^+ = \overline{U}/(u_\tau \pm 6\%) \qquad \text{(A-3)}$$

The errors in $\overline{U}$, ν and y were discussed earlier and the resultant error in y^+ and U^+ calculated from Equations A-2 and A-3 are shown in Table XII. The value of u_τ for the solvent flows obtained by "fitting" the data to the universal velocity profile. The uncertainty present in this type of fitting procedure is estimated at 5%.

The uncertainty in the turbulent intensities, u', is a function of the sample size from which u' was calculated and must be determined for each data point measured. These values are also shown in Table XII. The expected uncertainty of the ratios u'/u_τ and $u'/\overline{U}$ can be calculated at each measuring location. Excluding a single data point the error in u'/u_τ has a maximum of 21% and a minimum of 9%. The bulk of the measurements are on the order of

$$\left[u'/u_\tau\right] \pm 12\%.$$

The error in the ratio $u'/\overline{U}$ may also be calculated from Table XII. The range of error is found to be from 7% to 20%, with the bulk of the measurements being accurate to

$$\left[u'/\overline{U}\right] \pm 10\%.$$

APPENDIX B

DRAG-REDUCTION RESULTS

This Appendix presents the results of the pressure drop-flow rate tests performed on the drag-reducing polymer solutions. These measurements were made in an effort to obtain independent verification of the drag-reducing properties of the dilute polymer solutions. In addition, the results give an indication of the consistancy with which the polymer solutions were mixed.

Since the pressure drop in the two-dimensional channel was too small to be measured accurately, two nine-foot stainless steel pipes (0.835 and 0.425 inches diameter) that operate from a blowdown reservoir were used. The solutions were removed from the piping upstream of the entrance channel and, thus, the solutions were the same undegraded solutions used for the velocity measurements. Two pipes were used in an effort to give a broad range of data.

The amount of friction reduction was calculated by measuring the pressure drop in the pipes for a flow with and without the polymer additives. Percent drag-reduction can be found from

$$\% \text{ DR} = \left[\frac{[\Delta P]_{SOL} - [\Delta P]_{DPS}}{[\Delta P]_{SOL}}\right] \times 100 \qquad \text{(B-1)}$$

Here the pressure drop comparison is made at the same flow rate. The polymer solution characterization data for the three mixes of Separan

AP273 and the three mixes of Magnifloc 837-A, and the single mix of Polyox WSR-301, are shown in Figures 51, 52 and 53 respectively. There are two important items to note. First, the data scatter appear very wide, but consulting the data for a specific run indicates that the scatter is relatively small for each run.

Secondly, the slight but consistant effect of pipe diameter should be noted. There are effectively three diameters represented here: a 0.835 inch pipe, a 0.425 inch pipe and a 1.956 inch (hydraulic diameter) channel. The amount of drag-reduction in the channel was determined by first obtaining the solvent wall shear velocity, $[u_\tau]_{SOL}$ from a velocity profile integration and use of Figure 21. The percent drag-reduction was then obtained from

$$\% \text{ DR} = \left[\frac{[u_\tau]^2_{SOL} - [u_\tau]^2_{DPS}}{[u_\tau]^2_{SOL}}\right] \times 100 \qquad \text{(B-2)}$$

The pipe diameter effect appears greater at lower shearing stresses for each pipe, and the slope of the drag-reduction curve appears to lessen for increasing flow diameters. Thus the shear rate independence of drag-reduction as put forth by Whitsitt (48) was not assumed, and the pipe pressure drop results are to be used for verification and consistancy tests alone.

APPENDIX C

FIGURES AND ILLUSTRATIONS

This Appendix contains the Figures and Illustrations referred to in the text of this thesis.

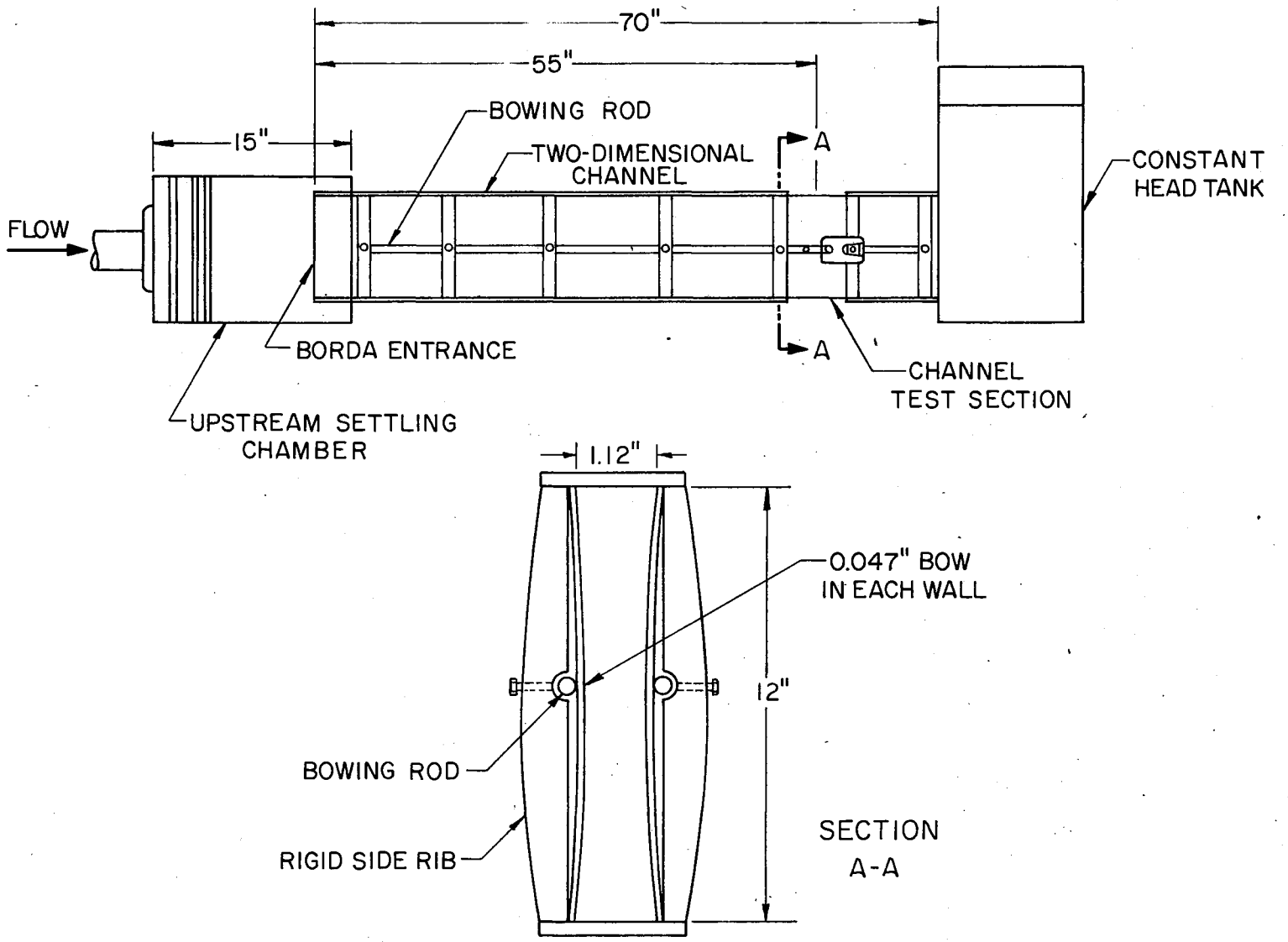

Figure 1. Schematic of Two-Dimensional Channel with Bowed Walls

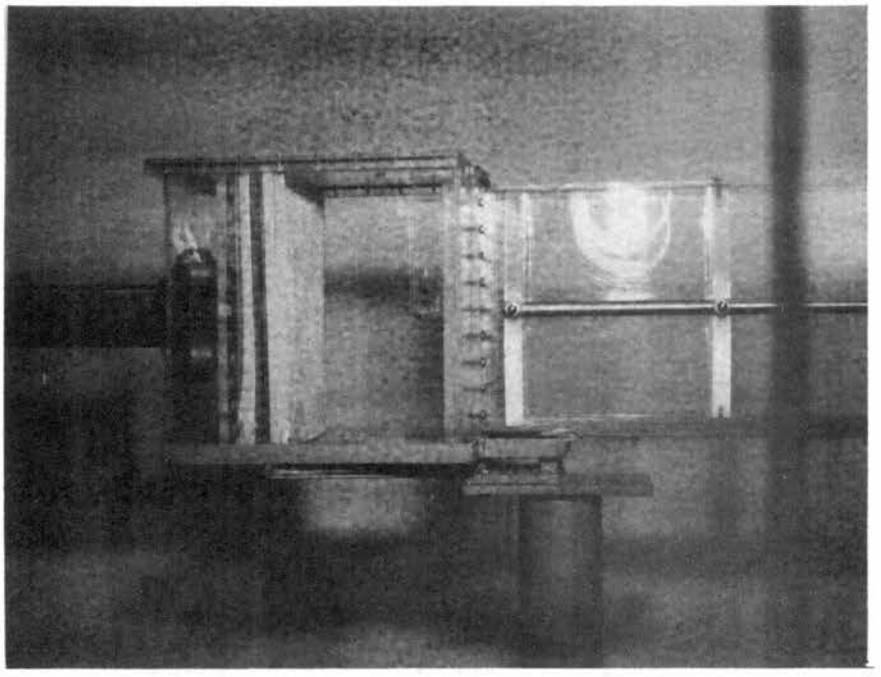

Figure 2. Upstream Settling Chamber of the Turbulent Flow Channel

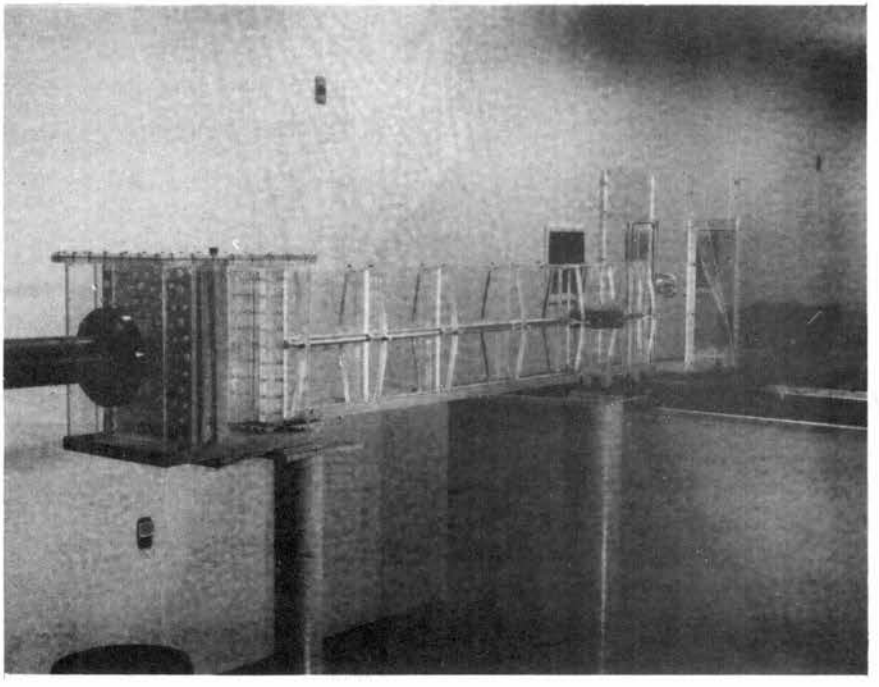

Figure 3. Turbulent Flow Channel - Overview

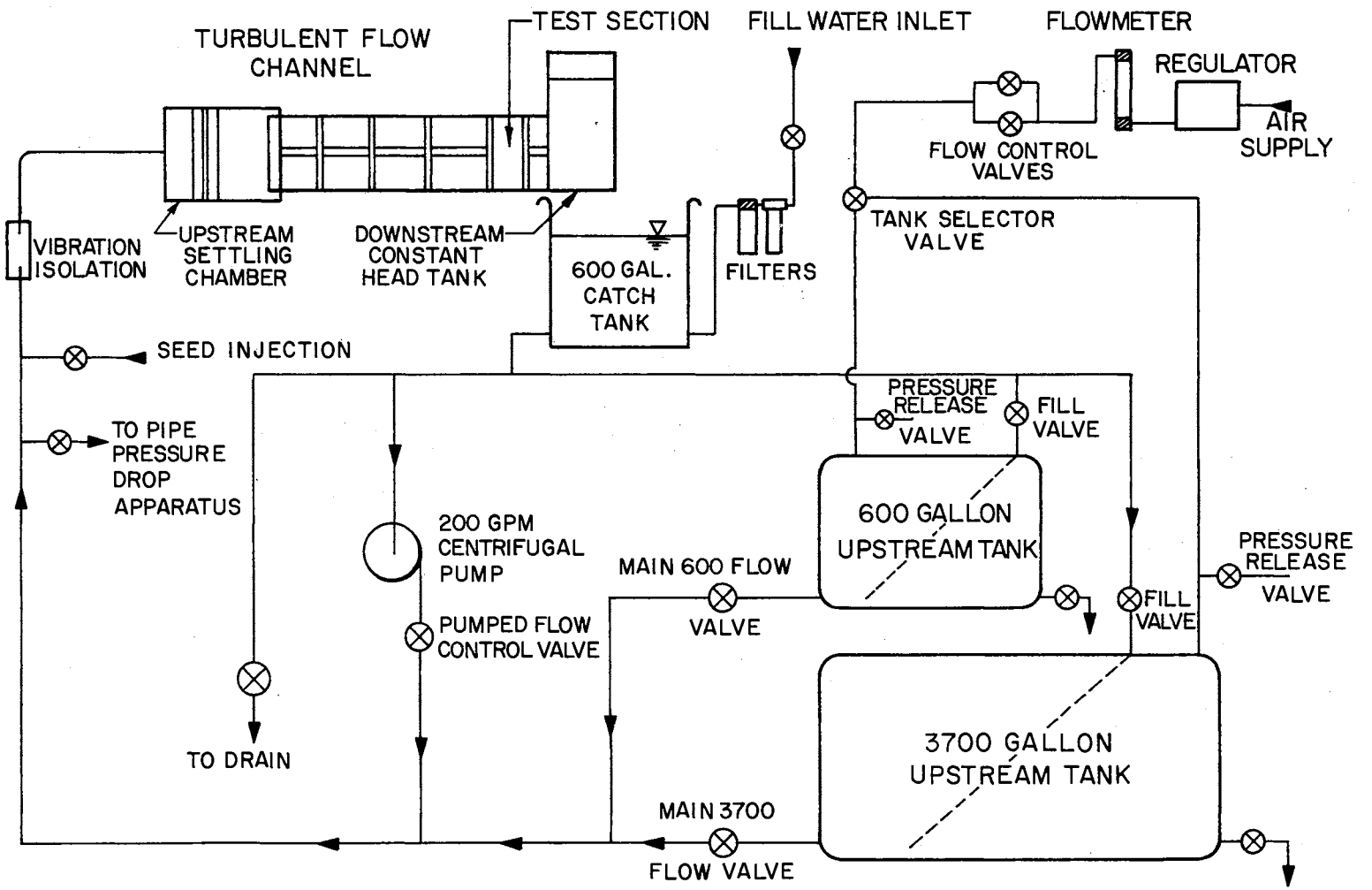

Figure 4. Schematic of Flow Channel and Circulation System

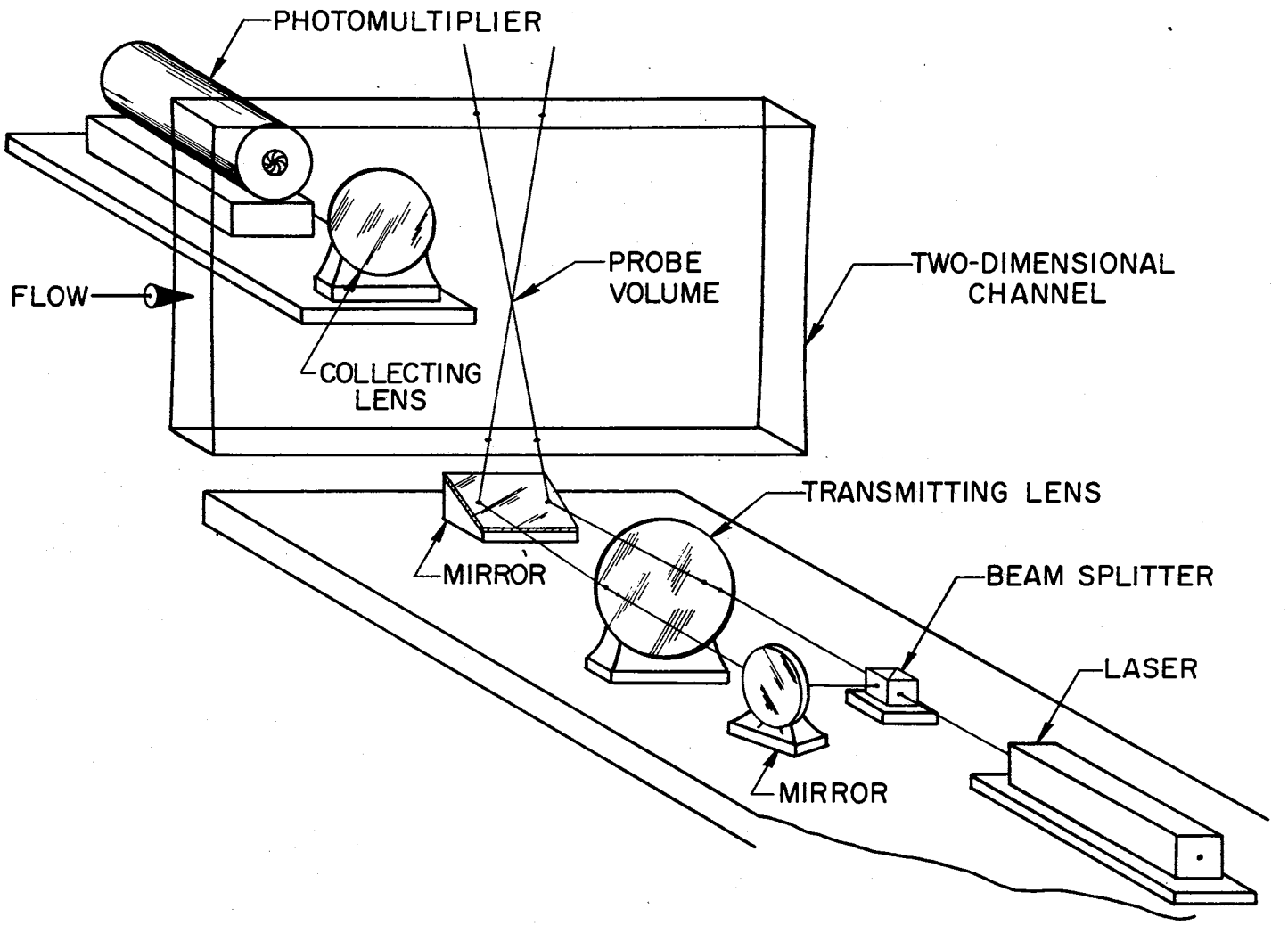

Figure 5. Side-Scatter Laser Anemometer Measuring Individual Realizations (LAMIR)

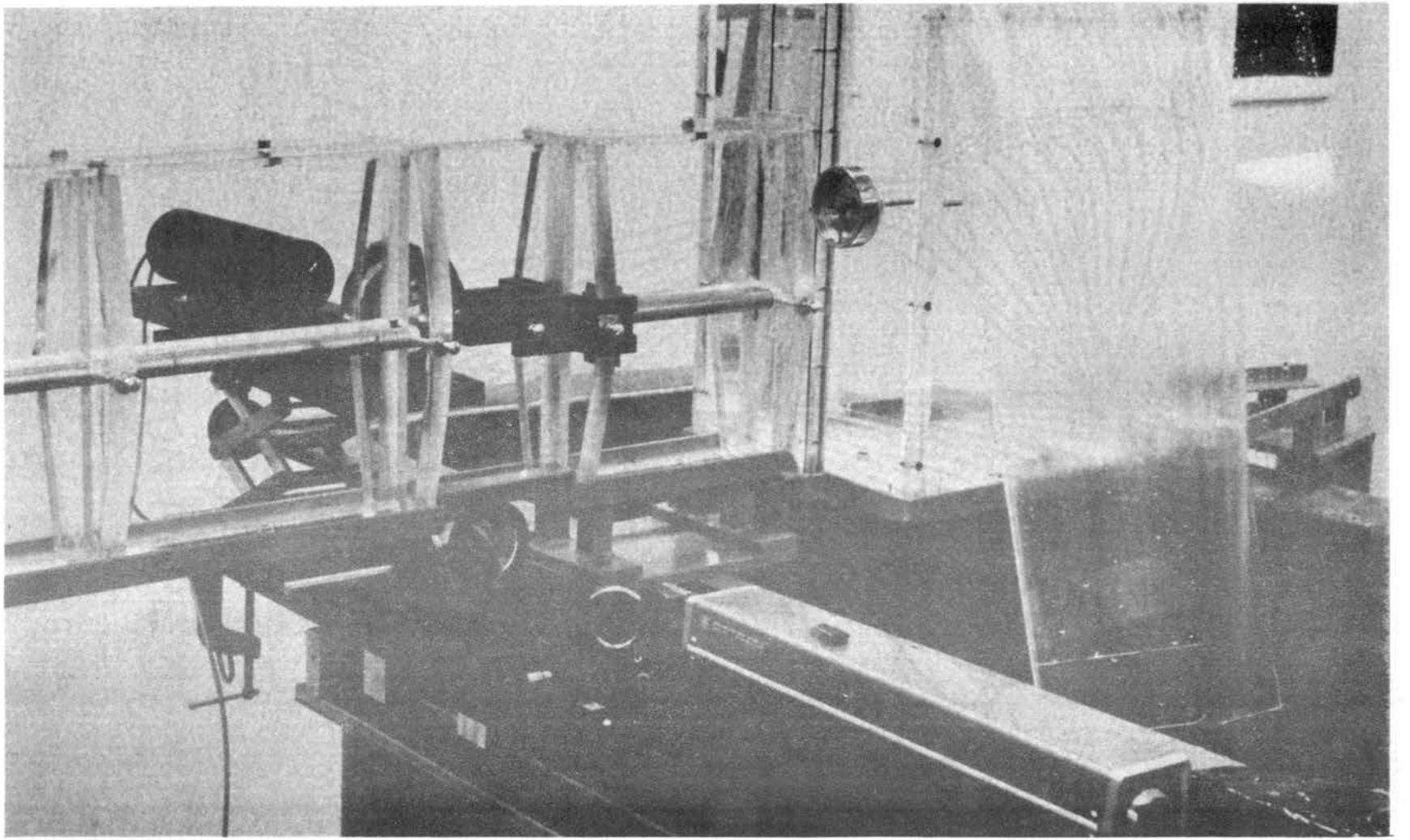

Figure 6. Photograph of LAMIR and Turbulent Flow Channel

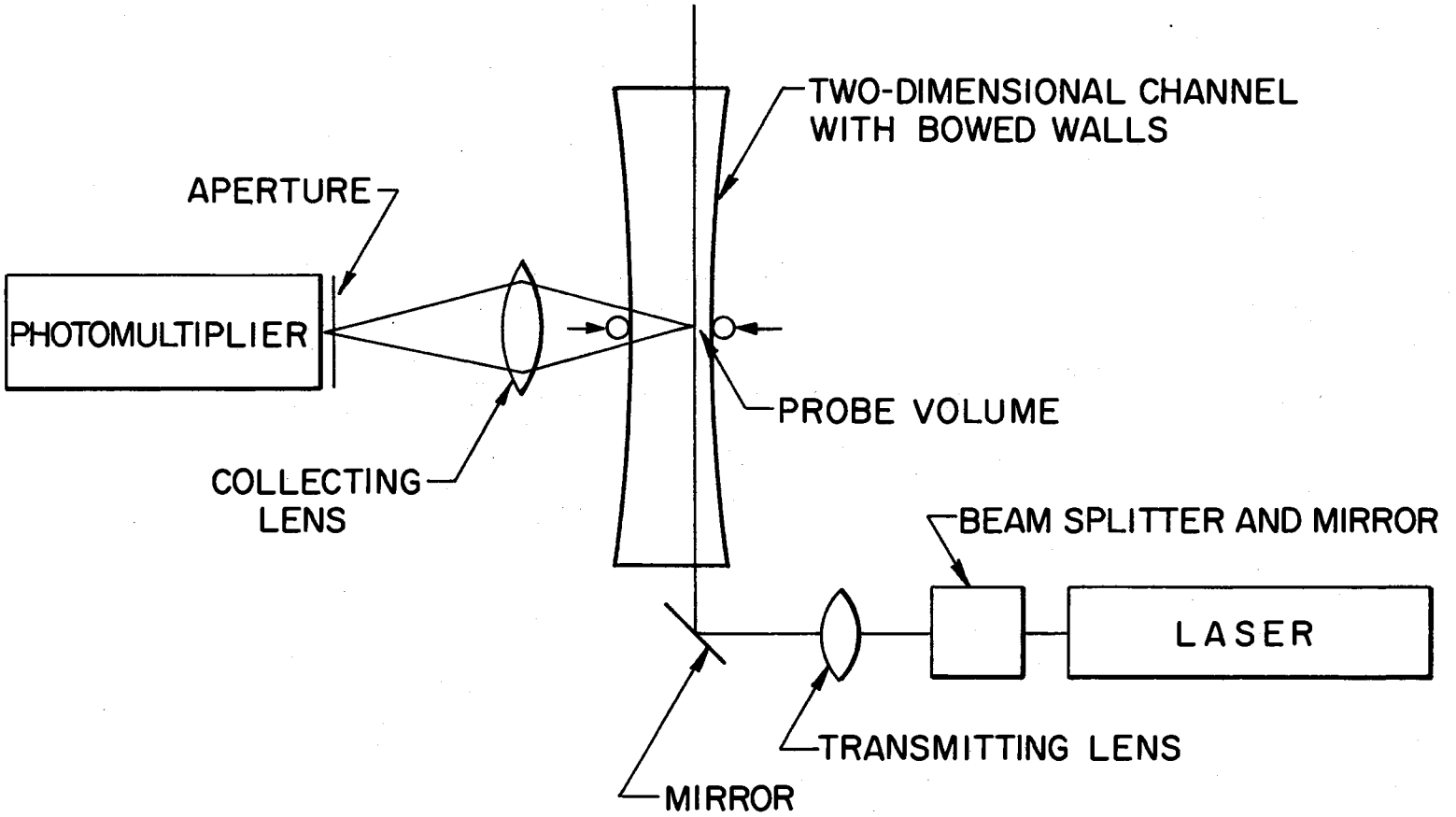

Figure 7. Schematic of Flow Channel and Optical Components

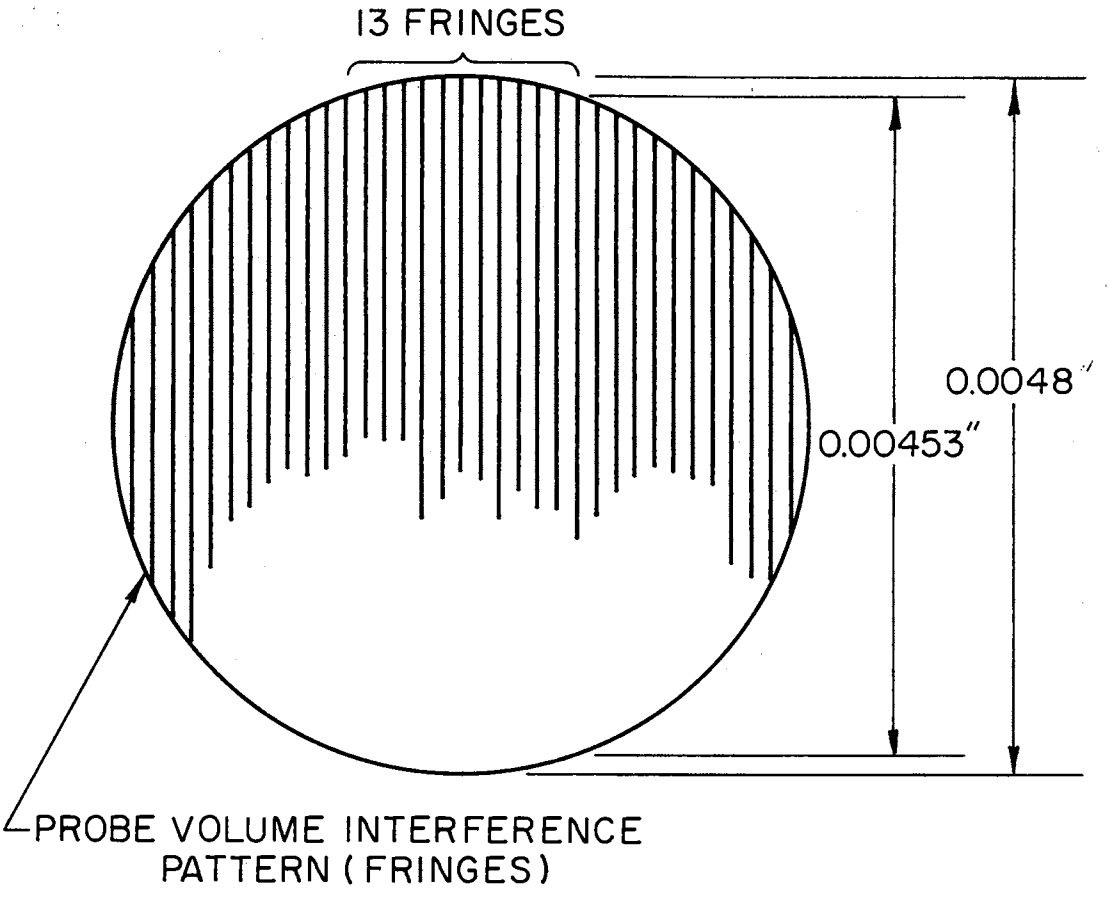

Figure 8. Cross Section of Probe Volume

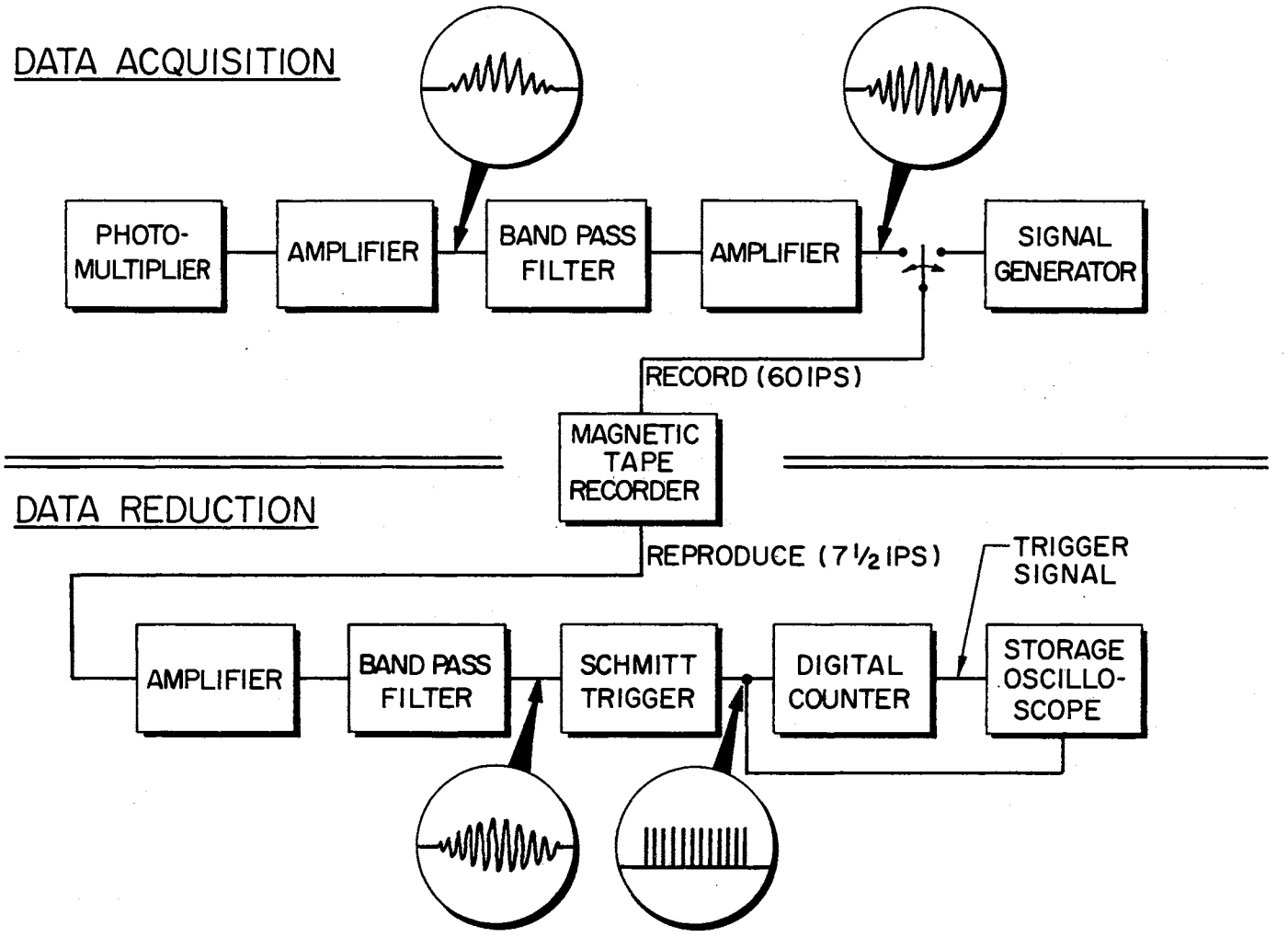

Figure 9. Block Diagram of Data Acquisition and Reduction System

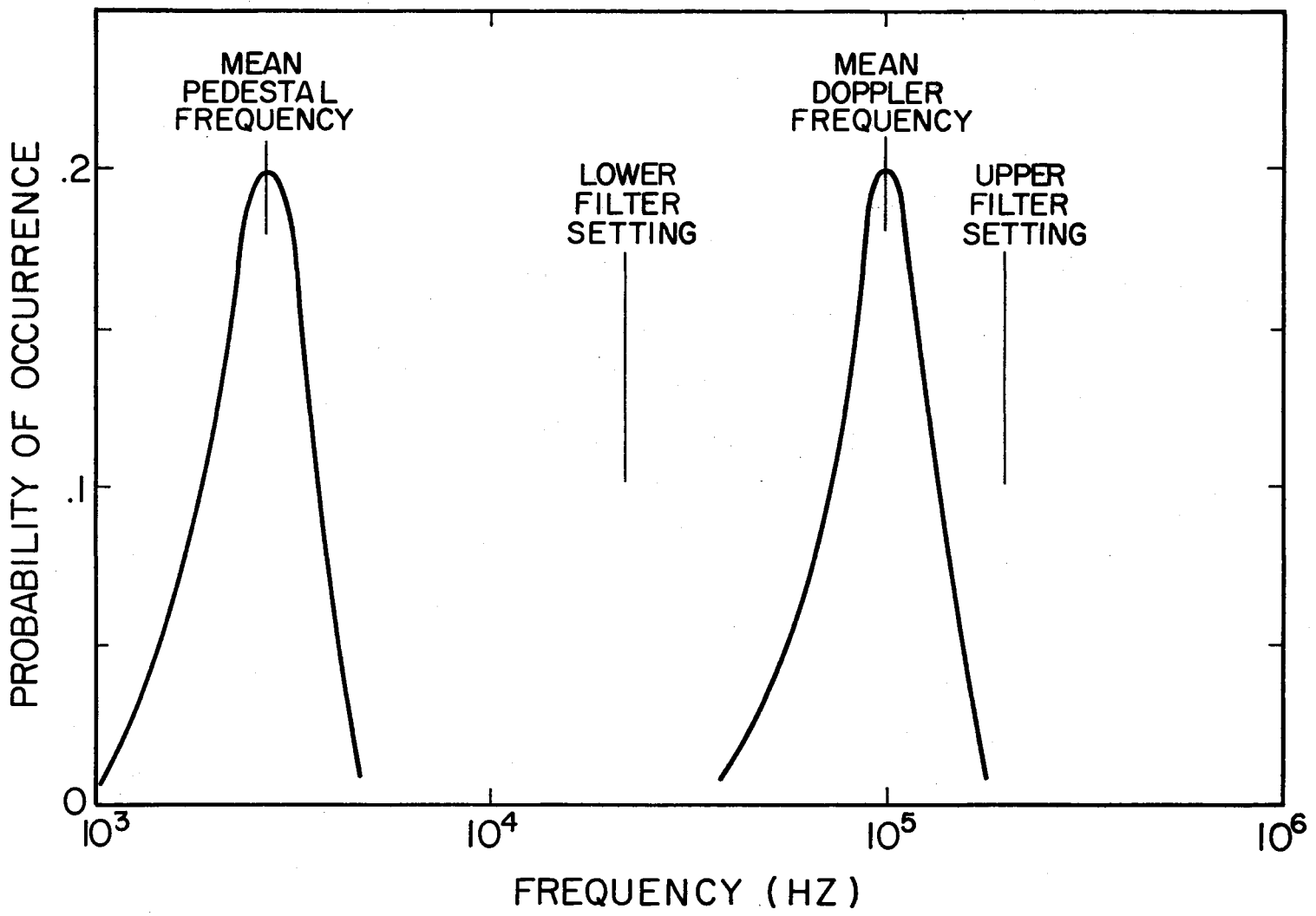

Figure 10. Histograms of Doppler and Pedestal Frequencies

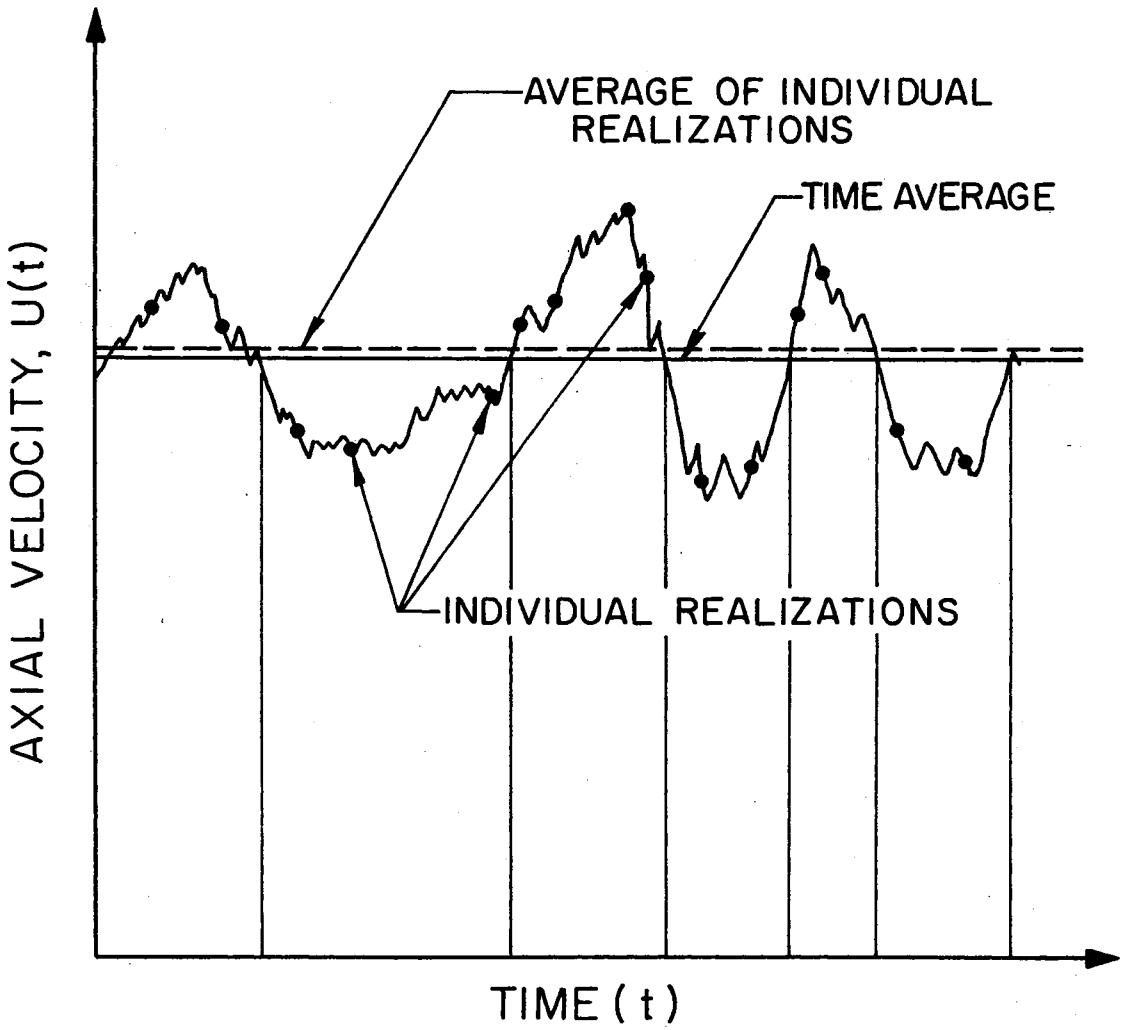

Figure 11. Comparison of Time-Average and Individual Realization Mean Velocities for Turbulent Flow

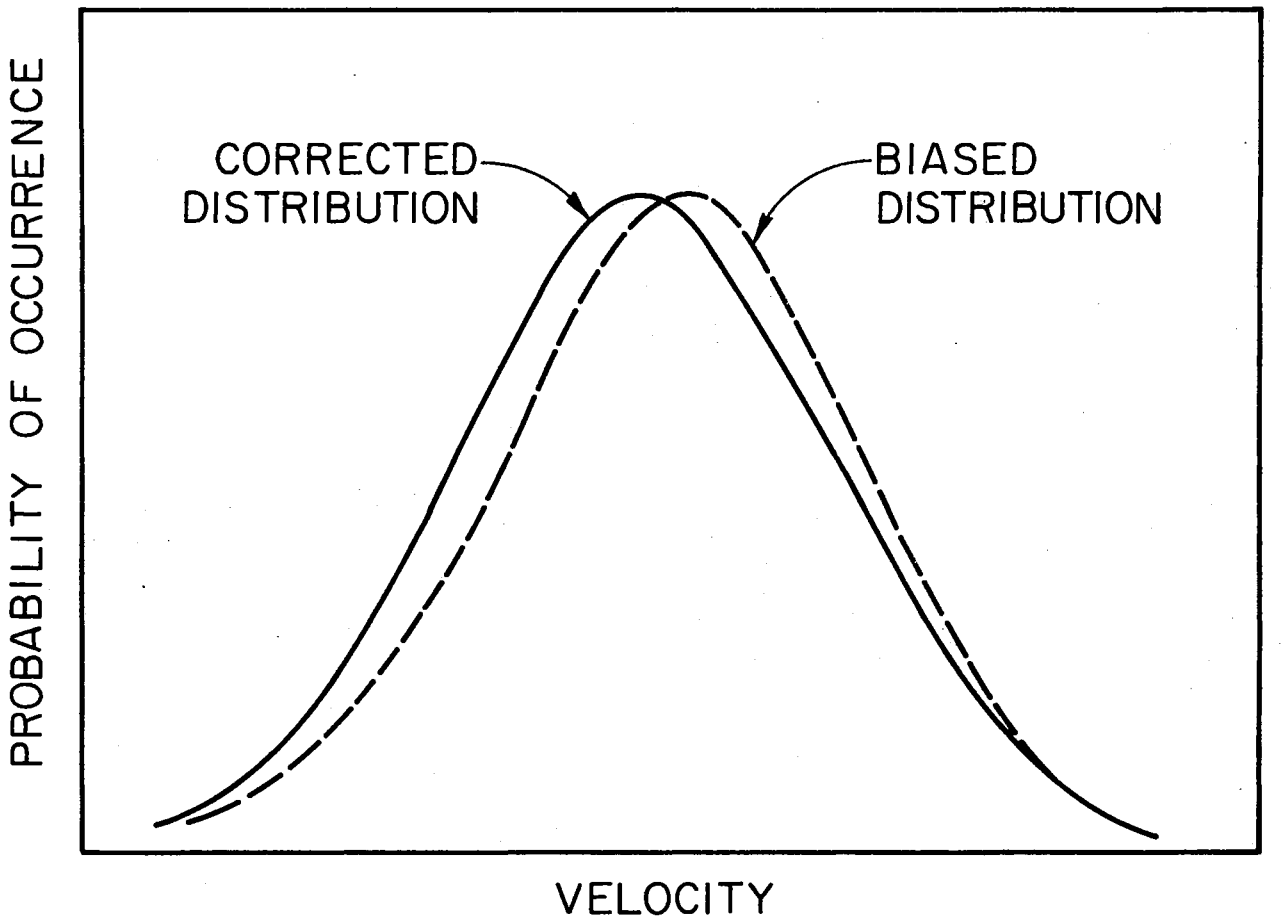

Figure 12. Comparison of Biased and Corrected Velocity Histograms

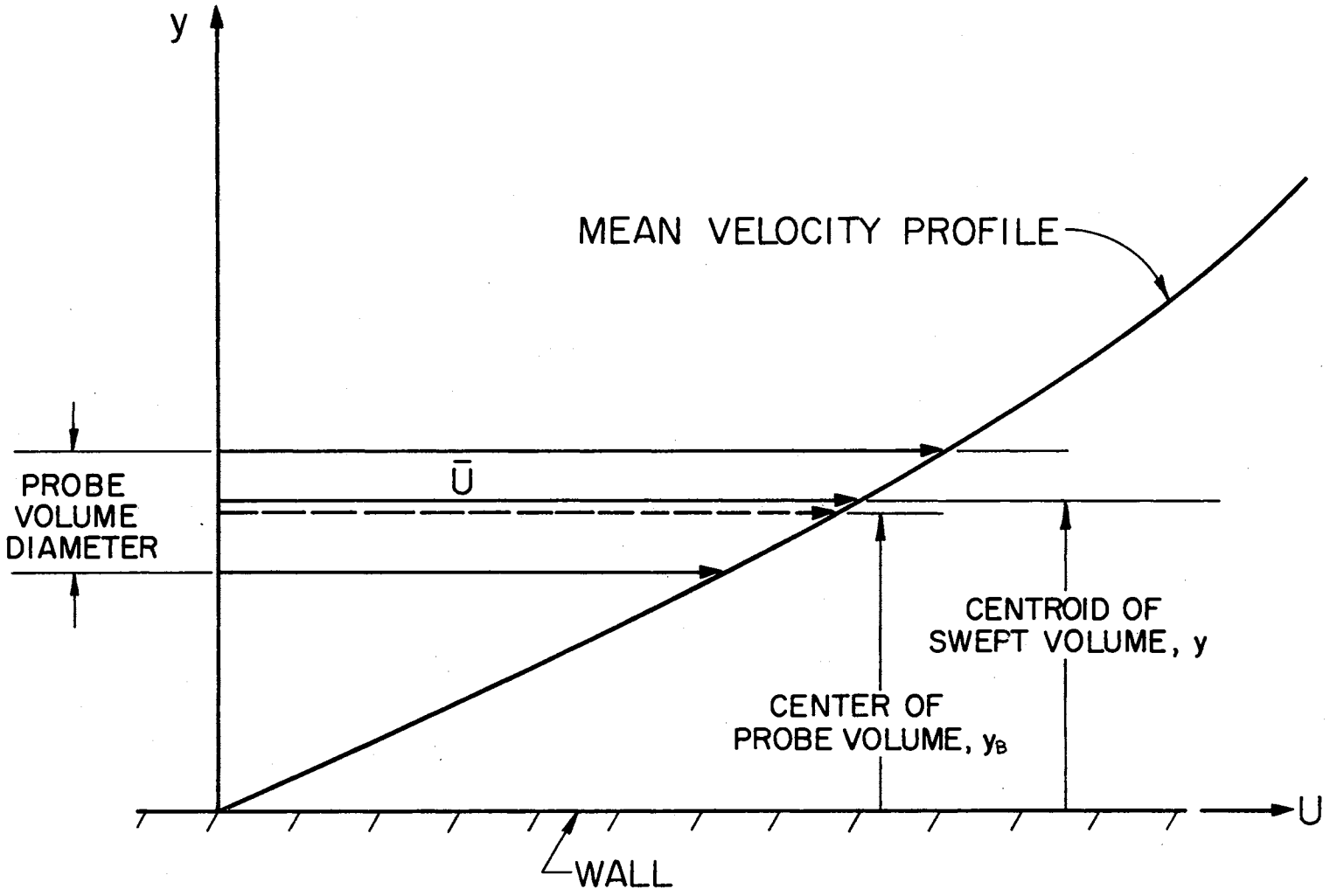

Figure 13. Illustration of Velocity Gradient Correction

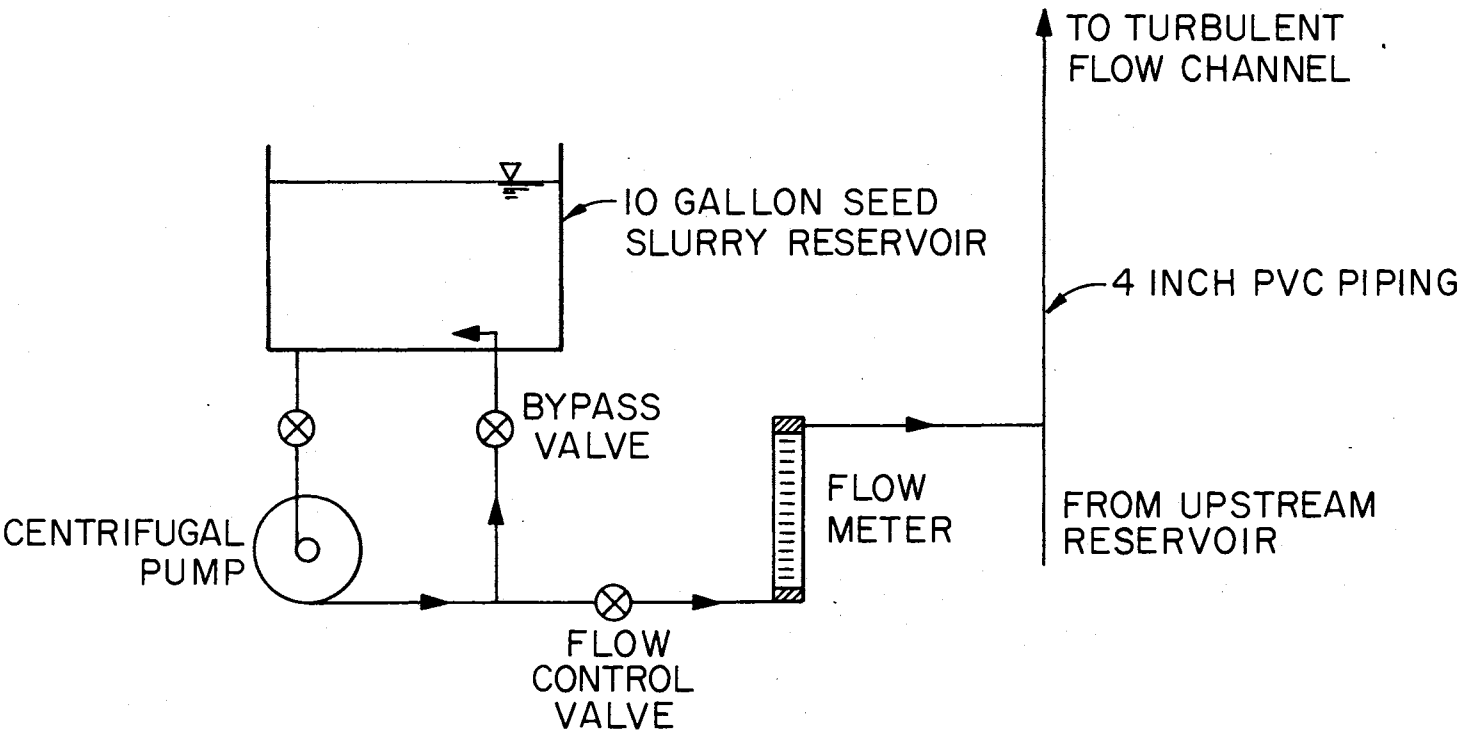

Figure 14. Line Diagram of Seed Injection System

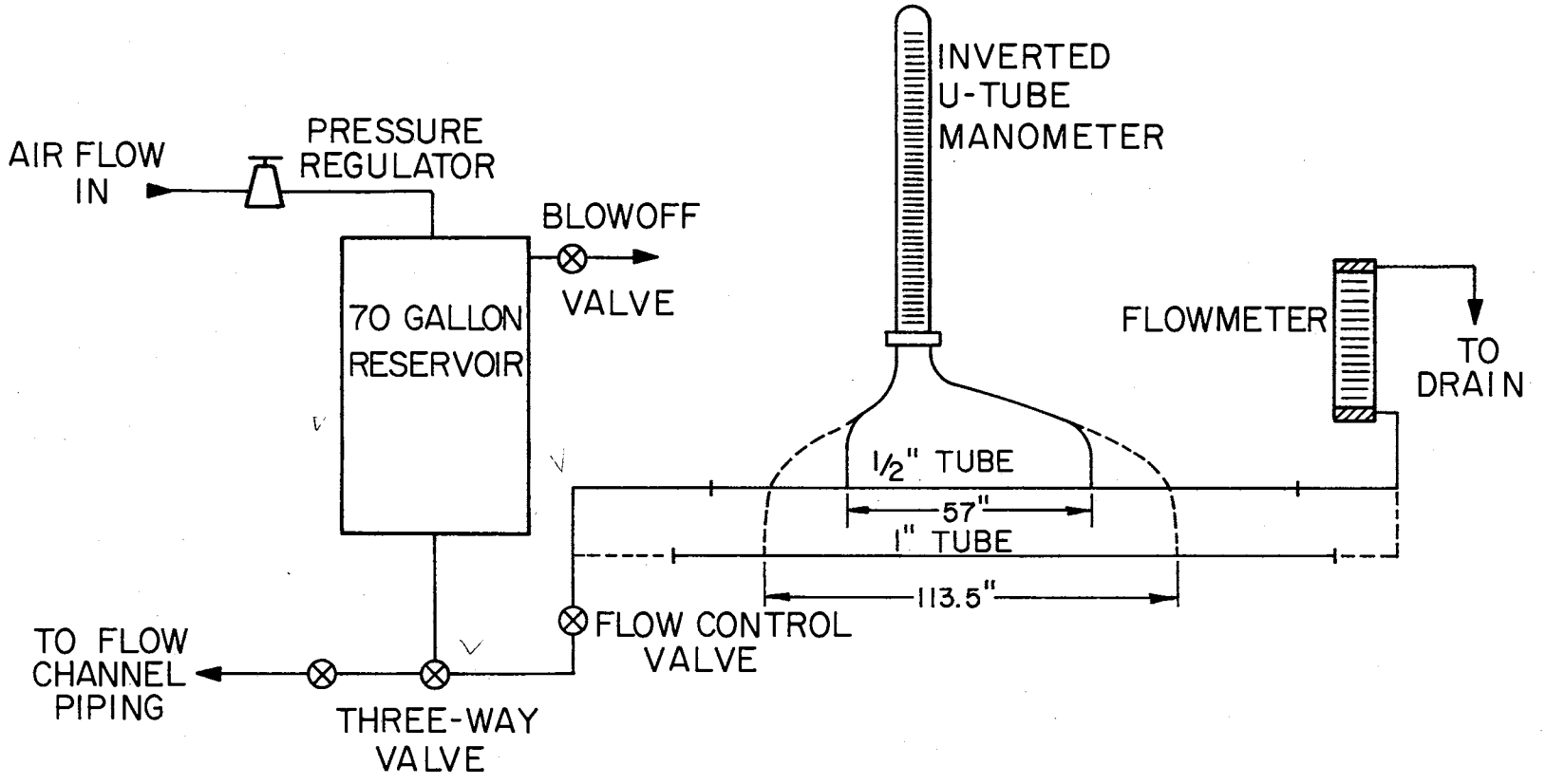

Figure 15. Line Diagram of Pipe Pressure Drop Apparatus

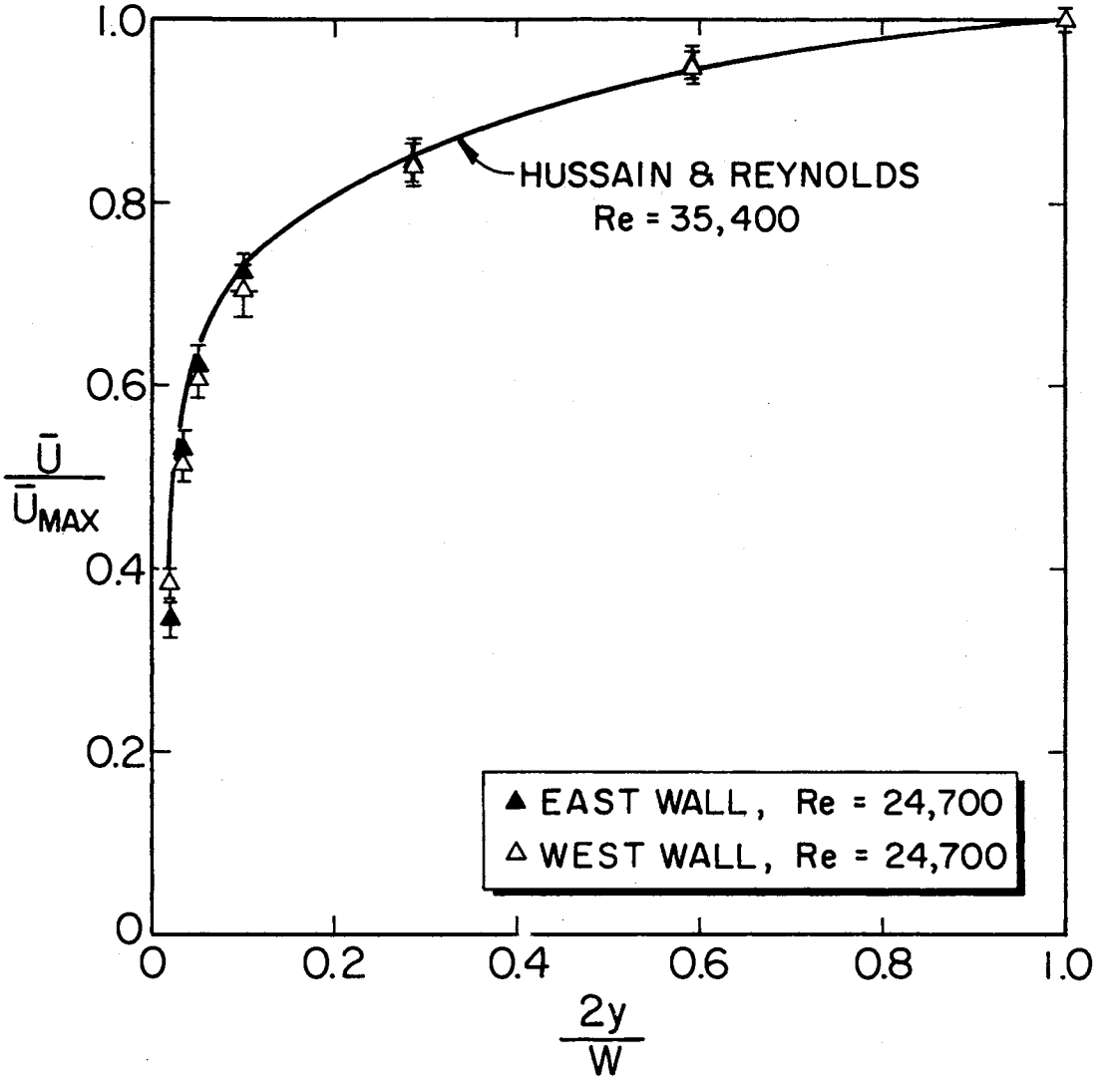

Figure 16. Symmetry Properties of Turbulent Flow Channel

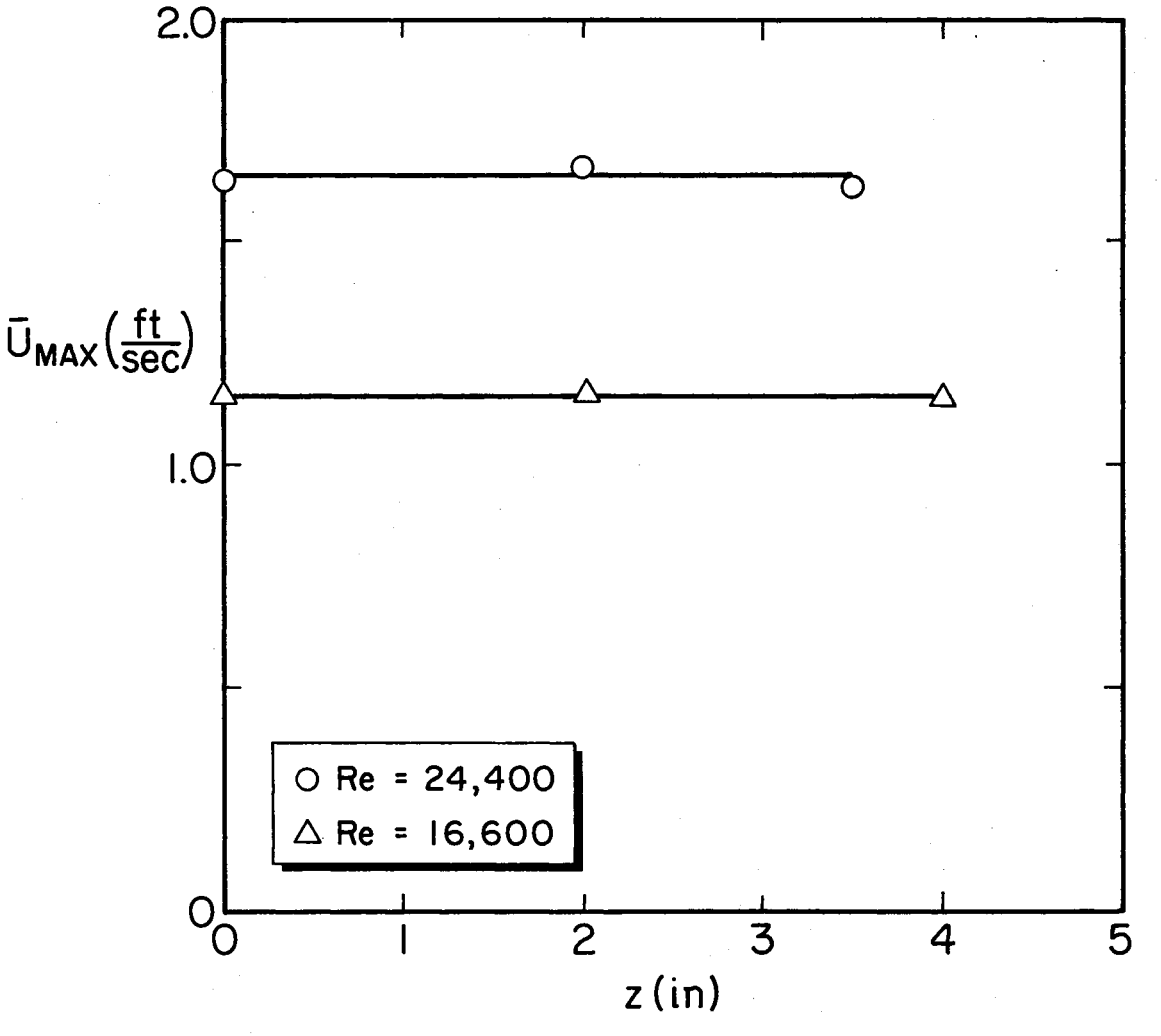

Figure 17. Two-Dimensional Properties of Turbulent Flow Channel

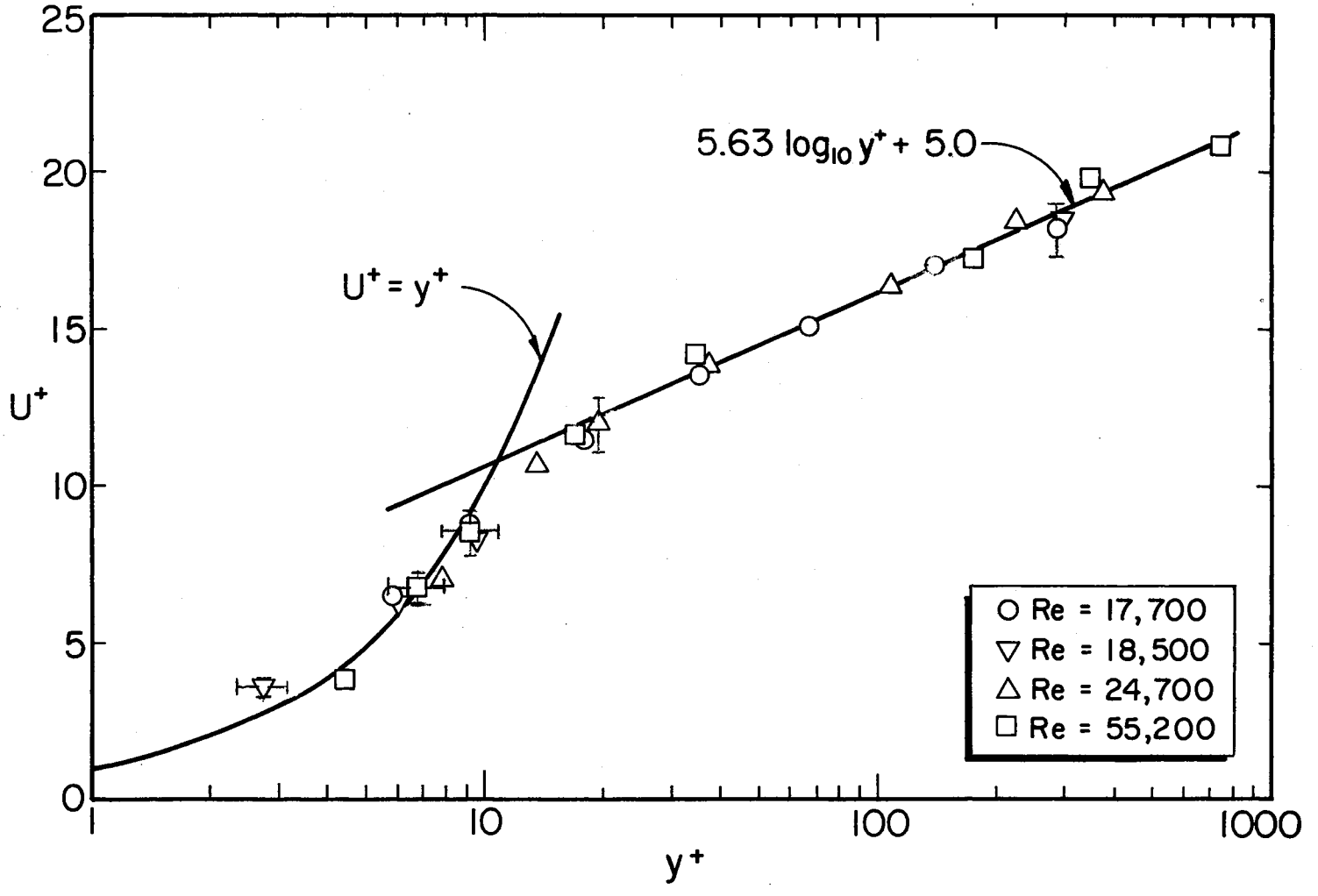

Figure 18. Law of the Wall Mean Velocity Profiles

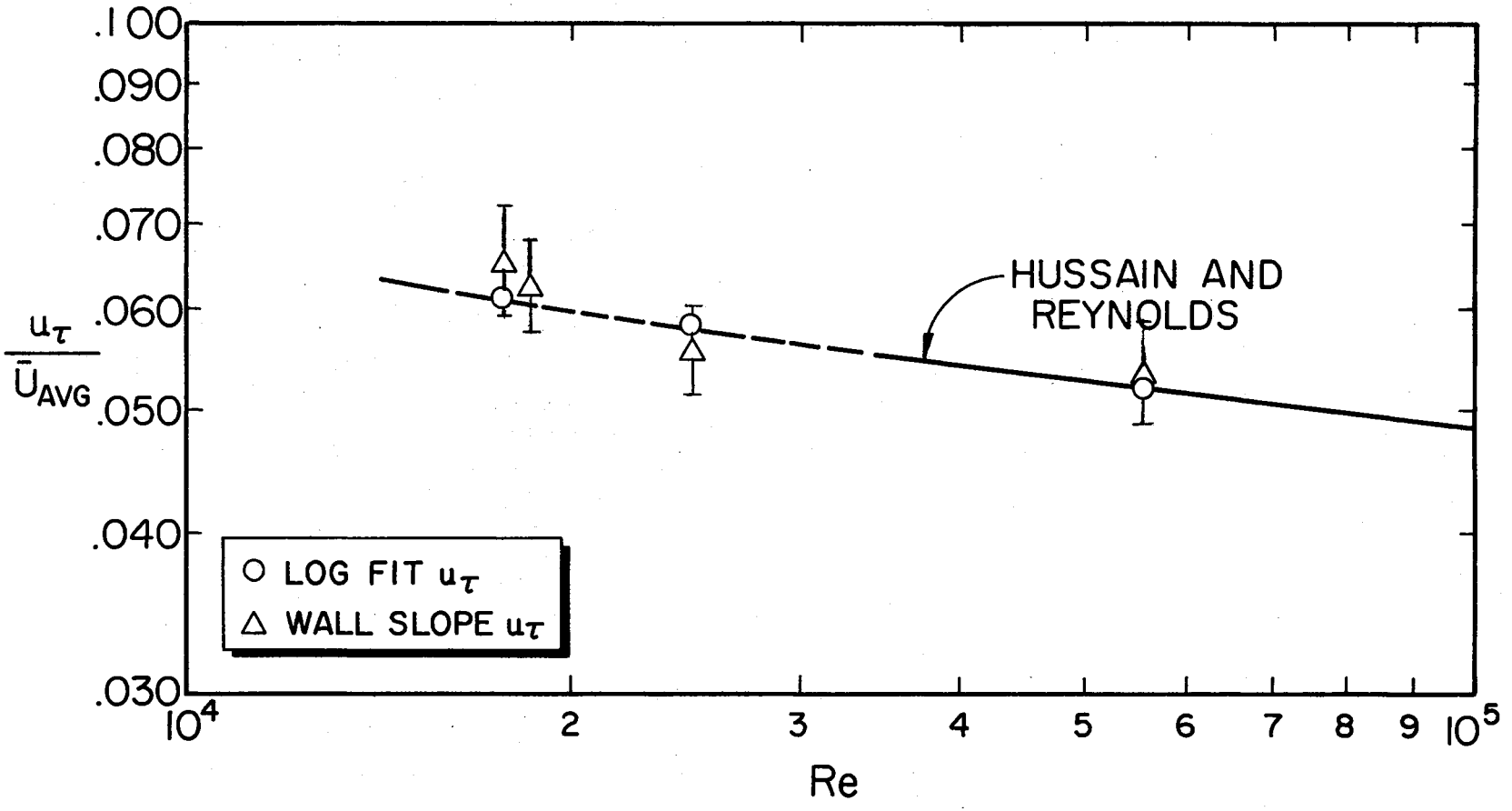

Figure 19. Shear Velocity Correlation

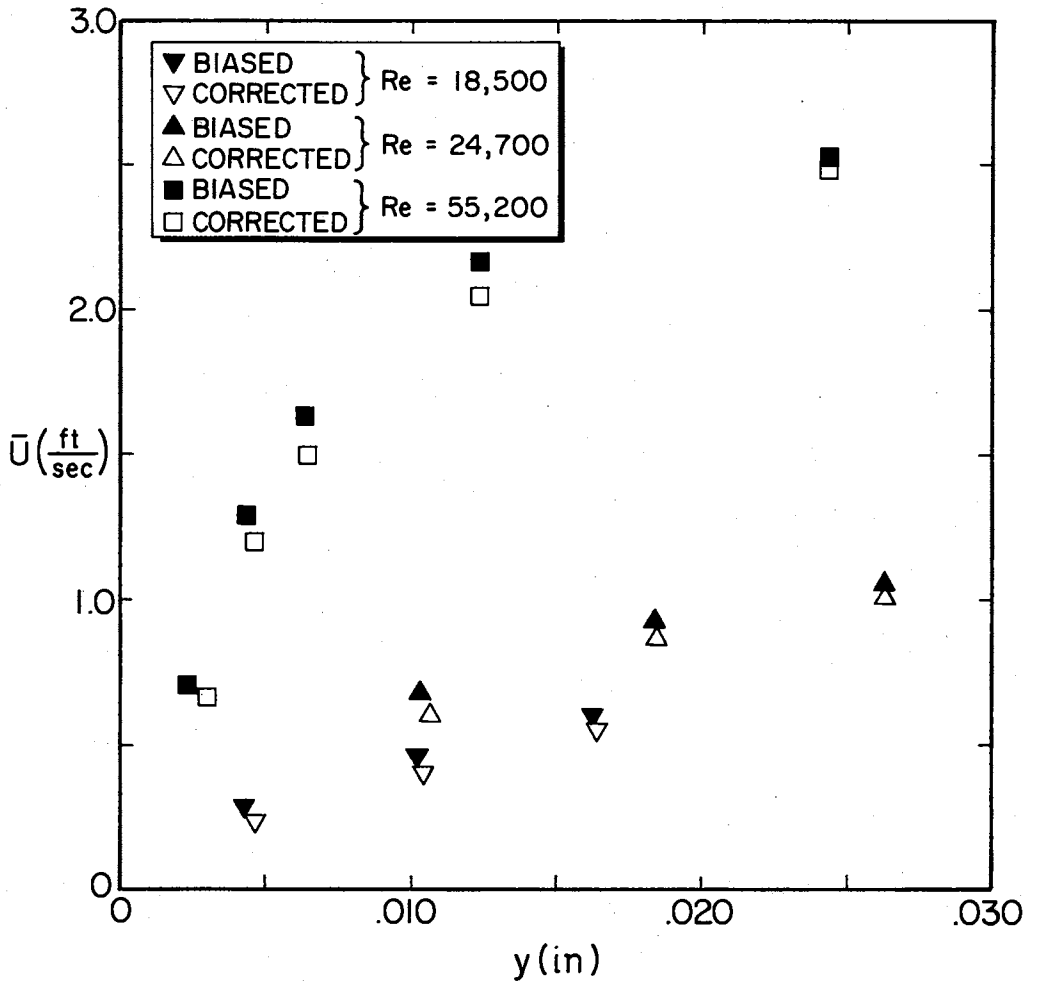

Figure 20. Comparison of Biased and Corrected Mean Velocities in Near-Wall Region

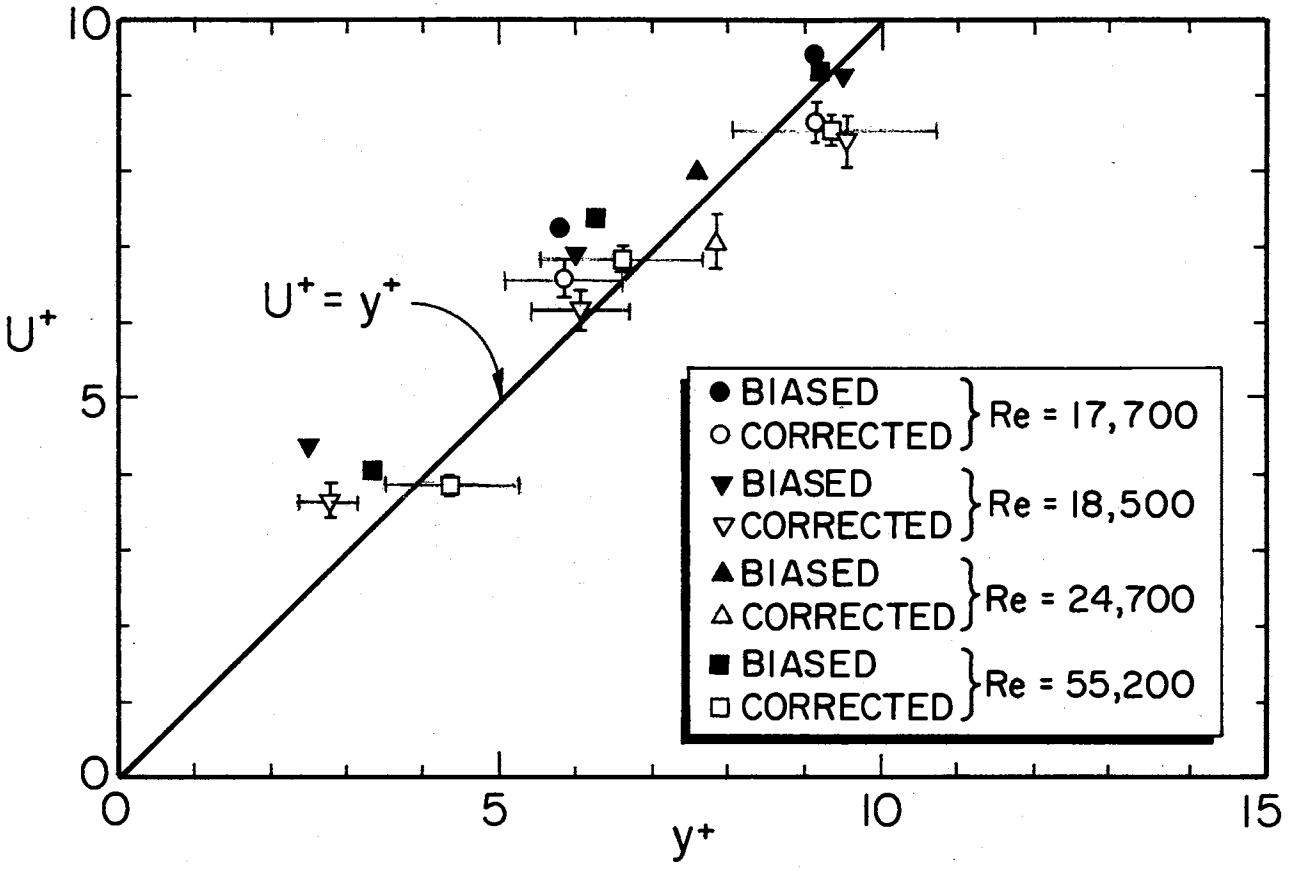

Figure 21. Non-Dimensional Near-Wall Mean Velocity Measurements

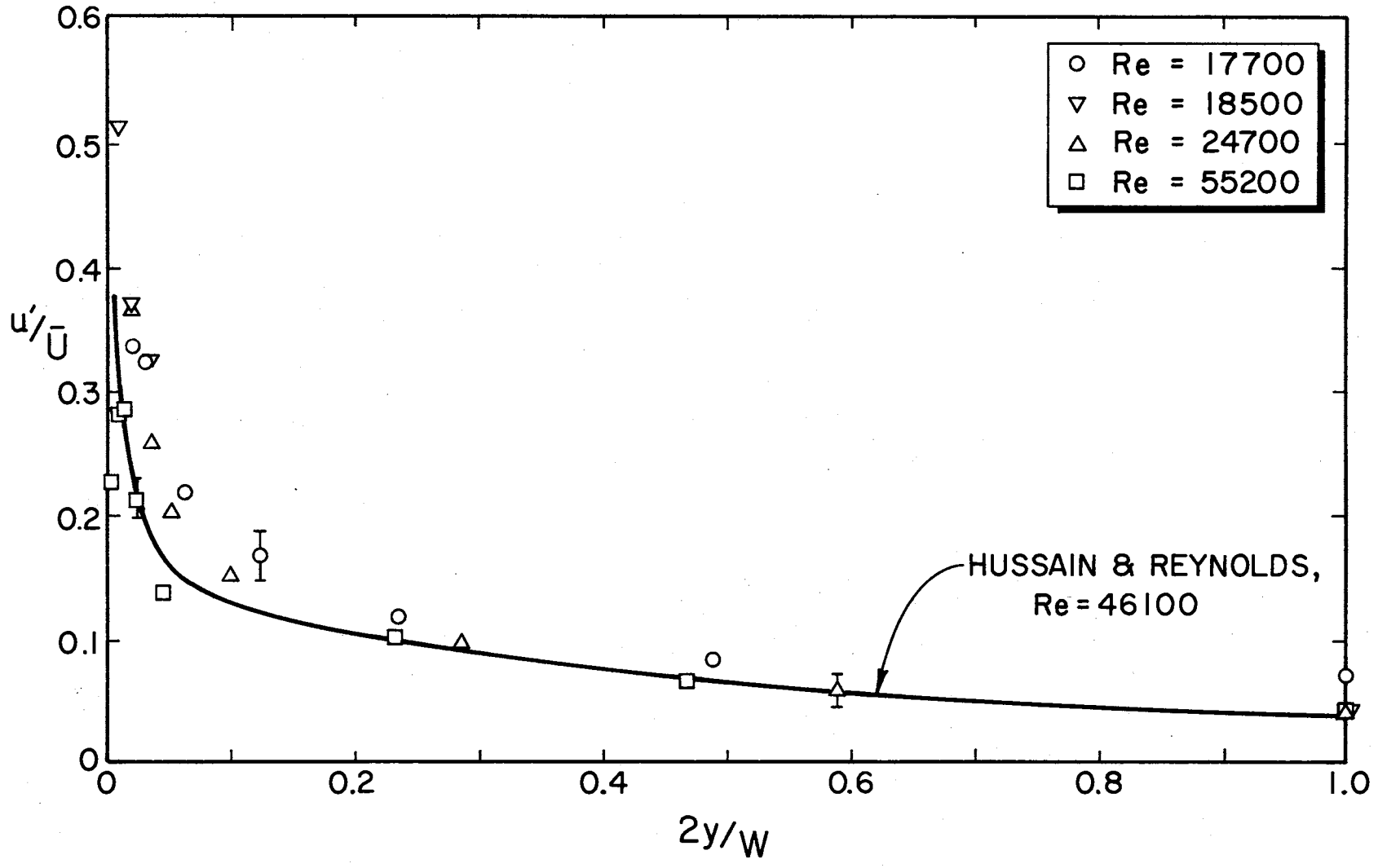

Figure 22. Streamwise Turbulent Intensities

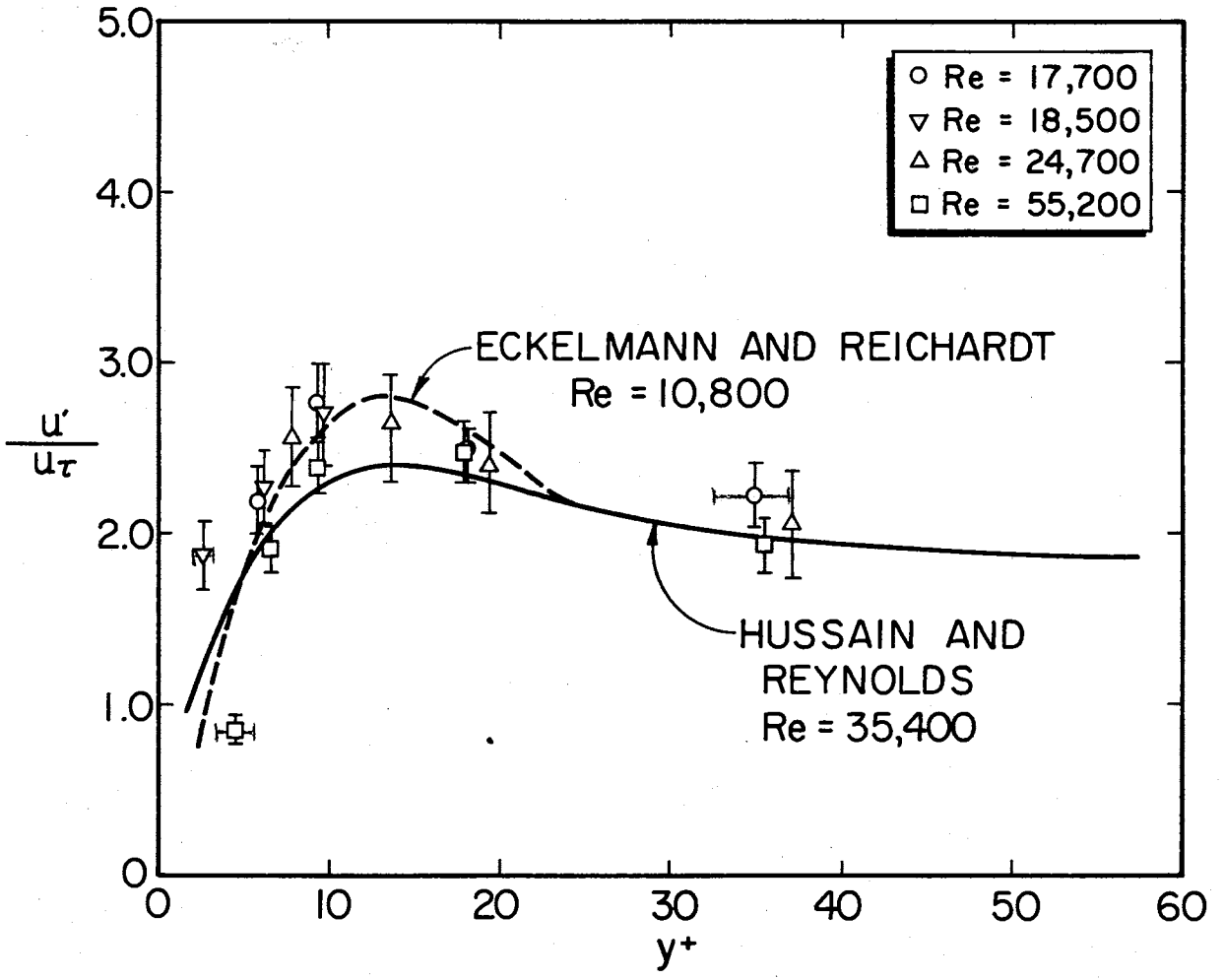

Figure 23. Streamwise Turbulent Intensities Normalized with Wall Layer Parameters

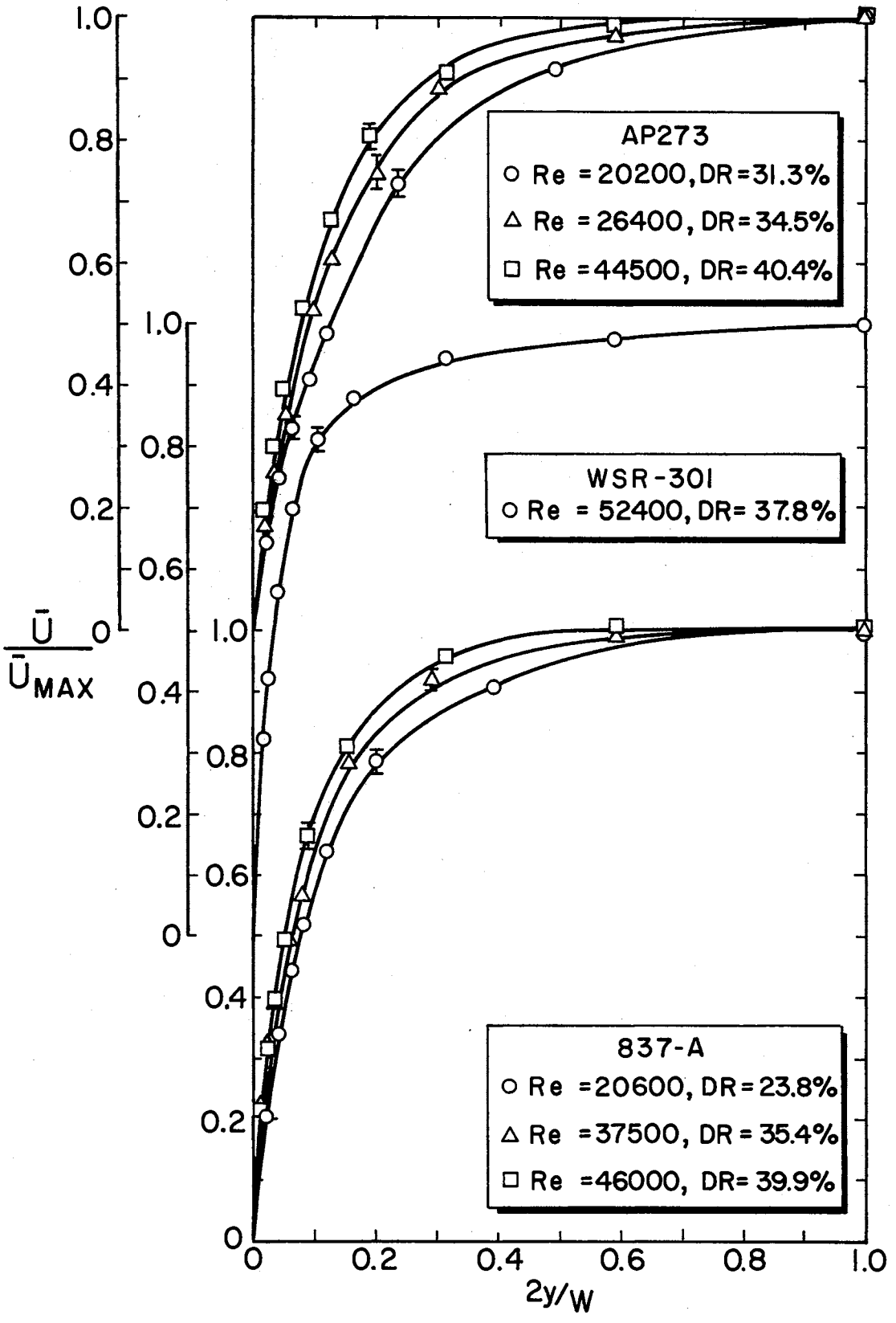

Figure 24. Mean Velocity Profiles for Drag-Reducing Flows

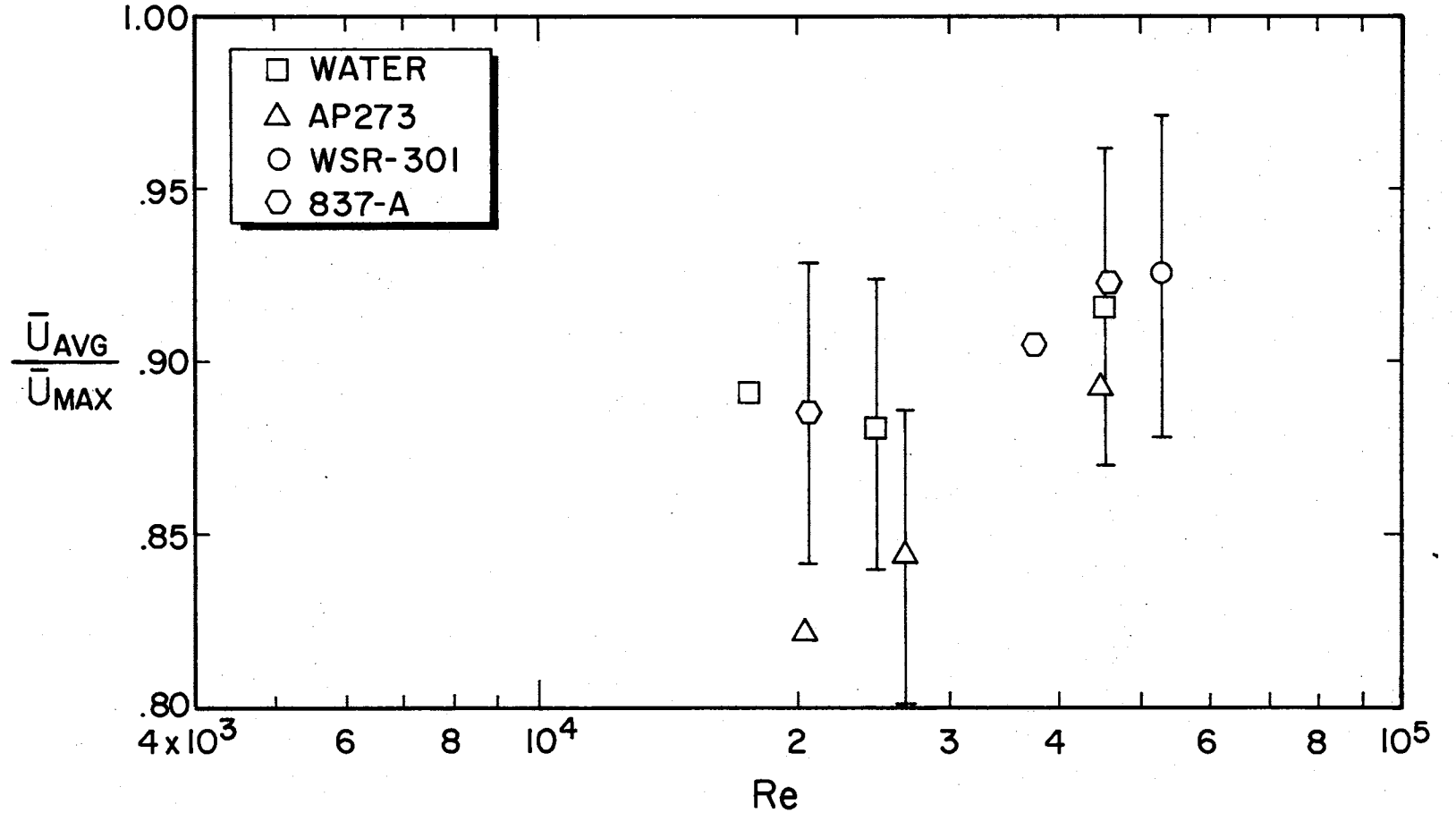

Figure 25. Ratio of Average to Maximum Velocities as a Function of Reynolds Number

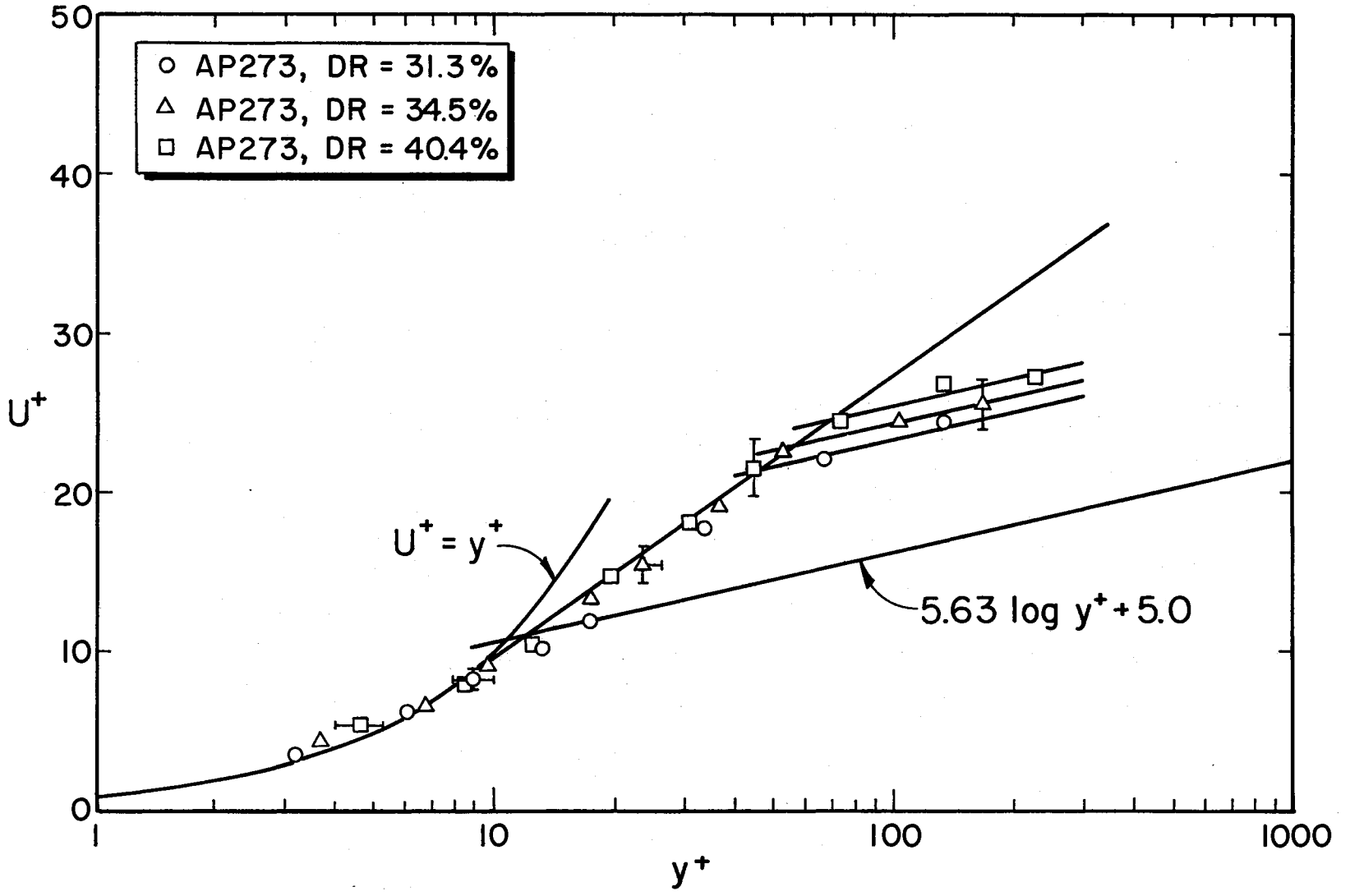

Figure 26. Non-Dimensional Mean Velocity Profiles for Separan AP273

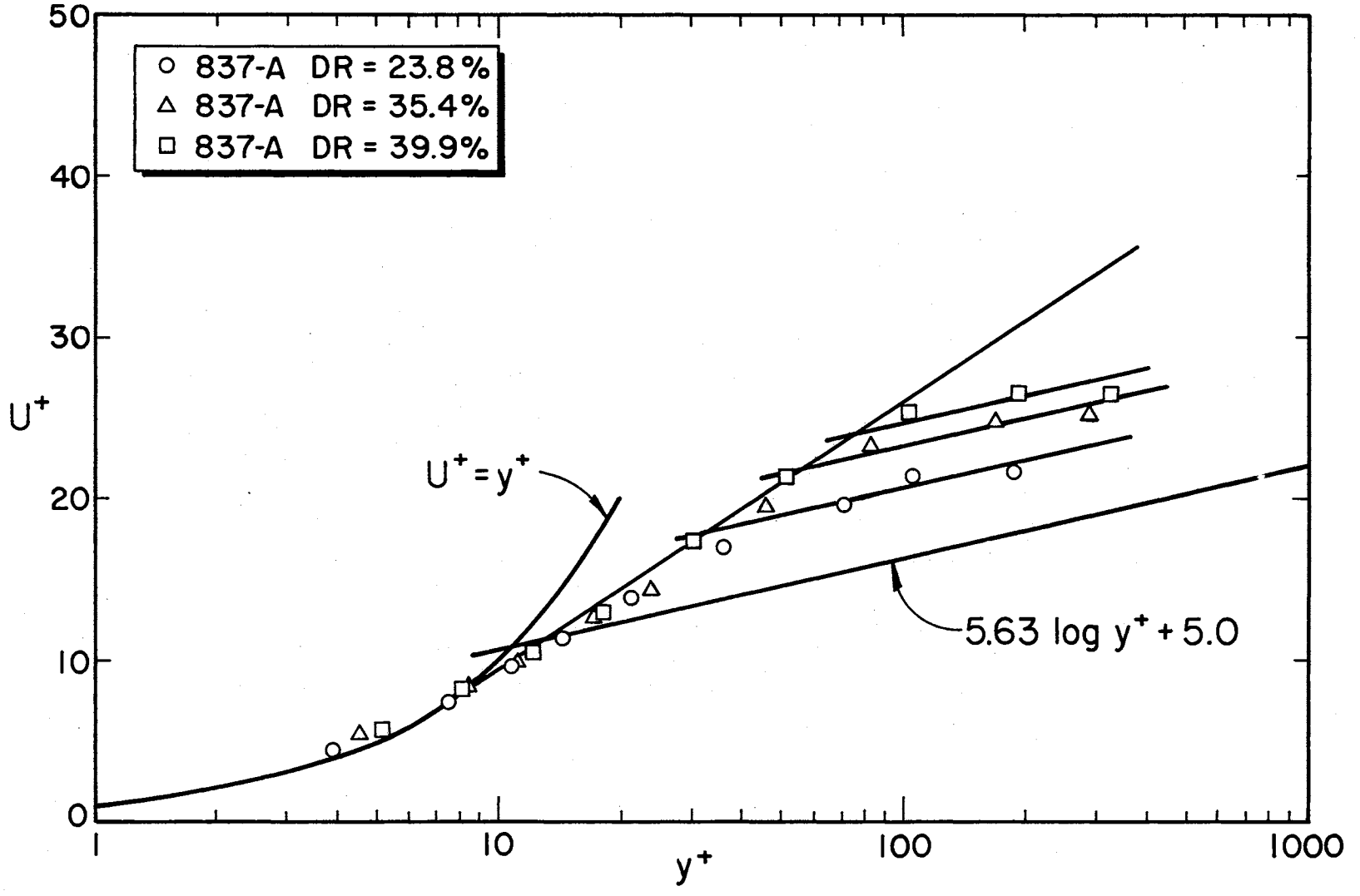

Figure 27. Non-Dimensional Mean Velocity Profiles for Magnifloc 837-A

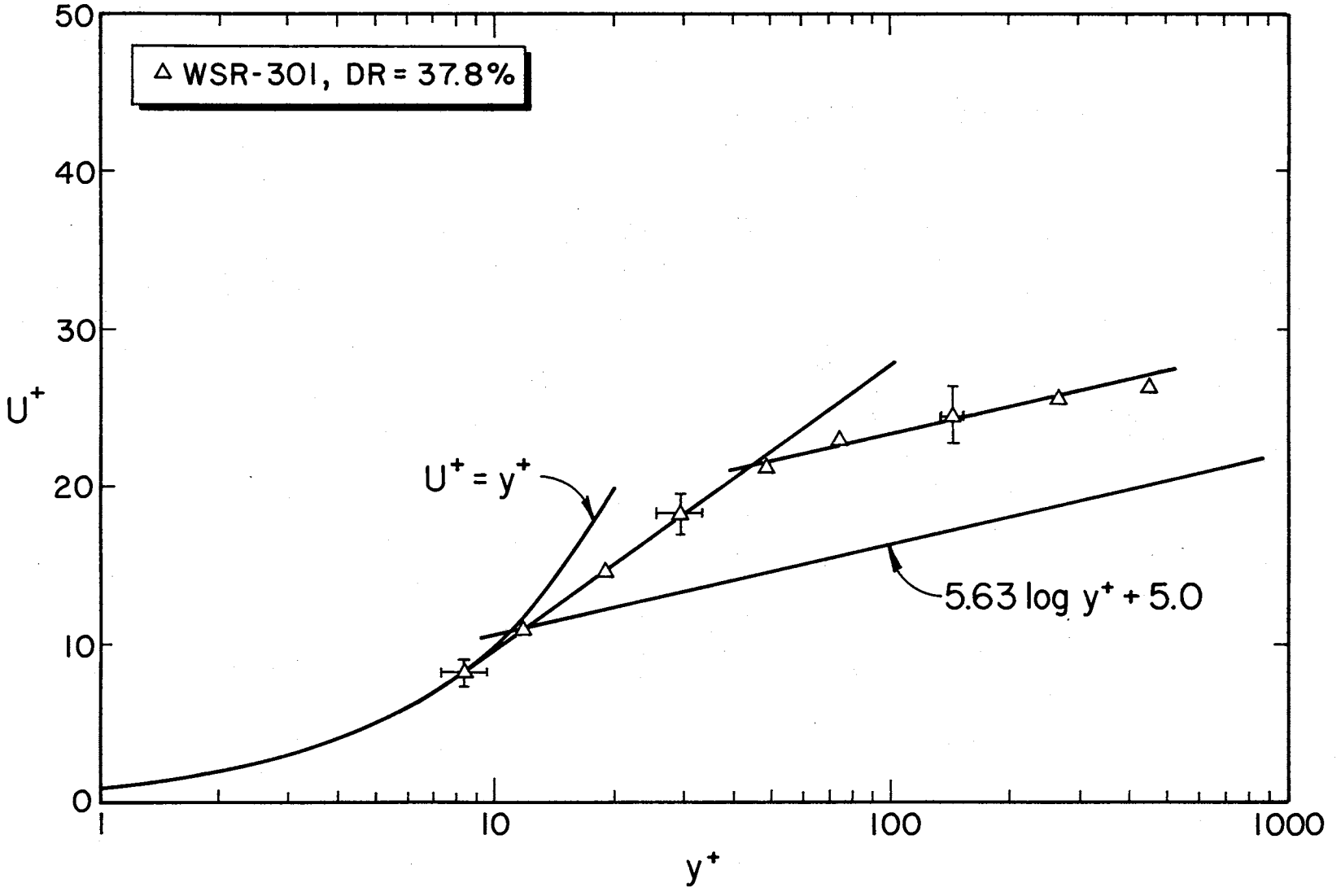

Figure 28. Non-Dimensional Mean Velocity Profile for Polyox WSR-301

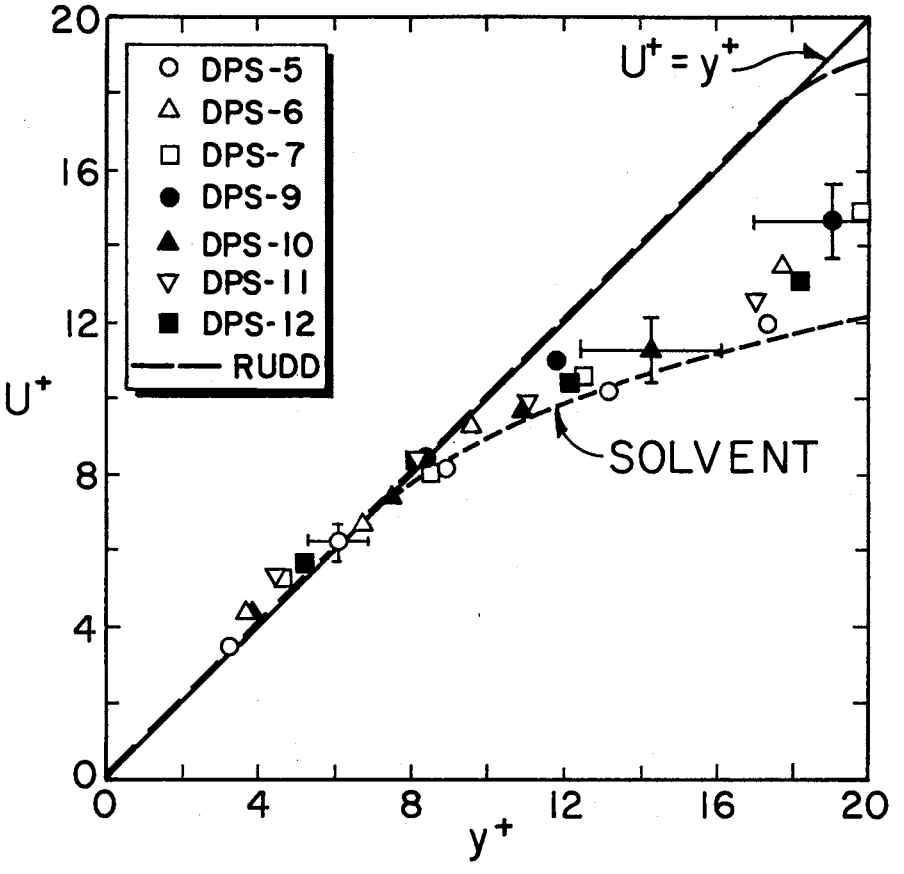

Figure 29. Normalized Mean Velocity Profiles for Drag-Reducing Flows - Near-Wall Region

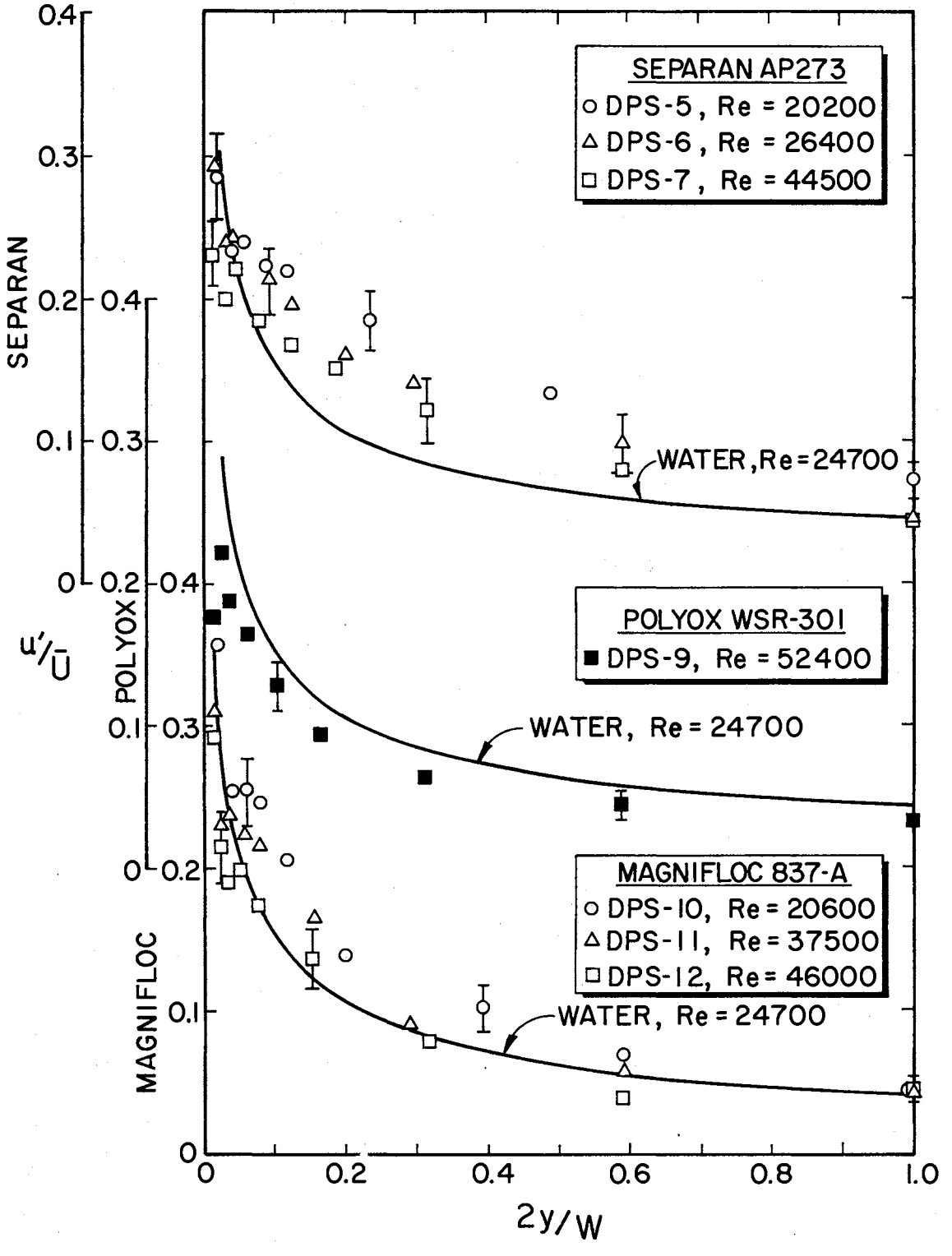

Figure 30. Streamwise Turbulent Intensities for Drag-Reducing Flows

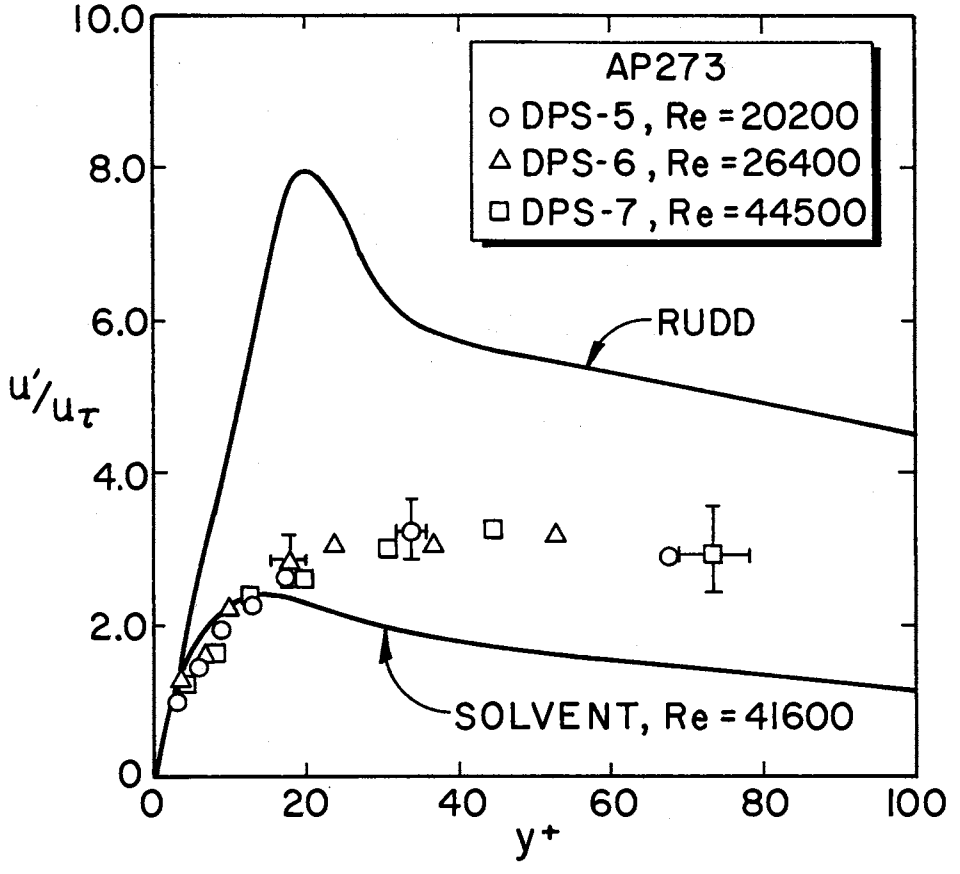

Figure 31. Near-Wall Turbulent Intensities for Separan AP273

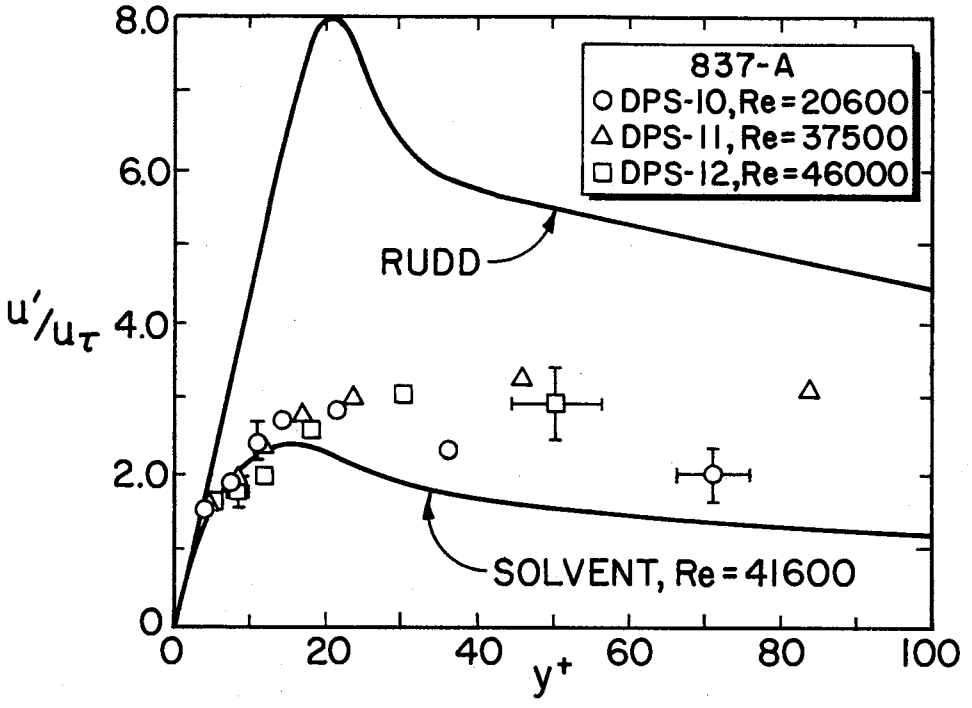

Figure 32. Near-Wall Turbulent Intensities for Magnifloc 837-A

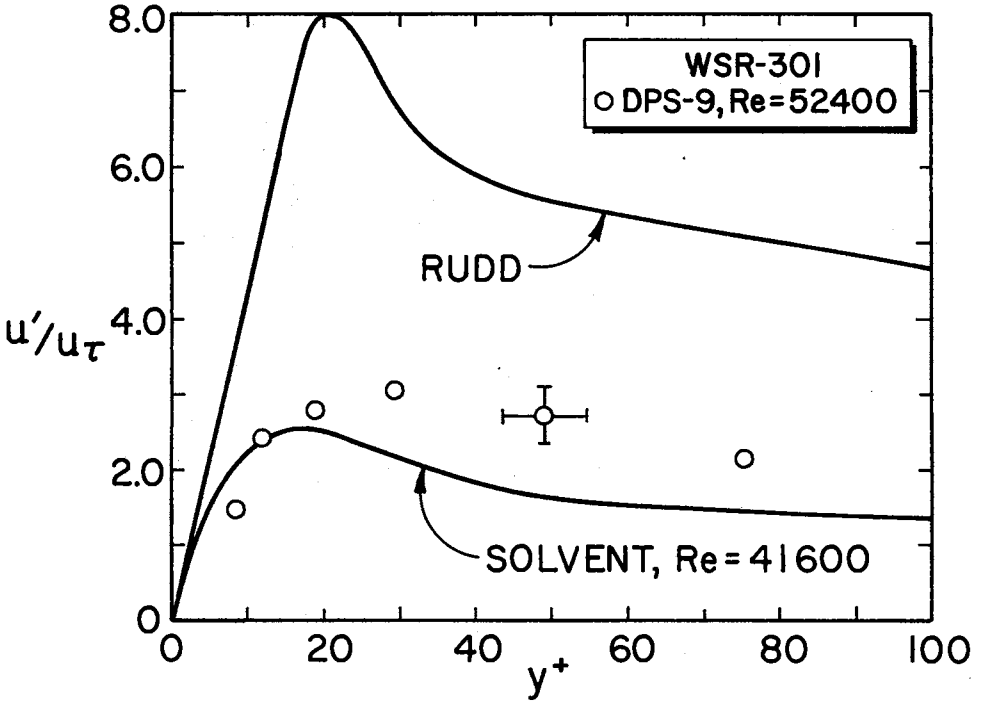

Figure 33. Near-Wall Turbulent Intensities for Polyox WSR-301

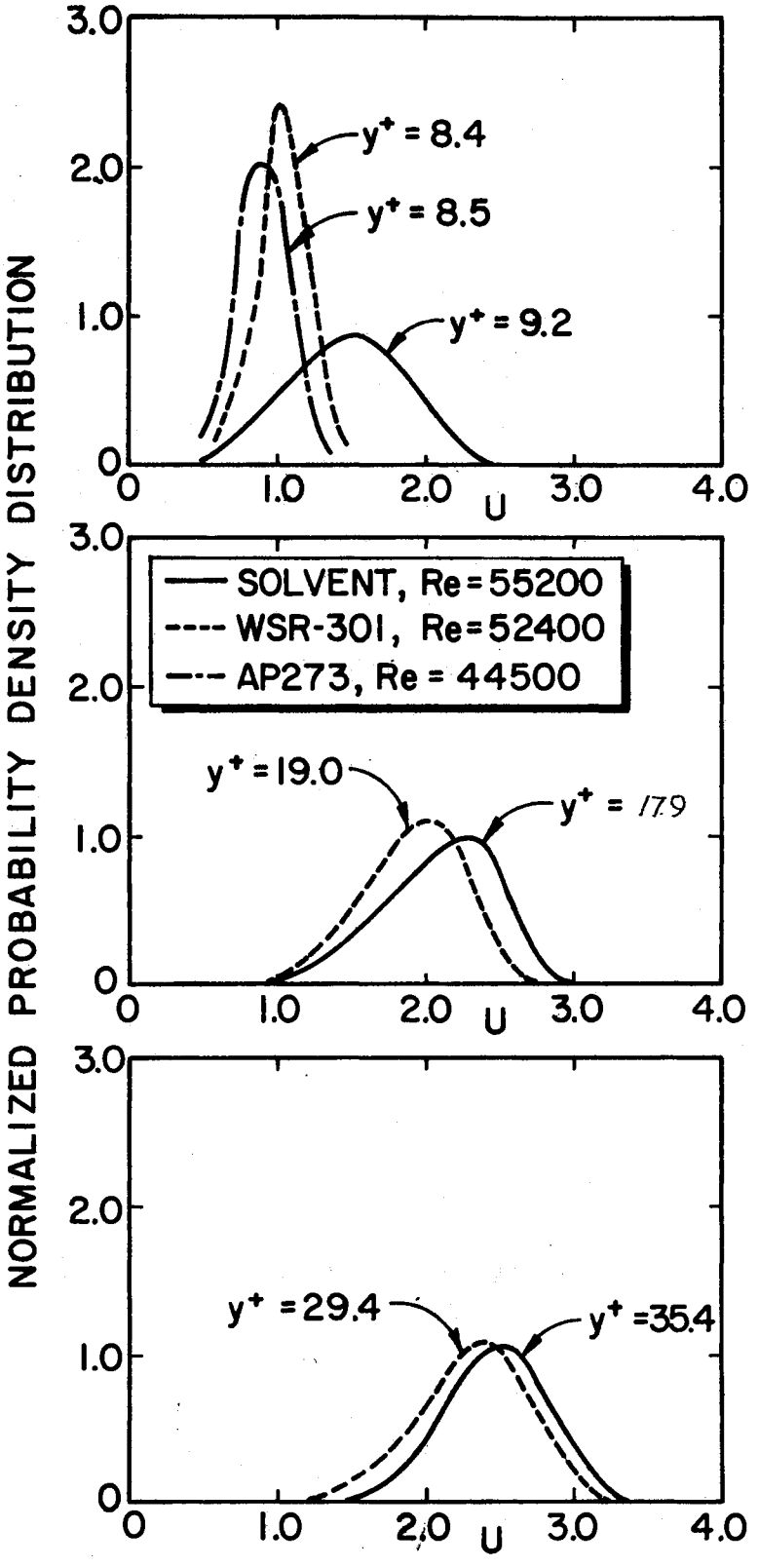

Figure 34. Comparison of Histograms for Drag-Reducing and Solvent Flows

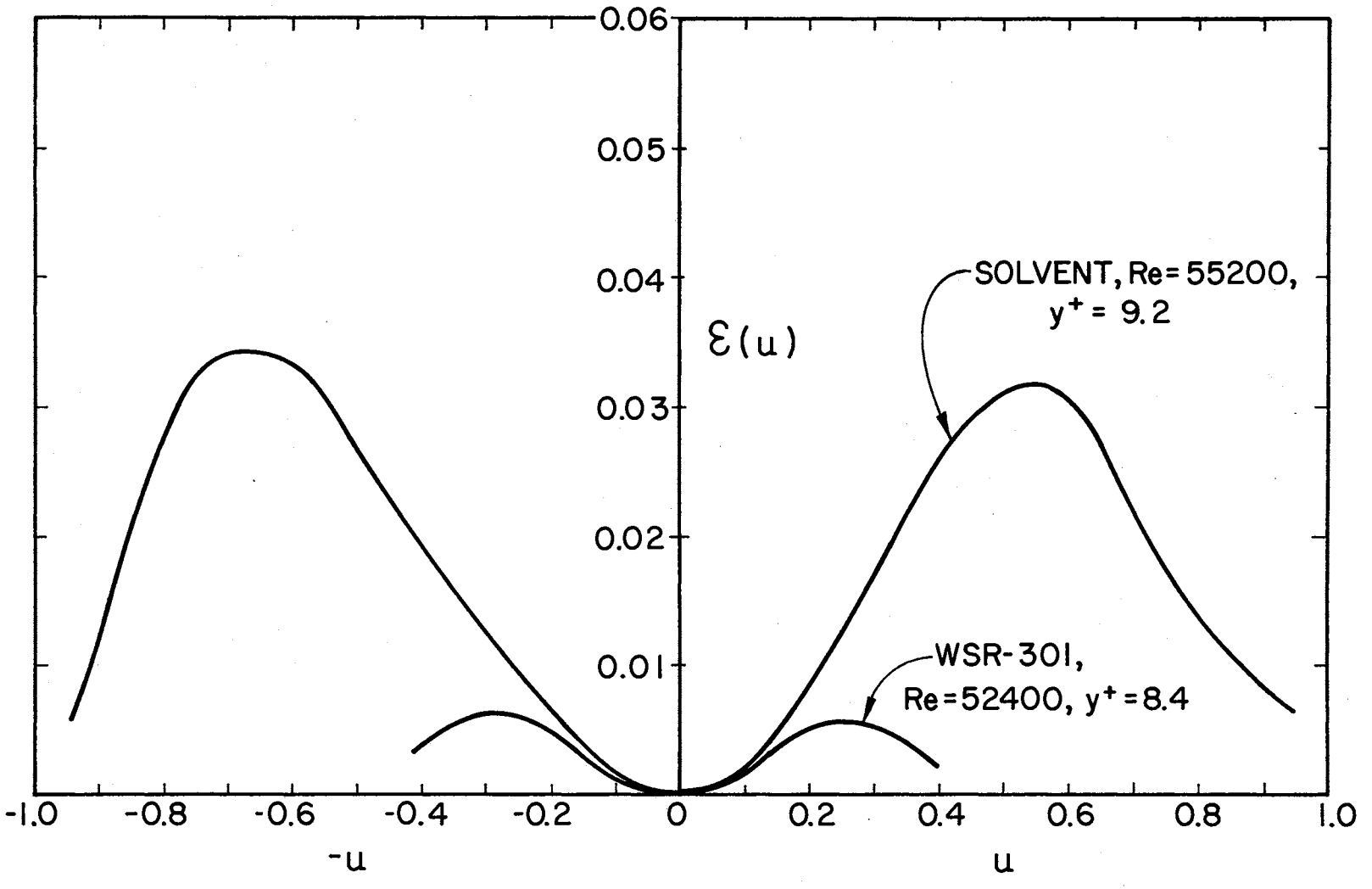

Figure 35. Energy Density Function Comparison ($y^+ \simeq 9$)

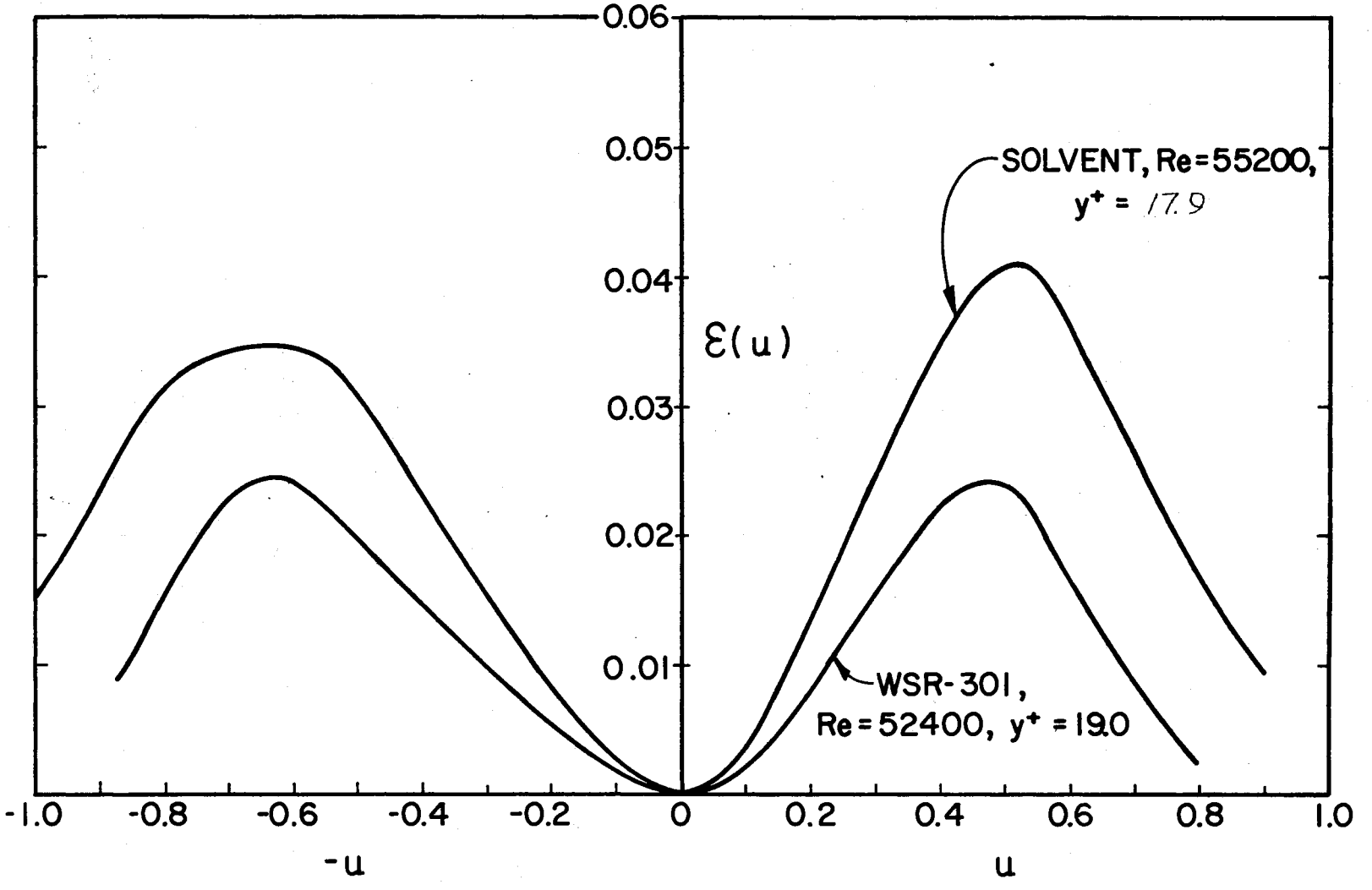

Figure 36. Energy Density Function Comparison ($y^+ \simeq 20$)

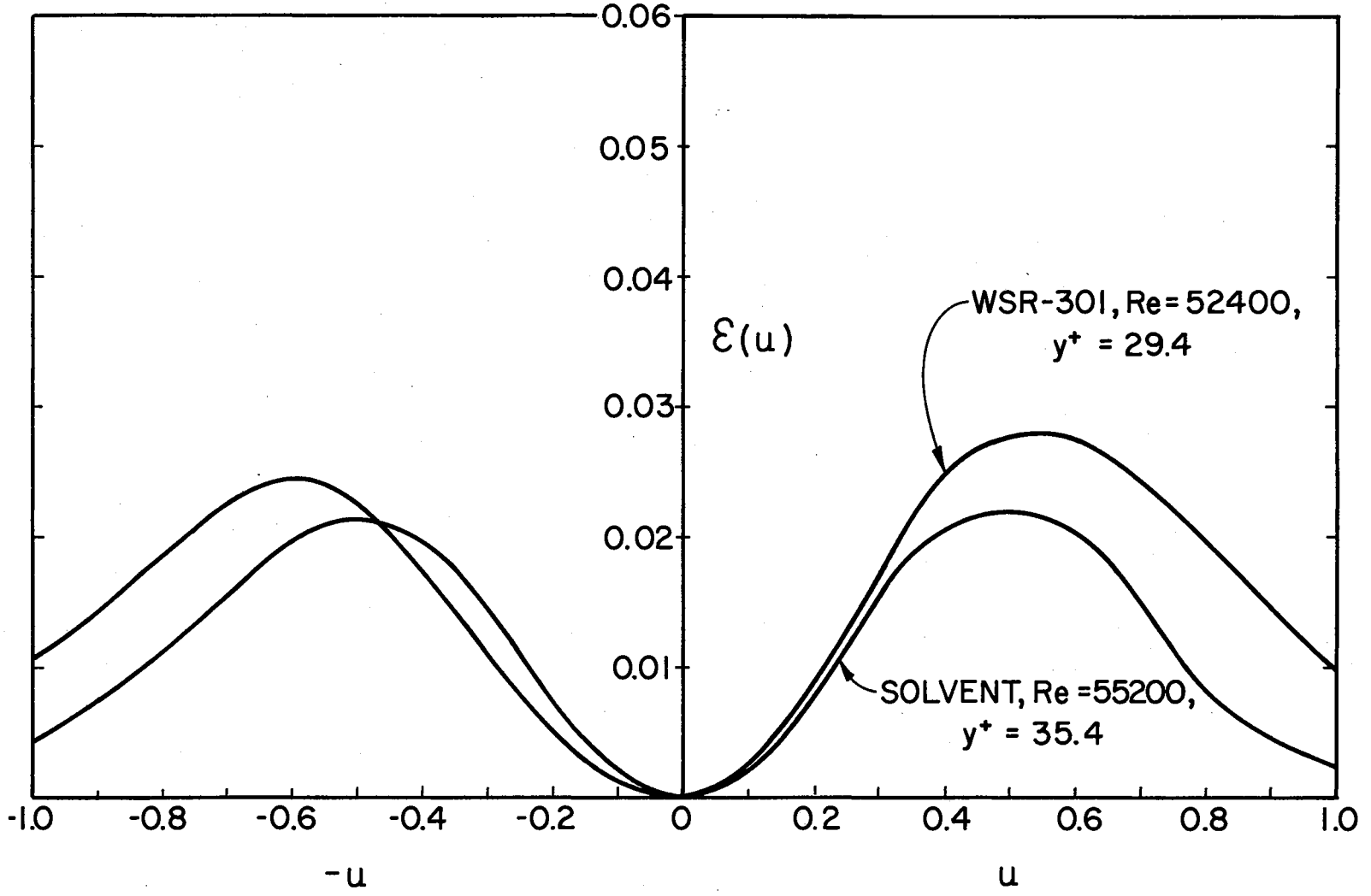

Figure 37. Energy Density Function Comparison ($y^+ \simeq 32$)

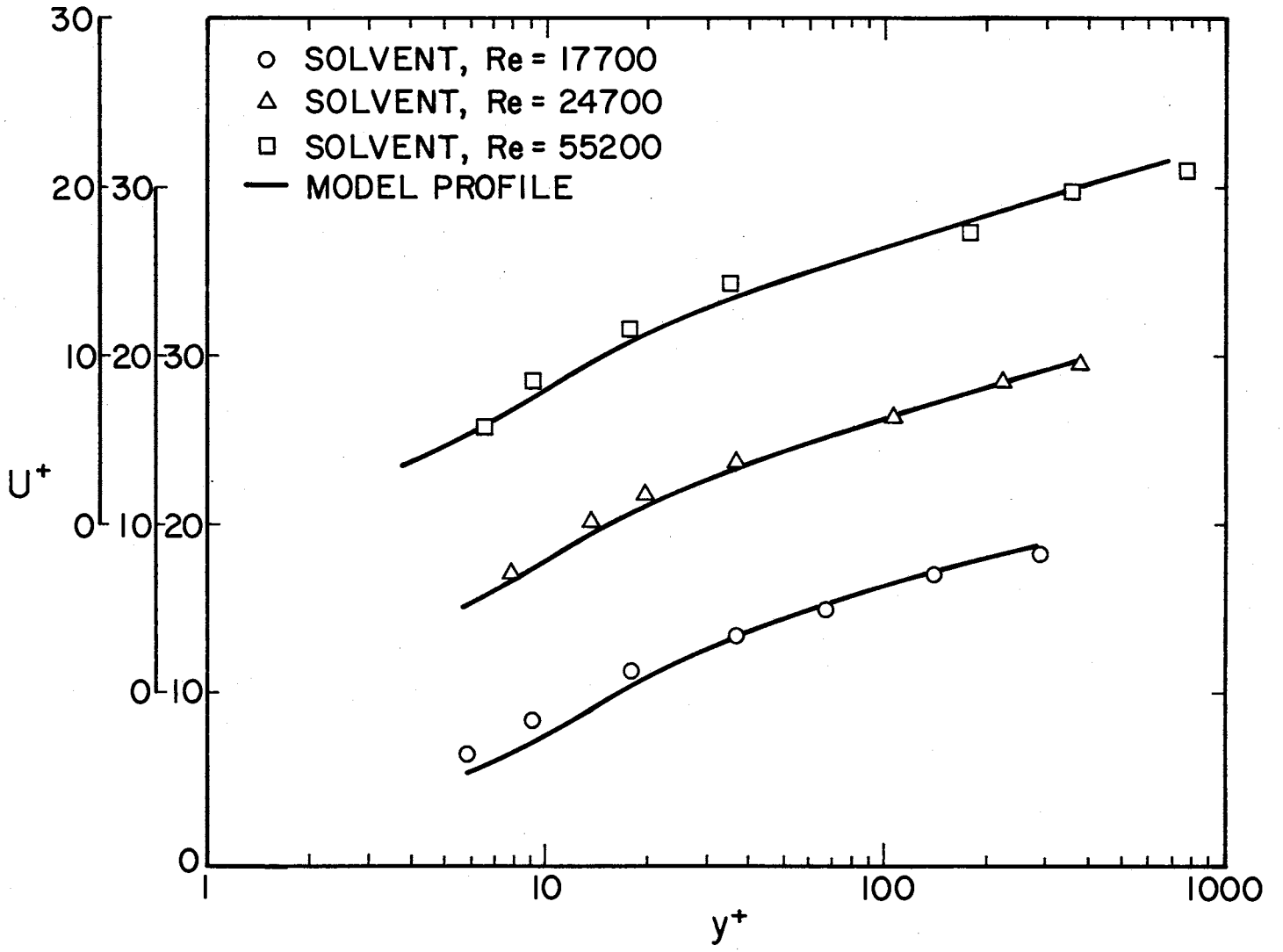

Figure 38. Comparison of Experimental and Calculated Velocity Profiles for the Solvent Flows

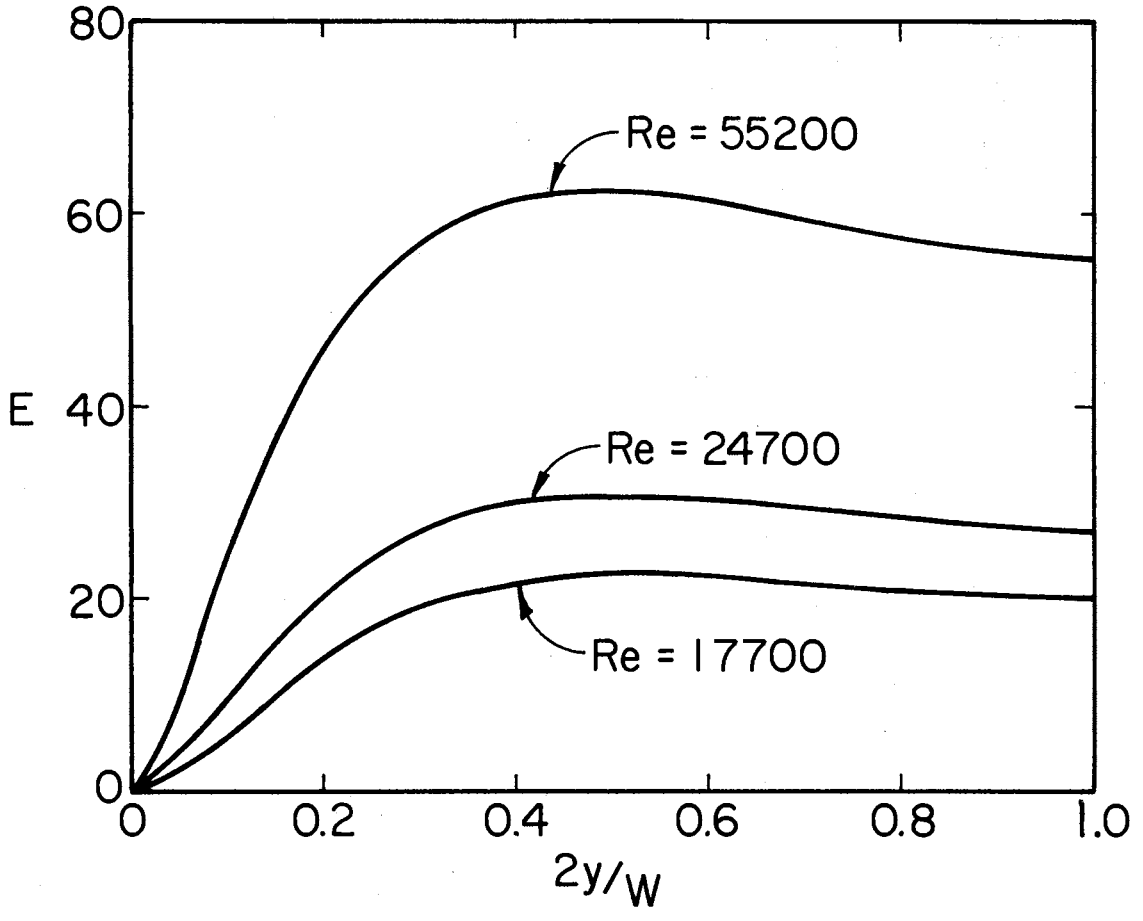

Figure 39. Eddy Diffusivities for Solvent Flows

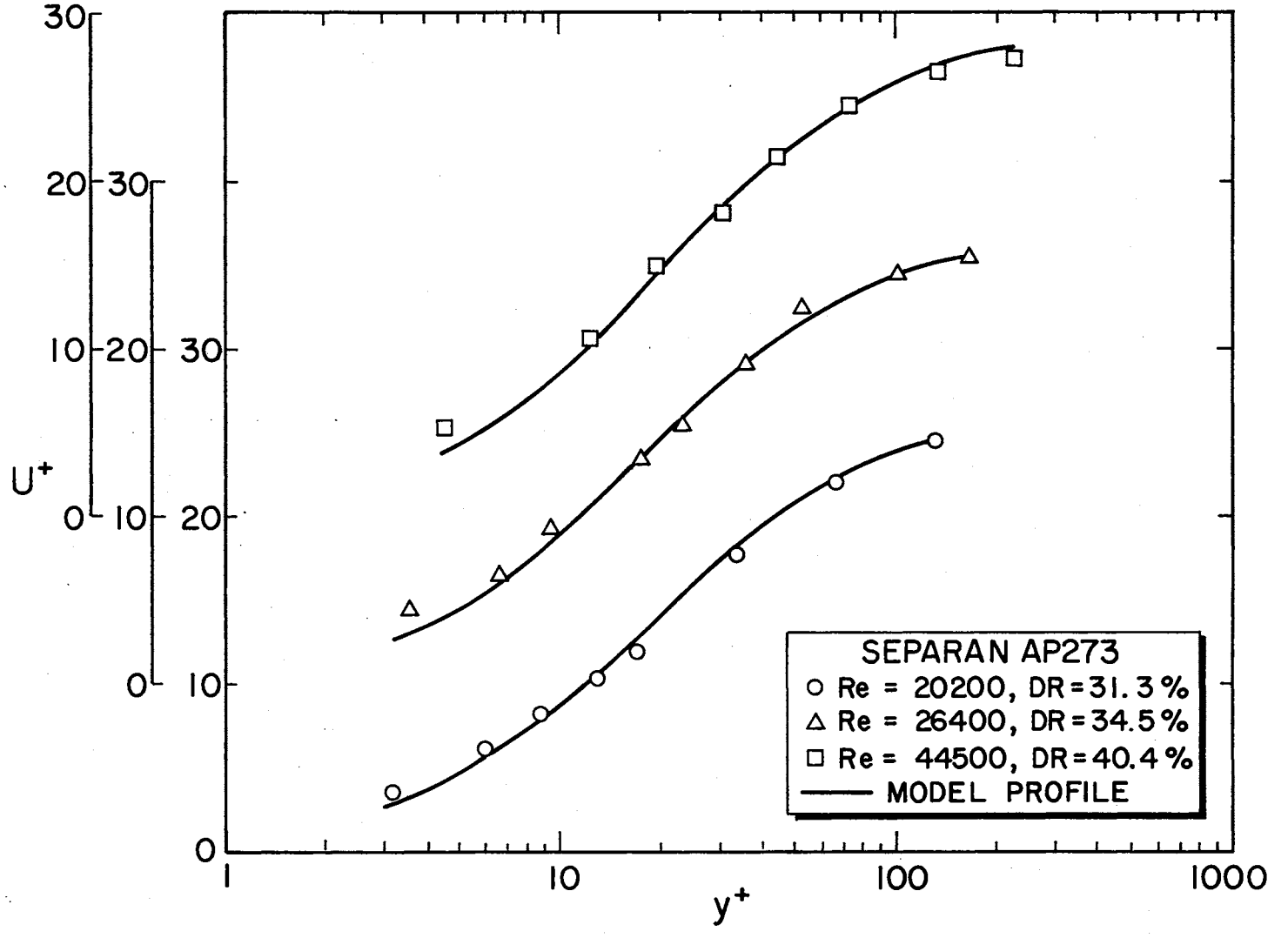

Figure 40. Comparison of Experimental and Calculated Velocity Profiles for Separan AP273

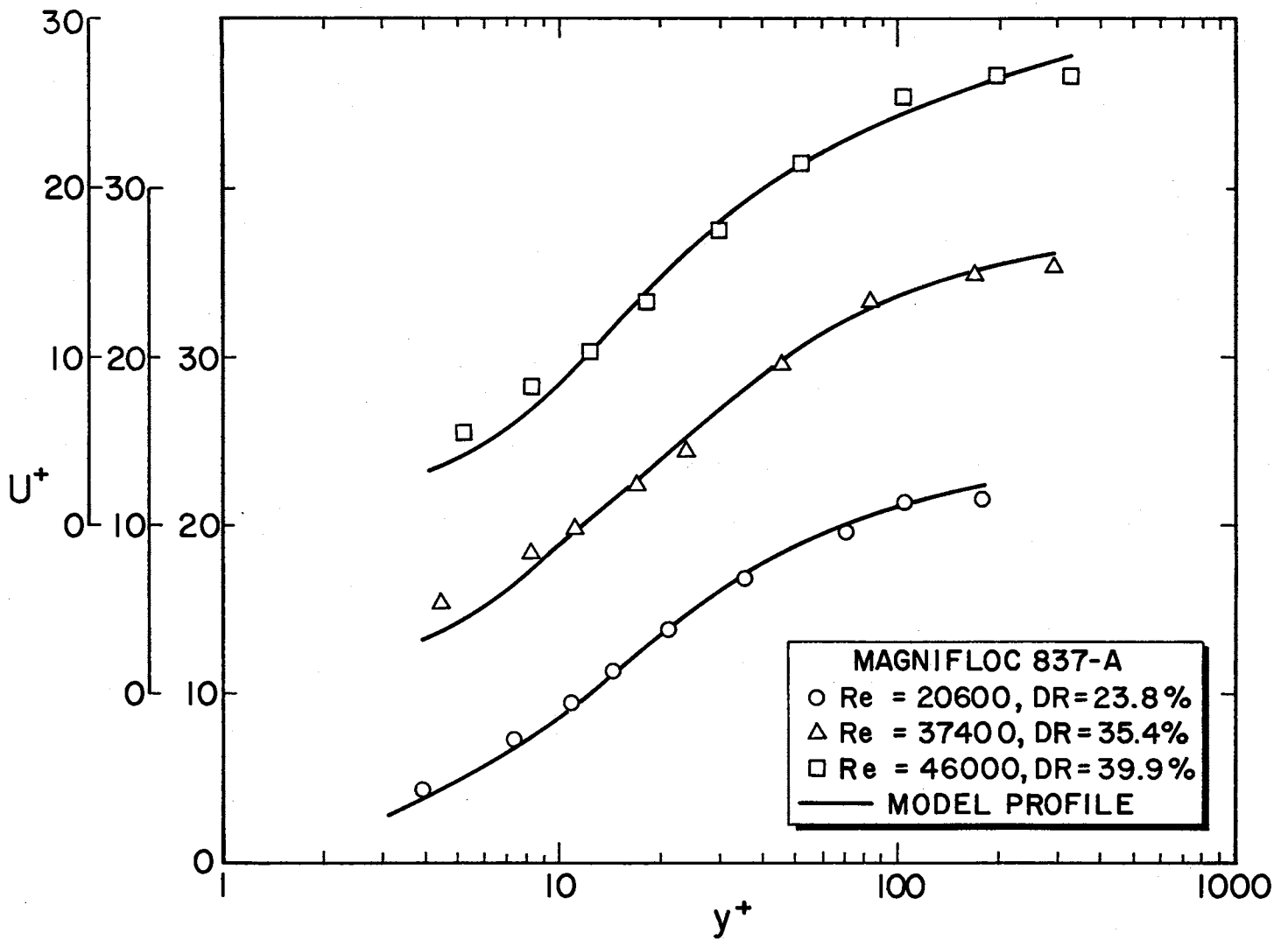

Figure 41. Comparison of Experimental and Calculated Velocity Profiles for Magnifloc 837-A

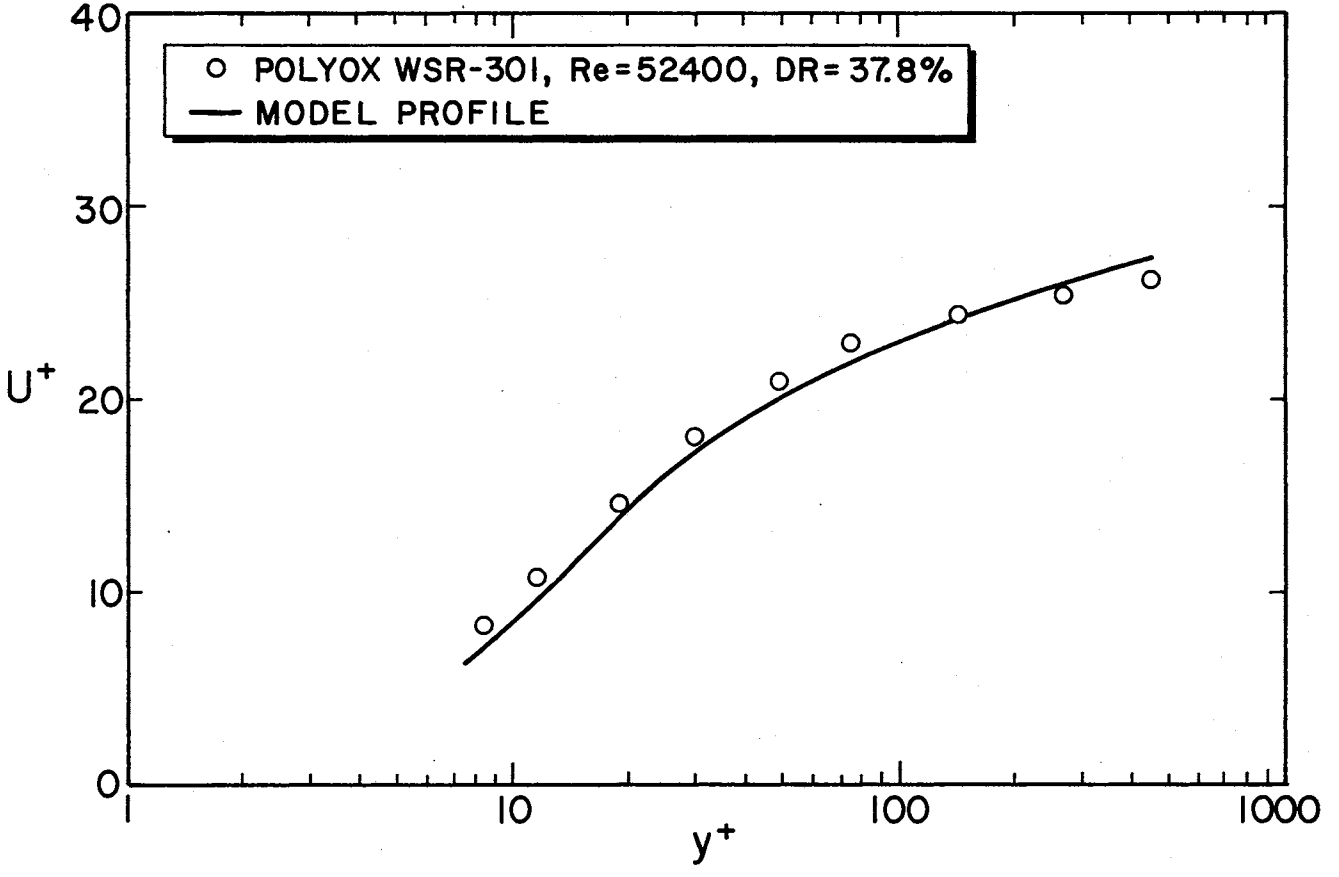

Figure 42. Comparison of Experimental and Calculated Velocity Profile for Polyox WSR-301

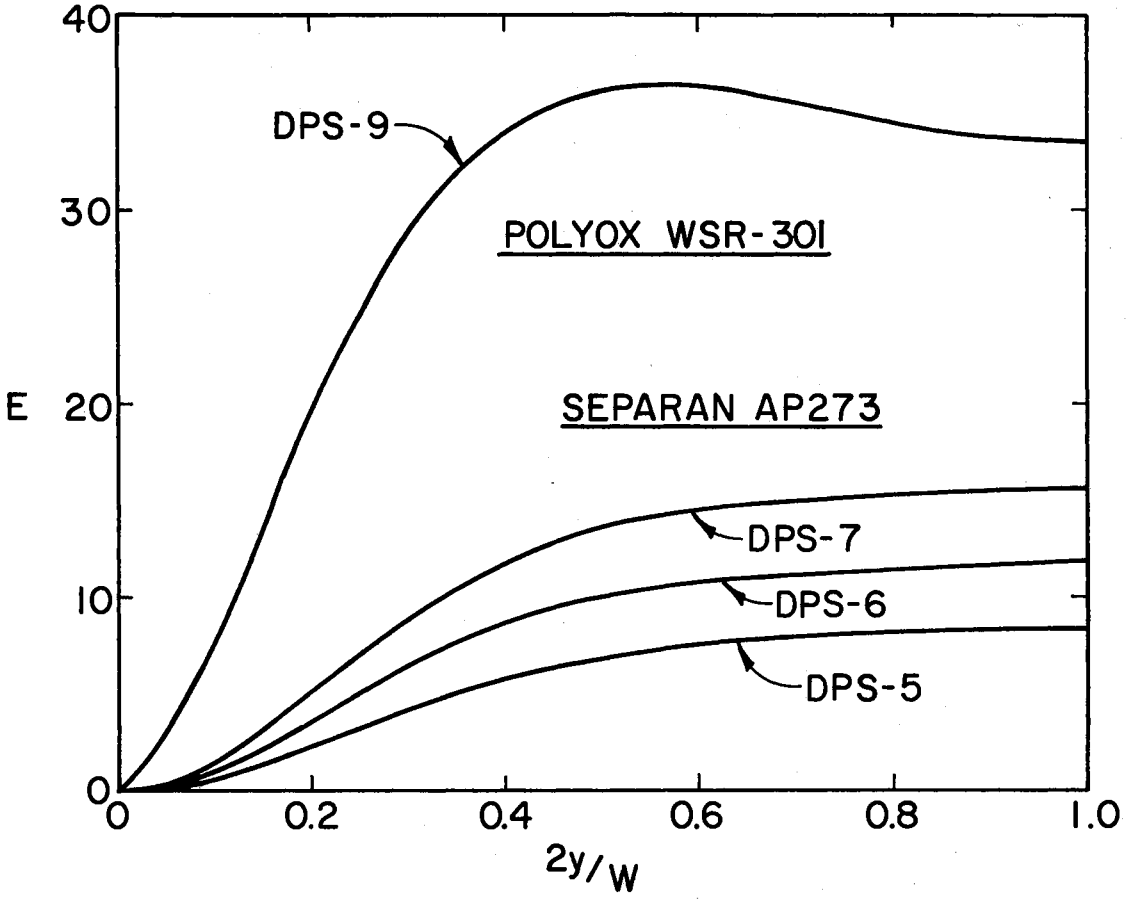

Figure 43. Eddy Diffusivities for Drag-Reducing Flows of Polyox WSR-301 and Separan AP273

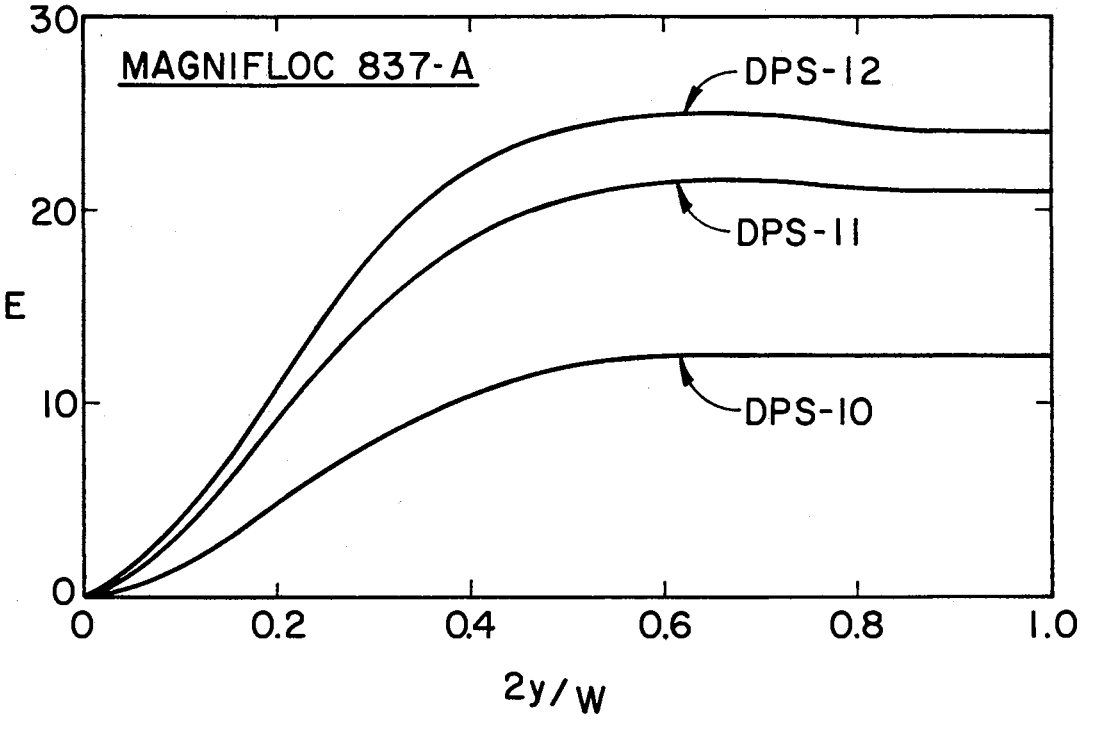

Figure 44. Eddy Diffusivities for Drag-Reducing Flow of Magnifloc 837-A

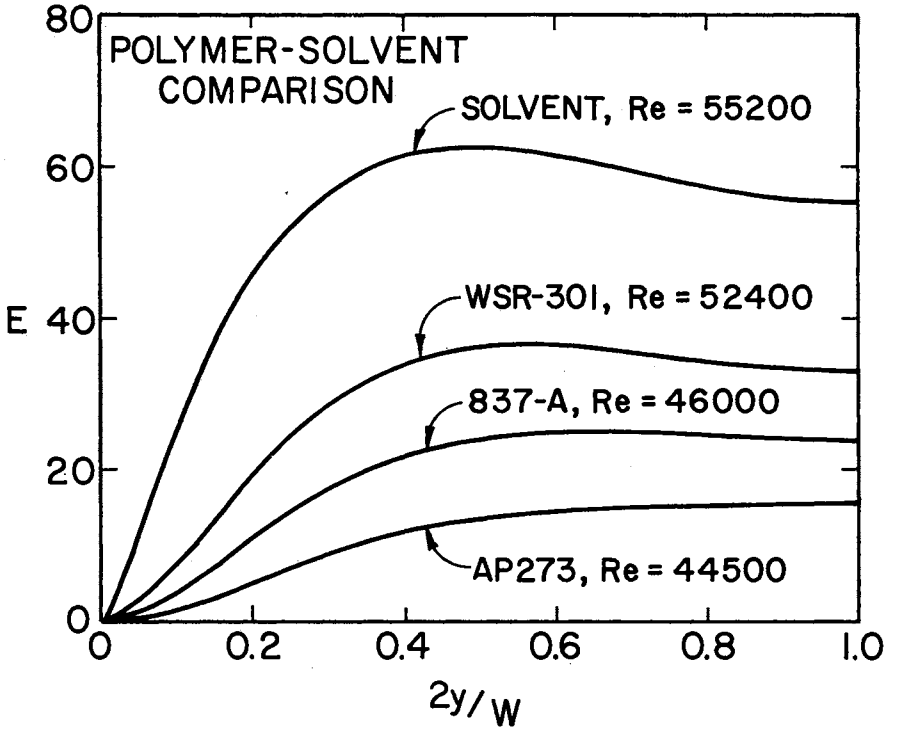

Figure 45. Comparison of Eddy Diffusivities for Solvent and Drag-Reducing Flows

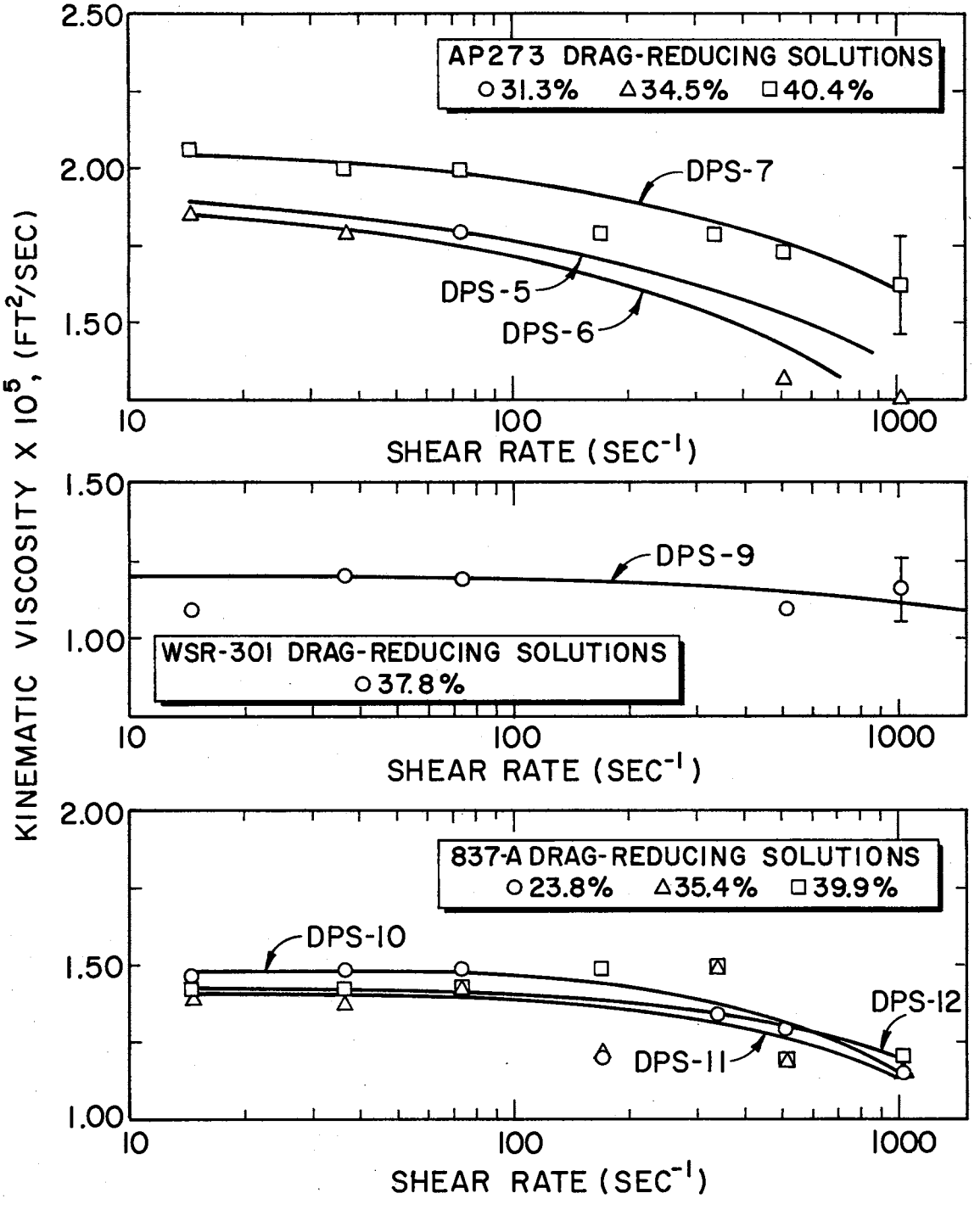

Figure 46. Effect of Shear Rate upon the Viscosity of the Drag-Reducing Solutions

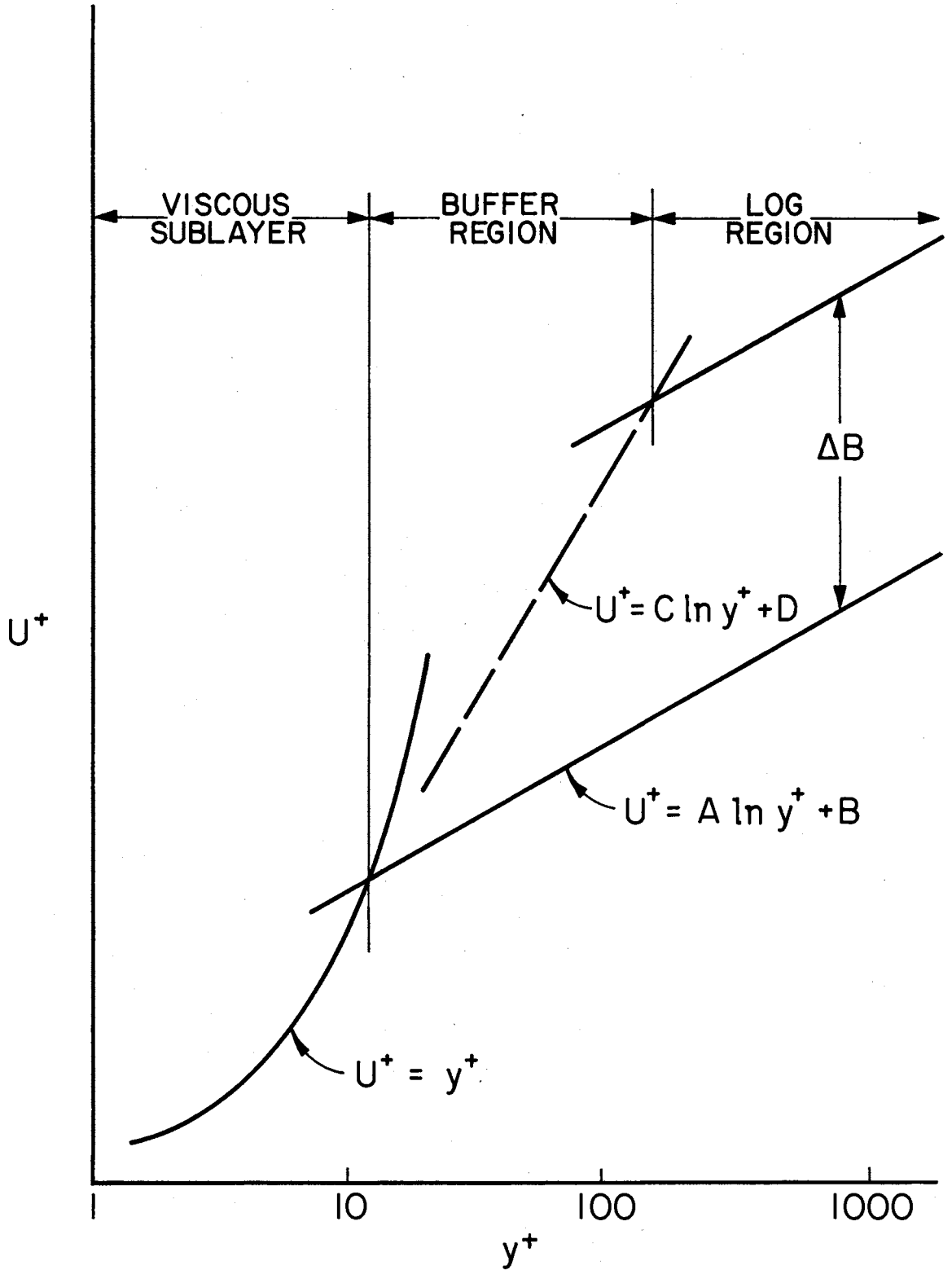

Figure 47. Generalized Non-Dimensional Velocity Profile

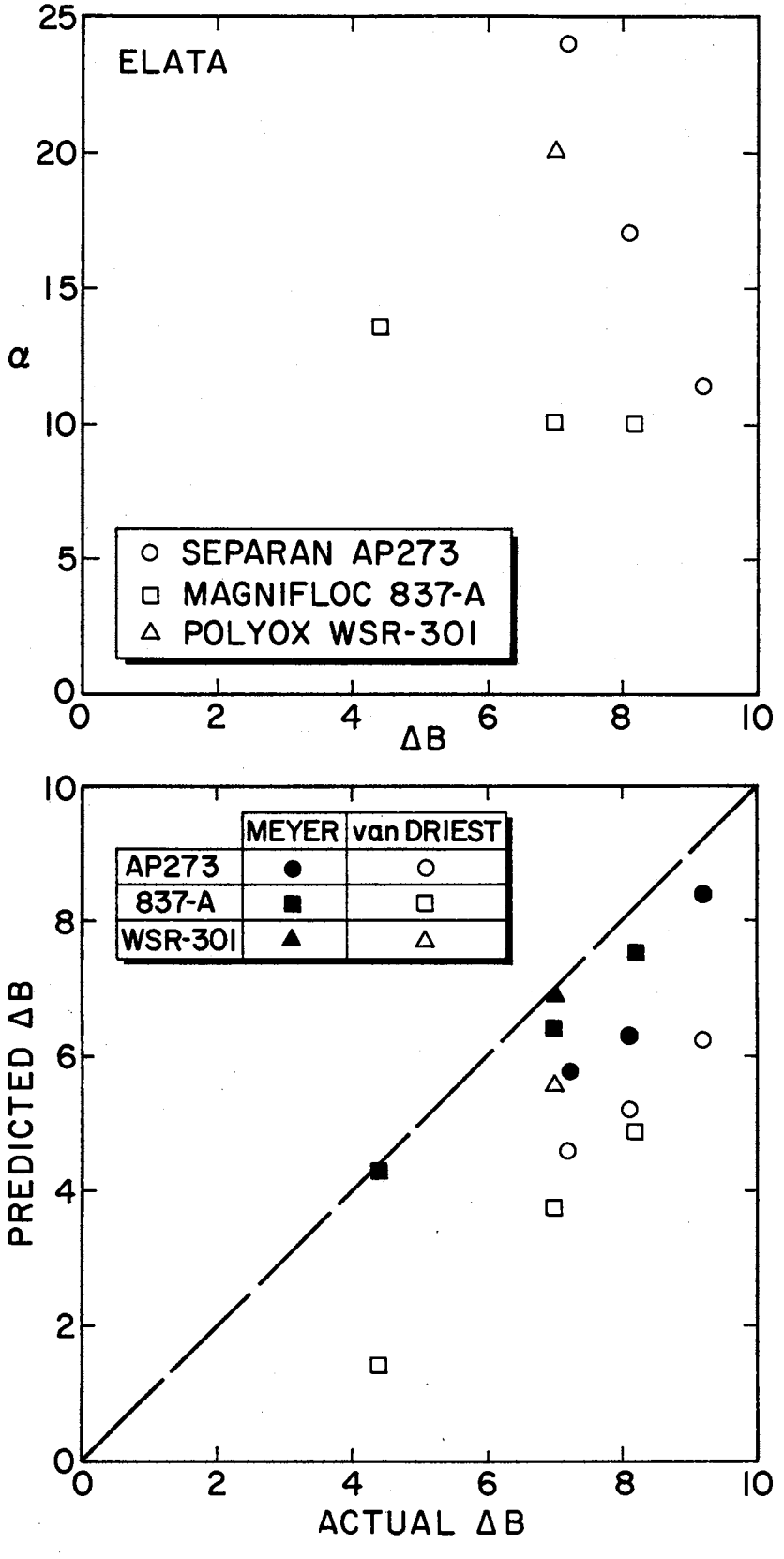

Figure 48. Evaluation of ΔB Predictors (Elata, Meyer, van Driest)

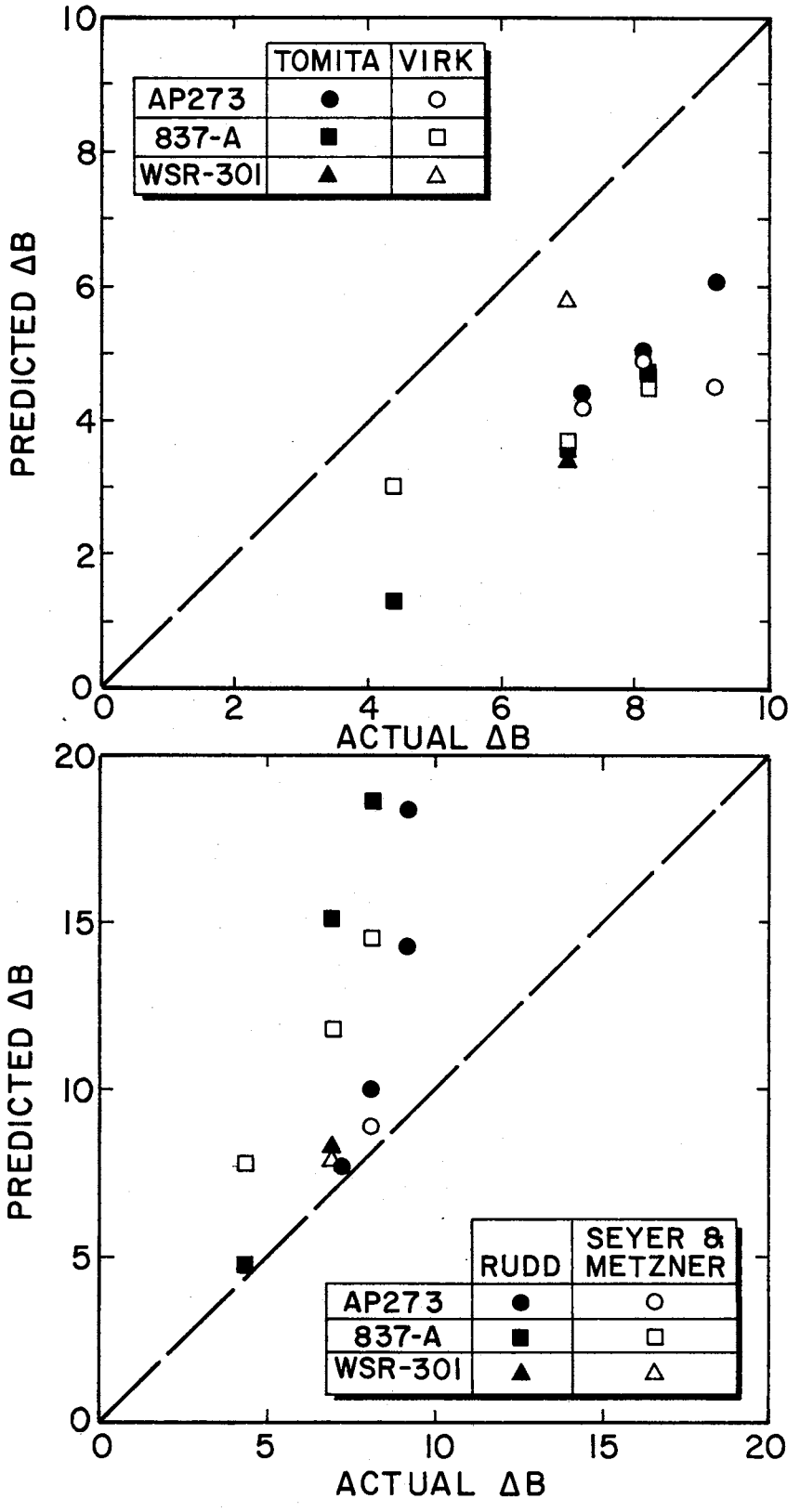

Figure 49. Evaluation of the ΔB Predictors

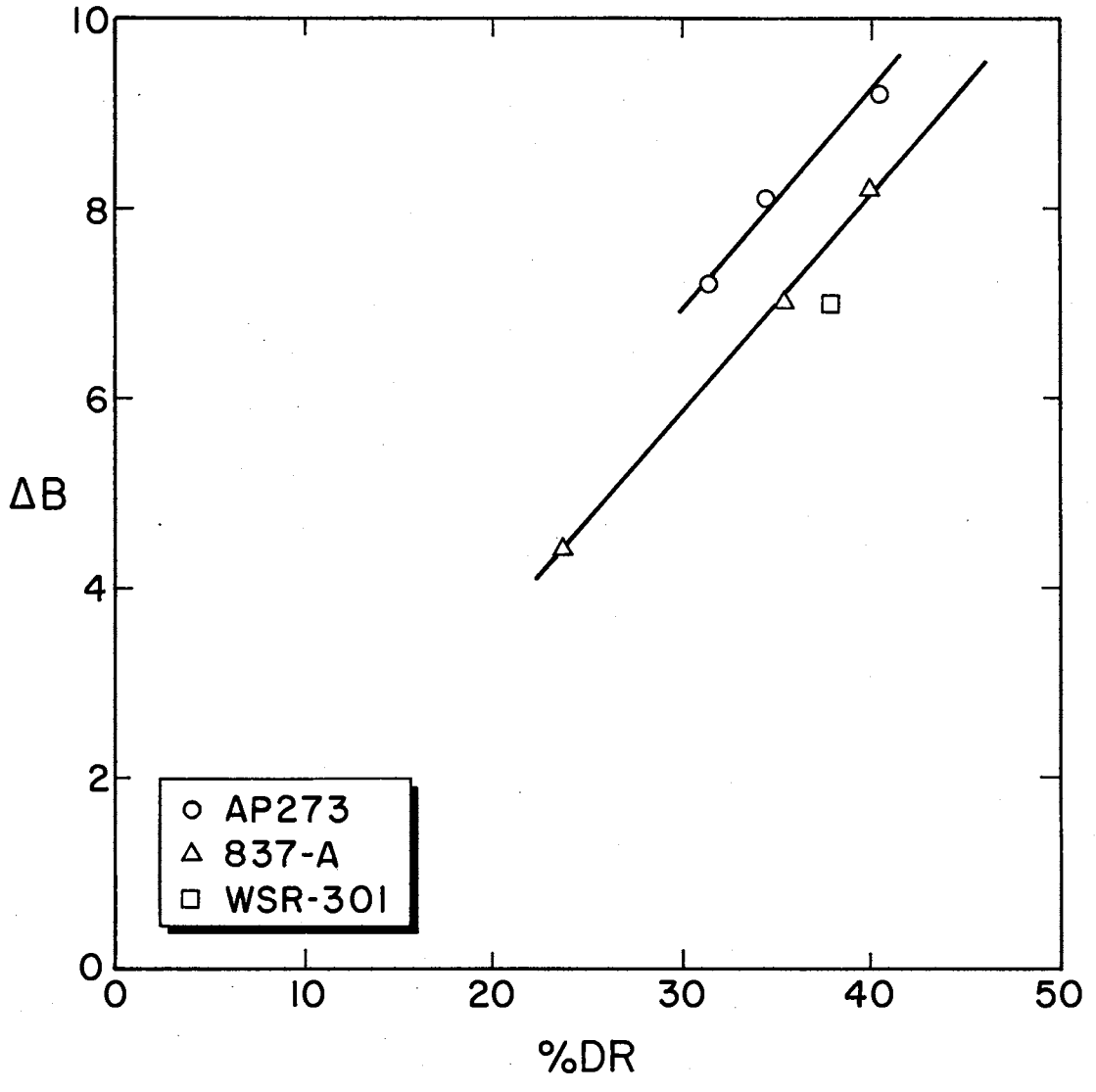

Figure 50. Correlation of ΔB with Percent Drag-Reduction

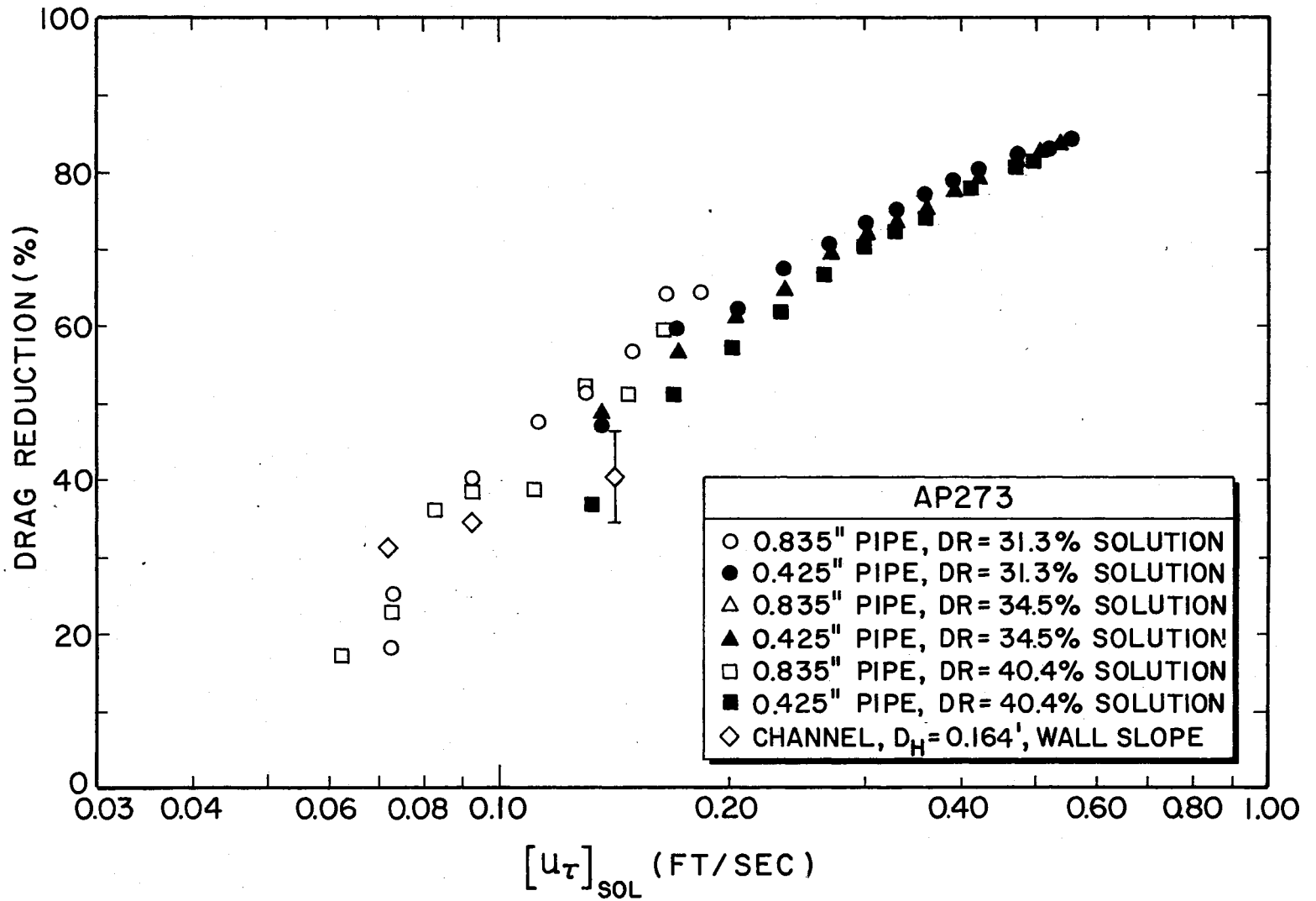

Figure 51. Drag-Reducing Characteristics of Separan AP273

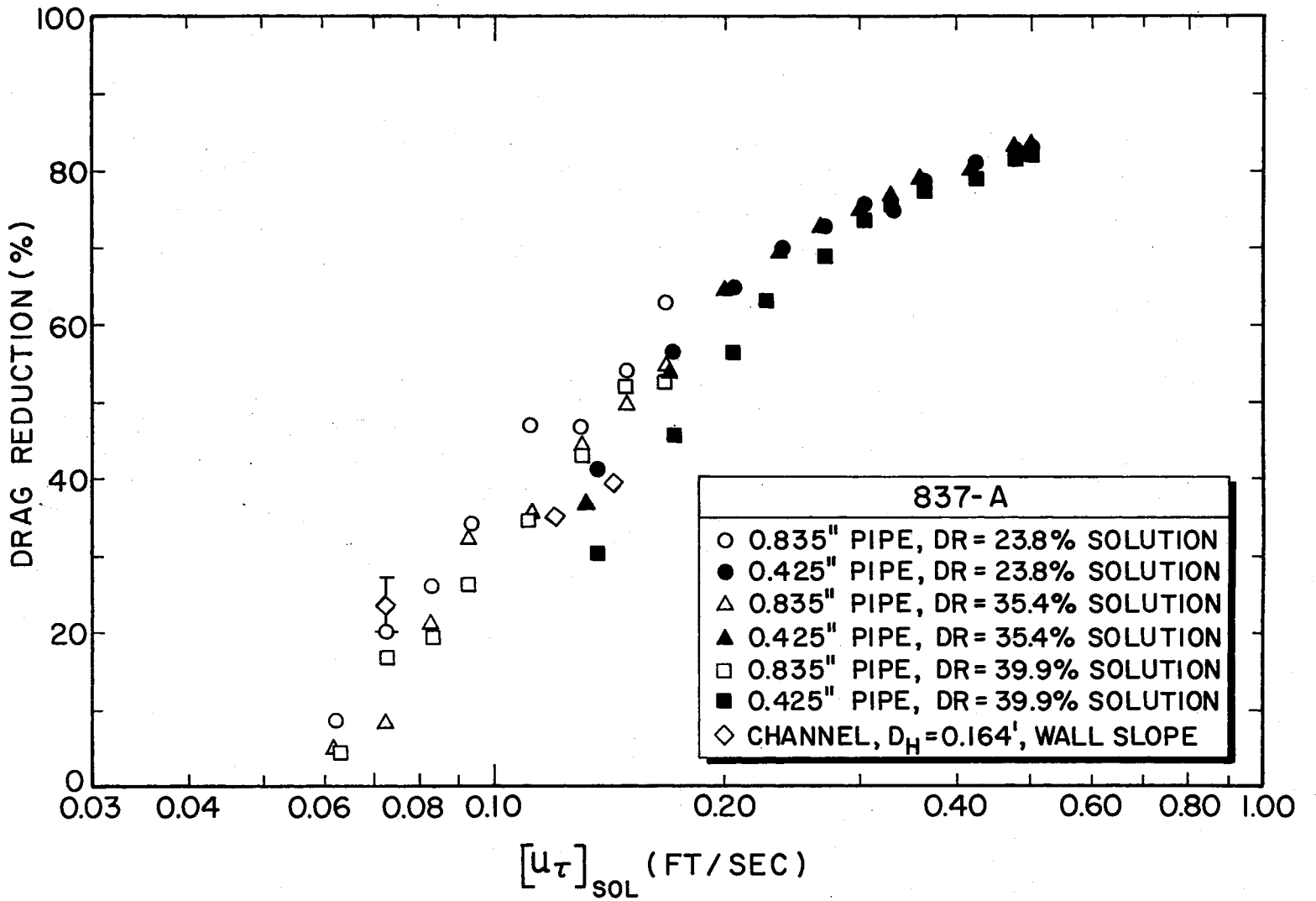

Figure 52. Drag-Reducing Characteristics of Magnifloc 837-A

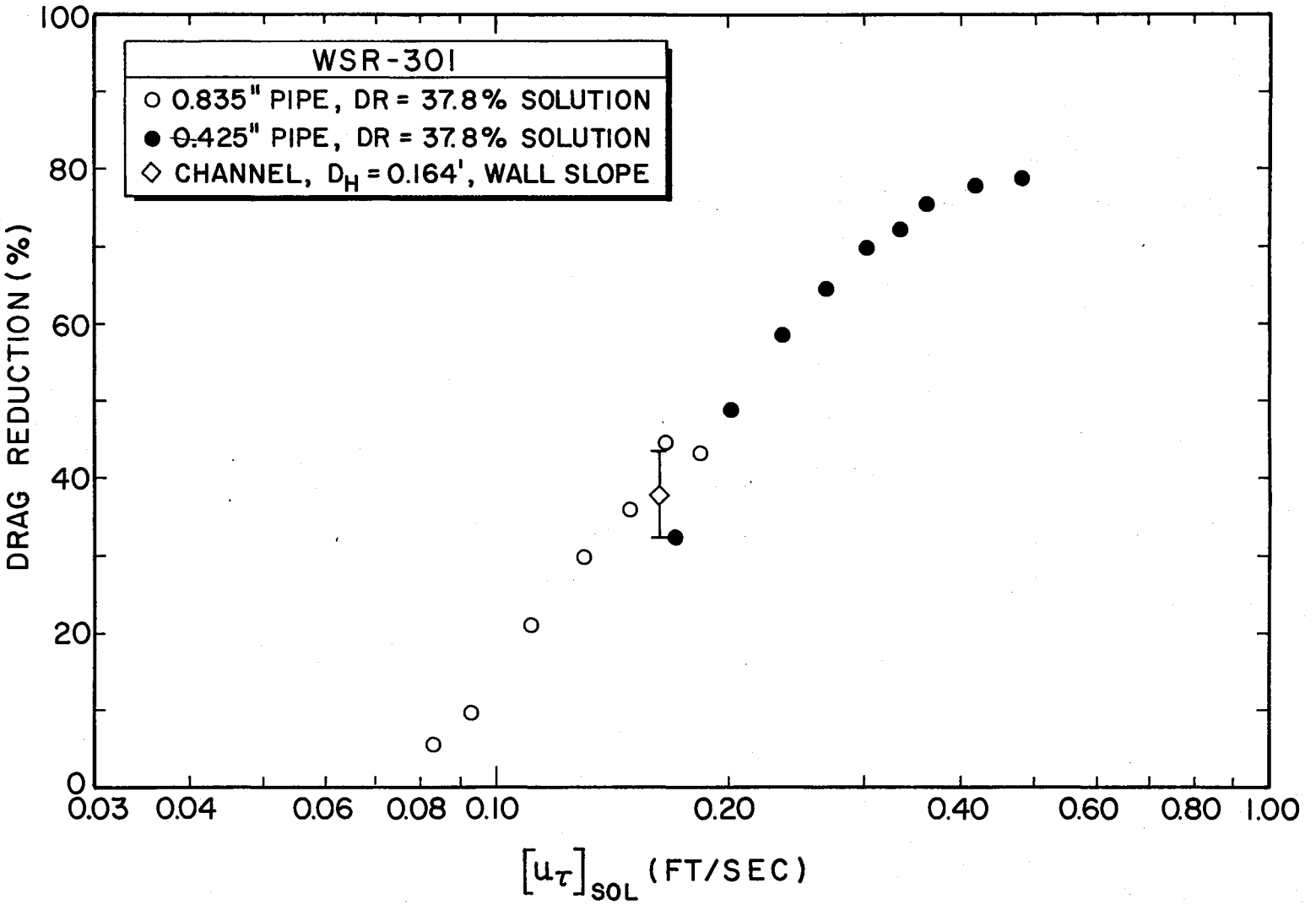

Figure 53. Drag-Reducing Characteristics of Polyox WSR-301

VITA

Michael Mack Reischman

Candidate for the Degree of

Doctor of Philosophy

Thesis: LASER ANEMOMETER MEASUREMENTS IN DRAG-REDUCING CHANNEL FLOWS

Major Field: Mechanical Engineering

Biographical:

Personal Data: Born in Barnesville, Ohio, September 26, 1942, son of Mr. and Mrs. O.J. Reischman, Sr.

Education: Graduated from Barnesville High School, Barnesville, Ohio in June, 1960; was enrolled in Ohio Technical College from 1960-1962 and received an Associate Degree of Electronic Engineering; was enrolled in the Mechanical Engineering Department at the University of New Mexico, 1962-1964; received a Bachelor of Science and Master of Science in Mechanical Engineering degree from New Mexico State University in 1967 and 1969, respectively; completed the requirements for the Doctor of Philosophy degree at Oklahoma State University in December, 1973.

Professional Experience: Electronic Technician, Los Alamos Scientific Laboratory, and the Physical Science Laboratory, 1962-1967; NDEA fellow and research assistant, New Mexico State University, 1967-1969; research associate and research assistant, Oklahoma State University, 1969-1973.